

SIFTING FOR A STREAM: THE MORPHOLOGY OF THE 300S STELLAR STREAM

BENJAMIN COHEN^{1,*}, ALEXANDER P. JI^{2,3}, PETER S. FERGUSON⁴, SERGEY E. KOPOSOV^{5,6},
ALEX DRLICA-WAGNER^{2,3,7}, ANDREW P. LI⁸, TING S. LI^{8,9,10}, LARA R. CULLINANE¹¹, GARY S. DA COSTA^{12,13},
DENIS ERKAL¹⁴, KYLER KUEHN¹⁵, GERAINT F. LEWIS¹⁶, SARAH L. MARTELL^{13,17}, ANDREW B. PACE¹⁸,
DANIEL B. ZUCKER^{19,20}, PETRA AWAD²¹, JOSS BLAND-HAWTHORN^{13,16}, GUILHERME LIMBERG³,
CLARA E. MARTÍNEZ-VÁZQUEZ²², JOSHUA D. SIMON²³, AND YONG YANG¹⁶

¹Department of Physics, University of Chicago, 5640 S Ellis Avenue, Chicago, IL 60637, USA

²Department of Astronomy & Astrophysics, University of Chicago, 5640 S Ellis Avenue, Chicago, IL 60637, USA

³Kavli Institute for Cosmological Physics, University of Chicago, Chicago, IL 60637, USA

⁴DIRAC Institute, Department of Astronomy, University of Washington, 3910 15th Ave NE, Seattle, WA, 98195, USA

⁵Institute for Astronomy, University of Edinburgh, Royal Observatory, Blackford Hill, Edinburgh EH9 3HJ, UK

⁶Institute of Astronomy, University of Cambridge, Madingley Road, Cambridge CB3 0HA, UK

⁷Fermi National Accelerator Laboratory, P.O. Box 500, Batavia, IL 60510, USA

⁸Department of Astronomy and Astrophysics, University of Toronto, 50 St. George Street, Toronto ON, M5S 3H4, Canada

⁹Dunlap Institute for Astronomy & Astrophysics, University of Toronto, 50 St George Street, Toronto, ON M5S 3H4, Canada
¹⁰Data Sciences Institute, University of Toronto, 17th Floor, Ontario Power Building, 700 University Ave, Toronto, ON M5G 1Z5, Canada

¹¹Leibniz-Institut für Astrophysik Potsdam (AIP), An der Sternwarte 16, D-14482 Potsdam, Germany

¹²Research School of Astronomy and Astrophysics, Australian National University, Canberra, ACT 2611, Australia

¹³Centre of Excellence for All-Sky Astrophysics in Three Dimensions (ASTRO 3D), Australia

¹⁴Department of Physics, University of Surrey, Guildford GU2 7XH, UK

¹⁵Lowell Observatory, 1400 W Mars Hill Rd, Flagstaff, AZ 86001, USA

¹⁶Sydney Institute for Astronomy, School of Physics, A28, The University of Sydney, NSW 2006, Australia

¹⁷School of Physics, University of New South Wales, Sydney, NSW 2052, Australia

¹⁸Department of Astronomy, University of Virginia, 530 McCormick Road, Charlottesville, VA 22904, USA

¹⁹School of Mathematical and Physical Sciences, Macquarie University, Sydney, NSW 2109, Australia

²⁰Macquarie University Research Centre for Astrophysics and Space Technologies, Sydney, NSW 2109, Australia

²¹Leiden Observatory, Leiden University, P.O.Box 9513, 2300RA Leiden, The Netherlands

²²Gemini Observatory, NSF's NOIRLab, 670 N. A'ohoku Place, Hilo, HI 96720, USA and

²³Observatories of the Carnegie Institution for Science, 813 Santa Barbara St., Pasadena, CA 91101, USA

(*S*⁵ COLLABORATION)

Version June 27, 2025

ABSTRACT

Stellar streams are sensitive laboratories for understanding the small-scale structure in our Galaxy's gravitational field. Here, we analyze the morphology of the 300S stellar stream, which has an eccentric, retrograde orbit and thus could be an especially powerful probe of both baryonic and dark substructures within the Milky Way. Due to extensive background contamination from the Sagittarius stream (Sgr), we perform an analysis combining Dark Energy Camera Legacy Survey photometry, *Gaia* DR3 proper motions, and spectroscopy from the Southern Stellar Stream Spectroscopic Survey (*S*⁵). We redetermine the stream coordinate system and distance gradient, then apply two approaches to describe 300S's morphology. In the first, we analyze stars from *Gaia* using proper motions to remove Sgr. In the second, we generate a simultaneous model of 300S and Sgr based purely on photometric information. Both approaches agree within their respective domains and describe the stream over a region spanning 33°. Overall, 300S has three well-defined density peaks and smooth variations in stream width. Furthermore, 300S has a possible gap of $\sim 4.7^\circ$ and a kink. Dynamical modeling of the kink implies that 300S was dramatically influenced by the Large Magellanic Cloud. This is the first model of 300S's morphology across its entire known footprint, opening the door for deeper analysis to constrain the structures of the Milky Way.

Keywords: Stellar streams (2166), Milky Way Galaxy (1054), Local Group (929), Magellanic Clouds (990), Globular star clusters (656)

1. INTRODUCTION

Stellar streams form through the tidal disruption of progenitor systems, such as globular clusters or dwarf galaxies. As the progenitor approaches a more massive host such as the Milky Way, tidal forces strip stars off of the progenitor near its Lagrange points. Stars released from the inner Lagrange point lose energy and move ahead of the progenitor to form the leading arm of

the stream, while stars released from the outer Lagrange point gain energy and fall behind to form the trailing arm (e.g., Johnston 1998; Küpper et al. 2008; Küpper et al. 2010). In a smooth potential without any external perturbations, stellar streams become long, relatively smooth structures that approximately follow the orbital track of their progenitor (Carlin & Newberg 2016). Because of this regularity, stellar streams are especially sensitive to both the Milky Way mass profile and perturbations within that profile, making them of great interest

*Corresponding Author: benmckcohen@uchicago.edu

in the study of Galactic dynamics. They have been used to analyze the geometry of the Galactic potential (e.g., Bonaca et al. 2014; Küpper et al. 2015; Bovy et al. 2016; Vasiliev et al. 2021; Ibata et al. 2023), constrain the mass of the Large Magellanic Cloud (LMC, e.g., Erkal et al. 2019; Shipp et al. 2021; Koposov et al. 2023), investigate the presence of dark matter subhalos without baryons (e.g., Erkal et al. 2016; Bonaca et al. 2019; Banik et al. 2021), and as a present day example of hierarchical structure formation (e.g., Bonaca et al. 2021; Malhan et al. 2022). For the investigation of dark sub-halos and other small perturbations, streams on retrograde orbits are especially useful due to the smaller influence of the Galaxy’s spiral arms and bar (e.g., Hattori et al. 2016; Pearson et al. 2017; Erkal et al. 2017; Banik et al. 2021; Yang et al. 2025).

In the past 20 years, nearly 120 streams have been found, increasing the known number by two orders of magnitude (Bonaca & Price-Whelan 2024). Stream morphologies have been carefully analyzed for a few of these streams, including Pal 5 (Erkal et al. 2017), GD-1 (Price-Whelan & Bonaca 2018), Orphan/Chenab (Koposov et al. 2019), Jet (Ferguson et al. 2021), ATLAS/Aliqa Uma (Li et al. 2021), and Phoenix (Tavangar et al. 2022), among others. Furthermore, Patrick et al. (2022) characterized the morphology of a population of streams using data from the Dark Energy Survey (DES, Abbott et al. 2018), the Dark Energy Camera Legacy Survey (DECaLS, Dey et al. 2019), and Pan-STARRS (Chambers et al. 2016) which allowed them to investigate trends in stream morphology across the population. However, many streams remain poorly characterized, as their low surface brightnesses and large distances make it difficult to identify stream members.

One such stream is 300S. 300S is a globular cluster stream on an extremely eccentric, retrograde orbit (Li et al. 2022). Previous matched filter analyses identified 300S’s footprint as spanning at least 25° across the sky with endpoints at distances of ~ 14 kpc and ~ 19 kpc (Grillmair 2013; Bernard et al. 2016). Usman et al. (2024) found the stellar population of 300S to match a relatively metal rich ($[\text{Fe}/\text{H}] = -1.35$) and old (12.5 Gyr) isochrone. We present a more extensive review of literature measurements of 300S in Section 1.1.

Because of its eccentric, retrograde orbit, 300S could be used to set a strong constraint on the structure of the Milky Way’s gravitational potential and any associated perturbations. Indeed, because of 300S’s structure and dynamics, Lu et al. (2025) found it to be one of the most promising probes of small dark matter subhalos among a sample of 50 streams. Moreover, 300S was the only member of the top three such streams with a retrograde orbit. However, other than the qualitative descriptions from the matched filter maps of Grillmair (2013) and Bernard et al. (2016), little is known about the structural morphology of 300S. The challenge of describing 300S is exacerbated by its distance and the extensive background structure in the region from the Sagittarius stream (Sgr), which overlaps 300S in both on-sky position and distance (Simon et al. 2011). This challenge has prevented further analysis of 300S’s relationship to the Galactic potential.

In this paper, we extend and numerically characterize 300S’s structural morphology across 33° , extending the stream by $\sim 7^\circ$ and presenting a new look at its structure

despite the background contamination from Sgr. To do this, we utilize two distinct methods with two distinct datasets – *Gaia* Data Release (DR) 3 (Gaia Collaboration et al. 2016, 2023) and the Dark Energy Camera Legacy Survey (DECaLS) DR9 (Dey et al. 2019) – to remove the background contamination and extract the stream signal. We find that 300S has a complex structure, including variations in its stellar density, a $\sim 4.7^\circ$ gap, and a kink/bend in the stream track. To verify the position of the kink and investigate the influence of the LMC on 300S, we additionally perform preliminary dynamical modeling. This modeling reproduces the bend and indicates that the LMC had a dramatic influence on the formation of 300S.

We organize this paper as follows. In Section 2, we describe the DECaLS, *Gaia*, and Southern Stellar Stream Spectroscopic Survey (S^5) datasets. In Section 3, we discuss both (1) our initial characterization of the stream, including an initial matched filter search and identification of a stream-centric coordinate system (Section 3.1), and (2) our search for RR Lyrae (RRL) and Blue Horizontal Branch (BHB) stars, including our subsequent recalculation of 300S’s distance gradient (Section 3.2). We then describe our dual methodologies for accounting for the Sgr background contamination (Sections 4 and 5) and discuss the resulting models (Section 6). Motivated by our models, we perform preliminary dynamical modeling of 300S (Section 7). We conclude in Section 8.

1.1. History of 300S Characterization

Information on 300S has been slowly accumulated since its discovery in ~ 2007 . In this section, we provide a brief history of the analysis of 300S as a compact reference.

300S was first detected in multiple analyses of the Segue 1 satellite. In Geha et al. (2009) and Norris et al. (2010), 300S appeared as a small overdensity of stars with radial velocity of ~ 300 km s $^{-1}$, hence the name. In Belokurov et al. (2007) and Niederste-Ostholt et al. (2009), the stream manifested as an extended spatial overdensity around Segue 1. One of the first detailed analyses of 300S was presented in Simon et al. (2011), where the authors definitively determined its existence through a spectroscopic analysis of over 20 stars and subsequent confirmation of 300S’s distinct radial velocity. By comparing their radial velocity members’ Sloan Digital Sky Survey (SDSS) photometry to Galactic globular clusters, they also obtained initial estimates of $d \sim 22$ kpc and $[\text{Fe}/\text{H}] \sim -1.3$, though with considerable uncertainties. Because of 300S’s extreme radial velocity which differs from that of Segue 1 by ~ 100 km s $^{-1}$, they disassociated the two objects.

Further spectroscopic analysis of a bright member of 300S was conducted by Frebel et al. (2013). Their spectroscopic analysis measured $[\text{Fe}/\text{H}] = -1.46 \pm 0.05 \pm 0.23$ (random and systematic uncertainties respectively) and an isochrone fit gave $d = 18 \pm 7$ kpc, in agreement with Simon et al. (2011). They concluded from low aluminum and magnesium abundances that 300S is unlikely to have formed from a globular cluster. Finally, they disassociated 300S from Sgr and the Orphan stream, which are both present in the region, through their inconsistencies with 300S’s radial velocity and metallicity.

To further clarify the mounting characterization of this new structure, Grillmair (2013) performed a matched fil-

ter search over the region on SDSS data and identified 300S as extending over 25° with distances ranging from 14 ± 3 kpc to 18 ± 2 kpc. Bernard et al. (2016) also identified the stream in a matched filter search of the Pan-STARRS1 3π Survey, identifying 24° of the stream between ~ 14 kpc to ~ 19 kpc. They further note that 300S’s distance gradient is opposite to that of Sgr, providing further evidence for their disassociation.

Carlin et al. (2012) noted that 300S, termed Segue 1b in their work, had kinematics consistent with having the same origin as the Virgo Stellar Overdensity (VOD) in a recent, massive dwarf galaxy merger. This event has since been matched with the *Gaia*-Enceladus-Sausage merger (GES, Belokurov et al. 2018; Helmi et al. 2018; Haywood et al. 2018) by Simion et al. (2019) and Perotoni et al. (2022).

Building on these studies, Fu et al. (2018) searched for 300S members in APOGEE (Apache Point Observatory Galactic Evolution Experiment, Majewski et al. 2017) and SEGUE (Sloan Extension for Galactic Understanding and Exploration, Yanny et al. 2009) data using kinematic, distance, and CMD filters. They used a distance gradient based on the endpoints of 14 kpc and 19 kpc from Bernard et al. (2016). The on-sky distribution of their members confirmed 300S’s association to the elongated overdensity found by Belokurov et al. (2007) and Niederste-Ostholt et al. (2009). Their members had $[\text{Fe}/\text{H}] = -1.48$ with a dispersion of $0.21^{+0.12}_{-0.09}$. Fu et al. (2018) also fitted an orbit to the stream and found it to be highly eccentric ($e = 0.87$) with an peri/apocenter of $4.1/\sim 60$ kpc. This orbit is distinct from that of Sgr and similar to VOD’s, confirming Carlin et al. (2012)’s result. Finally, Fu et al. (2018) argue that 300S’s progenitor was a dwarf galaxy due to the apparent metallicity spread and lack of correlated light element abundances. They also find this conclusion consistent with their measured full width at half maximum of 0.94° ; with 300S’s velocity dispersion of $\sim 4 - 5$ km s $^{-1}$; and with its orbit eccentricity, all of which are higher than in standard globular cluster streams, such as Pal 5.

Using the STREAMFINDER algorithm (Malhan & Ibata 2018), Ibata et al. (2021) recovered 300S – labeled by them as *Gaia*-10 – in the combined *Gaia* DR2 and EDR3 data set. Using narrow-band imaging from the *Pristine* survey, Martin et al. (2022) identified a mean metallicity of $[\text{Fe}/\text{H}] = -1.4 \pm 0.06$. Using these *Gaia* results, Malhan et al. (2022) attempted to group objects based on possible merger associations. They found a potential merger that includes 300S with NGC 5466 and its associated stream, NGC 7492, and Tucana III, though the small number of objects in the association was not that significant ($< 2\sigma$ significance). They further noted that Massari et al. (2019) and Forbes (2020) associated NGC 7492 with GES and NGC 5466 with Sequoia.

As part of S^5 , Li et al. (2022) identified spectroscopic members of 300S to place the metallicity at $[\text{Fe}/\text{H}] = -1.26 \pm 0.03$ with a dispersion of $0.04^{+0.04}_{-0.02}$ with a 95% confidence upper limit of 0.11. Due to the small metallicity dispersion, they concluded that 300S has a globular cluster progenitor. Additionally, they determined the orbit to be relatively unique, with a high eccentricity ($e = 0.77$) and a peri/apocenter of $5.8/45.8$ kpc. This eccentricity was the highest of the 12 stream sample these

authors analyzed. Additionally, 300S was one of only two streams in their sample (the other being Jet) with a retrograde orbit and one of two (the other being AAU) at a non-extremity in its orbit. Because of 300S’s orbit, they associate the stream with the GES merger and with the objects NGC 5466 and Tucana III, in agreement with the associations of Malhan et al. (2022).

Finally, Usman et al. (2024) used 300S as a laboratory to study multiple stellar populations (MSPs). Using high resolution spectroscopy, they find no evidence of a metallicity dispersion and note that the most metal poor star found by Fu et al. (2018) has an inconsistent radial velocity and is probably a non-member of 300S. The lower resulting velocity dispersion and the identification of one star in 300S with an abundance pattern matching the “second population” in globular clusters (e.g., Bastian & Lardo 2018) confirm the conclusion of Li et al. (2022) that 300S’s progenitor was a globular cluster. Usman et al. (2024) argue that the low aluminum and magnesium abundances reported in Frebel et al. (2013) can be explained from the *ex situ* formation of 300S’s progenitor. In fact, they find the magnesium abundances to be similar to those of GES as described by Limberg et al. (2022), further supporting these objects’ association. They determine the metallicity of the stream to be $[\text{Fe}/\text{H}] = -1.35$. Using the observed luminosity of the stream and the time necessary for it to totally disrupt, they determine an initial mass range of $10^{4.5-4.8} M_\odot$ for the progenitor. Interestingly, they note that 300S’s initial mass may be close to a threshold to produce MSPs, although the value of that cutoff is still not known.

To summarize, 300S is a relatively metal rich, globular cluster stream on an extremely eccentric, retrograde orbit. Spatially, it traces at least 25° across the sky at distances between 14 kpc and 19 kpc. It is likely independent of Segue 1, Sgr, and Orphan, and evidence suggests that it is associated with the GES merger. Its chemistry indicates that it formed *ex situ*.

2. DATA

2.1. DECaLS DR9 Data

We use photometric information from the Dark Energy Camera (DECam; Flaugher et al. 2015) Legacy Survey (DECaLS) DR9 (Dey et al. 2019). We select a rectangular region $(-20^\circ, 20^\circ) \times (-15^\circ, 15^\circ)$ centered roughly on 300S in an earlier rendition of the stream coordinate system. We remove galaxies by requiring that the TYPE flag is PSF. We additionally apply certain quality cuts. First, we require that FRACFLUX for the g and r bands are both < 0.05 . This ensures that the measured flux is dominated by the source. We also require that the g and r band ANYMASK flags are 0 and FLUX values are > 0 .

We deredden the data using the corresponding transmission coefficients in MW_TRANSMISSION which represent the transmission of each band in linear units (see the discussion by Ruiz-Macias et al. 2021 for more details). To avoid any contamination from far-field objects that could obfuscate the detected stream features, we perform a magnitude cut of $g < 22.6$. As we are primarily focused on the main sequence and red giant branch, we follow Ferguson et al. (2021) and perform a color cut of $0 \leq g - r \leq 1$ except when searching for BHB candidate members (Section 3.2.2).

Finally, we apply masks to the data to prevent contamination by known field objects. We mask Segue 1 at (R.A., Decl.) of $(151.763^\circ, 16.073^\circ)$ as well as Leo I and Leo II at $(152^\circ, 12.5^\circ)$ and $(168.5^\circ, 22.2^\circ)$ respectively. We mask these objects with circles of angular radii 0.3° , 0.5° , 1.0° respectively. Of these overdensities, only Segue 1 lies anywhere near the stream track. Its half-light radius is 29 pc, which corresponds to an approximate half-light angular radius of $\sim 0.07^\circ$ given its distance of 23 kpc (Martin et al. 2008). Therefore, with a 0.3° mask radius, Segue 1 should not leak into our results. Further, as the stream full width at half maximum is $\sim 0.94^\circ$ (Fu et al. 2018, also see Section 6), the mask itself also should not influence our results. These cuts leave 2,046,607 sources over an $1,186 \text{ deg}^2$ region

We use this catalog to derive the initial matched filtered stellar density and stream coordinate system (Section 3.1), the refined matched filtered stellar density (Section 3.2.4), and one of our two empirical models of stream morphology (Section 5). We also use it to analyze the distance gradient of 300S (Section 7.2.3) and to cross-match against the other catalogs.

2.2. Gaia DR3 Data

We use astrometric information from *Gaia* DR3 (Gaia Collaboration et al. 2016, 2023). We follow Ferguson et al. (2021) and Pace et al. (2022) by removing nearby sources with a parallax cut of $\bar{\varpi} - 3\sigma_{\bar{\varpi}} < 0.05$. We additionally apply certain quality cuts. First, we ensure that the renormalized unit weight error (RUWE) is < 1.4 (as suggested by Pourbaix et al. 2022) and the goodness of fit statistic, `ASTROMETRIC_GOF_AL`, is < 3 (as suggested in Hambly et al. 2022). We also require `ASTROMETRIC_EXCESS_NOISE_SIG` to be < 2 (as in Pace et al. 2022). Further, we keep only sources with a corrected flux excess (C^* , see Equation 6 and discussion in Riello et al. 2021) satisfying $< 3\sigma_{C^*}(G)$ to exclude abnormal photometry. Finally, to prevent cross-contamination with Active Galactic Nuclei (AGN), we check that there is no overlap between our data and the *Gaia* `GAIAEDR3.AGN_CROSS_ID` table (as in Ferguson et al. 2021). We then cross-match the *Gaia* catalog with the DECaLS DR9 catalog using a matching radius of $0.5''$. We also apply the same object masks as we applied to the DECaLS DR9 data. These cuts leave 635,606 sources over a $1,401 \text{ deg}^2$ region.

We use this catalog as the basis for one of our two empirical models of stream morphology (Section 4).

2.3. S^5 Catalog

We use stellar parameters and radial velocities from the S^5 internal data release (iDR3.7).

S^5 spectra are acquired at the 3.9m Anglo-Australian Telescope at Siding Spring Observatory in Australia. Using the AAOmega double spectrograph (Smith et al. 2004) and the 2dF fibre positioner (Lewis et al. 2002), low-resolution blue spectra ($R \sim 1300$, $3800\text{\AA} < \lambda < 5800\text{\AA}$) and high-resolution red spectra ($R \sim 10,000$, $8420\text{\AA} < \lambda < 8840\text{\AA}$) are obtained simultaneously for up to 367 science targets, along with 25 sky fibers. These data are reduced with the 2dFdr software package (AAO software team 2015).

These data were processed using an improved pipeline from previous S^5 releases (such as iDR1.5, Li et al. 2019). Briefly, this pipeline fits a simultaneous model on both the red and blue arms of the AAOmega spectra as well as additional observations from different nights using RVSPECFIT (Koposov 2019). Details on the spectral fitting for these data are discussed in Ji et al. (2021) and Li et al. (2022).

300S members were extracted from these data using a mixture model. For more details on the membership selection, see A. P. Li et al. (in prep.). As we use the S^5 members as a pure ground-truth, we select stars with membership probability $> 99\%$. Like with *Gaia* DR3, we cross-match the S^5 catalog with the DECaLS DR9 catalog with a matching radius of $0.5''$ to create consistency between our datasets. This cut removes 7 stars, which all fail the cuts on the DECaLS DR9 dataset described in Section 2.1, and leaves a pure, matched selection of 66 members.

We use this catalog to fit polynomials for the 300S proper motion filters (Section 3.2.2), to rederive the 300S distance gradient (Section 3.2.3), and to prepare and evaluate our orbital models (Section 7).

3. PRELIMINARY EMPIRICAL CHARACTERIZATION

Here, we describe our preliminary analyses of 300S which are prerequisites to fitting models of stream morphology in Sections 4 and 5. To summarize, we begin with a naïve matched filter using the distance gradient of Fu et al. (2018). With this map, we are able to identify a stream coordinate system. We use this coordinate system to search for standard candles in the stream. We find only 1 RRL star and no BHB stars. We then derive a new distance gradient using the selected S^5 members and the RRL star. Finally, we redo the matched filter using our improved distance gradient and use it to motivate our methods of stream fitting.

3.1. Naïve Matched Filter and Coordinate System

The matched filter method is an important tool for extracting stream signal from a stellar density map (e.g., Odenkirchen et al. 2001; Rockosi et al. 2003). The method consists of matching stars in color-magnitude space to an isochrone chosen to reflect the object of interest. This way, overdensities whose color-magnitude distribution match that of the object pass through the filter, while overdensities whose distribution do not match are suppressed, effectively increasing the signal to noise ratio of the object in the map. This method has been used extensively in the mapping of stellar streams (e.g., Bonaca et al. 2012; Grillmair 2017; Shipp et al. 2018; Ferguson et al. 2021).

In this work, we adopt a $[\text{Fe}/\text{H}] = -1.35$, 12.5 Gyr isochrone, as was used for 300S by Usman et al. (2024). We use MIST’s DECam synthetic photometry (Dotter 2016) to generate the isochrone. Following Ferguson et al. (2021), we then consider stars to match the isochrone when they fall within a color range around it. As in Shipp et al. (2018) and Ferguson et al. (2021), we define an upper and lower color padding as

$$L(g_{\text{iso}}) = E \cdot \left(0.001 + e^{(g_{\text{iso}} + \mu_0 + \Delta\mu/2 - 27.09)/1.09} \right) + C_1 \quad (1)$$

$$U(g_{\text{iso}}) = E \cdot \left(0.001 + e^{(g_{\text{iso}} + \mu_0 - \Delta\mu/2 - 27.09)/1.09} \right) + C_2 \quad (2)$$

In order to get a purer, though less complete, sample in the presence of the strong contamination in the region, we add a scaling factor s and select stars with color

$$(g - r)_{\text{iso}} - s \times L(g_{\text{iso}}) < (g - r) < (g - r)_{\text{iso}} + s \times U(g_{\text{iso}}) \quad (3)$$

We set $\Delta\mu, E, C_1, C_2$ following [Shipp et al. \(2018\)](#) as 0.5, 2, 0.05, 0.1 respectively. We set $\mu_0 = 16.2$ ($d = 17.4$ kpc) as the distance modulus of the stream. This approximately corresponds to the [Fu et al. \(2018\)](#) distance gradient evaluated at the position of Segue 1. We set $s = 2/3$. We show the resulting density map of matching stars in [Figure 1\(b\)](#). For comparison, we also show the unfiltered map in [Figure 1\(a\)](#) where the only cuts are the quality and basic color-magnitude cuts described in [Section 2.1](#).

The presence of Sgr is clear in the unfiltered map as a wide band that extends across the field. Without the matched filter, this signal visually dominates over 300S. Although 300S becomes clearer in the matched filter map, there remains considerable contamination from Sgr, visible as a large, dark region above 300S. This is unsurprising given the chemical structure of Sgr and its age ([Limberg et al. 2023](#)). The strong presence of Sgr within the filtered map indicates that an isochrone-based filter in color-magnitude space is insufficient to isolate 300S's signal.

Due to the lack of a clear progenitor, we follow [Ferguson et al. \(2021\)](#) and define a stream coordinate system based on the visual extent of the stream in the matched filter map. We define endpoints at (R.A., Decl.) of $(147.0^\circ, 16.0^\circ)$ and $(168.5^\circ, 14.0^\circ)$. We then rotate the sphere such that these endpoints fall along the ϕ_1 -axis' great circle equidistant from 0. This rotation in Cartesian coordinates is the matrix

$$R = \begin{bmatrix} -0.89325016 & 0.36451269 & 0.26312478 \\ -0.39958263 & -0.91195263 & -0.09314568 \\ 0.20600456 & -0.18834248 & 0.96025477 \end{bmatrix}$$

and the $\phi_2 = 0^\circ$ line is visible in [Figure 1](#) as a dotted blue line. Under this transformation, ϕ_1 increases with R.A.

3.2. 300S Distance Gradient

In this section, we rederive 300S's distance gradient with a method robust against Sgr contamination.

3.2.1. Proper Motion Filter

We use a proper motion filter both to filter candidates in our search for standard candle members in [Section 3.2.2](#) and to extract 300S's signal in one of our two empirical models in [Section 4](#).

To derive our proper motion filter, we use the S^5 spectroscopic member catalog as a pure ground truth. We

Table 1
Coefficients for Quadratic Fits to S^5 Member Proper Motions and Radial Velocities

	a_0	a_1	a_2
$p_{\mu_{\alpha^*}}$	-3.5007	-0.1489	-0.0013
p_{μ_δ}	-3.0991	-0.0451	-0.0002
p_{vr}	297.80	-1.56	-0.09

first separately fit quadratic polynomials, p_{α^*} and p_δ , to these members in μ_{α^*} and μ_δ respectively.¹ The coefficients for these polynomials are given in [Table 1](#). Next, we compute the standard deviations of the residuals for these fits as σ_{α^*} and σ_δ respectively.² We then define our filters as

$$|\mu_{\alpha^*} - p_{\alpha^*}(\phi_1)| < N\sigma_{\alpha^*} \quad (4)$$

$$|\mu_\delta - p_\delta(\phi_1)| < N\sigma_\delta \quad (5)$$

where we set $N = 1.2$ to minimize contamination from Sgr. However, our general results are not sensitive to the specific value of N . For more discussion, see [Section 4](#).

We show these filters in [Figure 2](#). In addition to the filters, we show simulated proper motions of Sgr from the simulation of [Vasiliev et al. \(2021\)](#). If $N \gtrsim 1.2$, both proper motion filters would be contaminated by Sgr at $\phi_1 > -12.5^\circ$ where the peak 300S signal occurs, justifying the choice of $N = 1.2$. It includes the majority (61%) of the S^5 member stars while excluding the majority of Sgr in all of the region of interest.

3.2.2. Standard Candles

Standard candles such as BHB and RRL stars are an effective way to determine a stream's distance gradient because of their robust color-magnitude relations. Because of this, authors have used both BHB (e.g., [Deason et al. 2011](#); [Belokurov & Koposov 2015](#); [Ferguson et al. 2021](#); [Li et al. 2021](#)) and RRL (e.g., [Musella et al. 2012](#); [Garofalo et al. 2013](#); [Vivas et al. 2020](#); [Li et al. 2021](#)) stars as reliable distance tracers for streams and other Galactic structures. We search for both BHB and RRL stars in 300S.

To find BHB stars, we use our cross-matched DECaLS DR9 and *Gaia* DR3 catalogs. We first identify BHB candidates with color $(g - r) < 0$. Next, we filter on-stream stars by selecting only candidates with $|\phi_2| < 1^\circ$ which corresponds to ~ 2 times the stream full width at half maximum of [Fu et al. \(2018\)](#). We also require that $\phi_1 > -12.5^\circ$ to prevent the intersection of our filters and Sgr's simulated proper motions. We set an upper bound of $\phi_1 < 16^\circ$. We then calculate M_g using the relation of [Belokurov & Koposov \(2015\)](#)

$$M_g(g - r) = 0.398 - 0.392(g - r) + 2.729(g - r)^2 + 29.1128(g - r)^3 + 113.569(g - r)^4 \quad (6)$$

and select stars with distances in the range 13.5 – 19.5 kpc, which allows slight variation around 300S's distance extent of 14 – 19 kpc found by [Bernard et al. \(2016\)](#). This leaves 24 potential members. Finally, we select stars

¹ We notate $\mu_{\alpha^*} \equiv \mu_\alpha \cos \delta$.

² We find $\sigma_{\alpha^*} = 0.19 \text{ mas yr}^{-1}$ and $\sigma_\delta = 0.16 \text{ mas yr}^{-1}$.

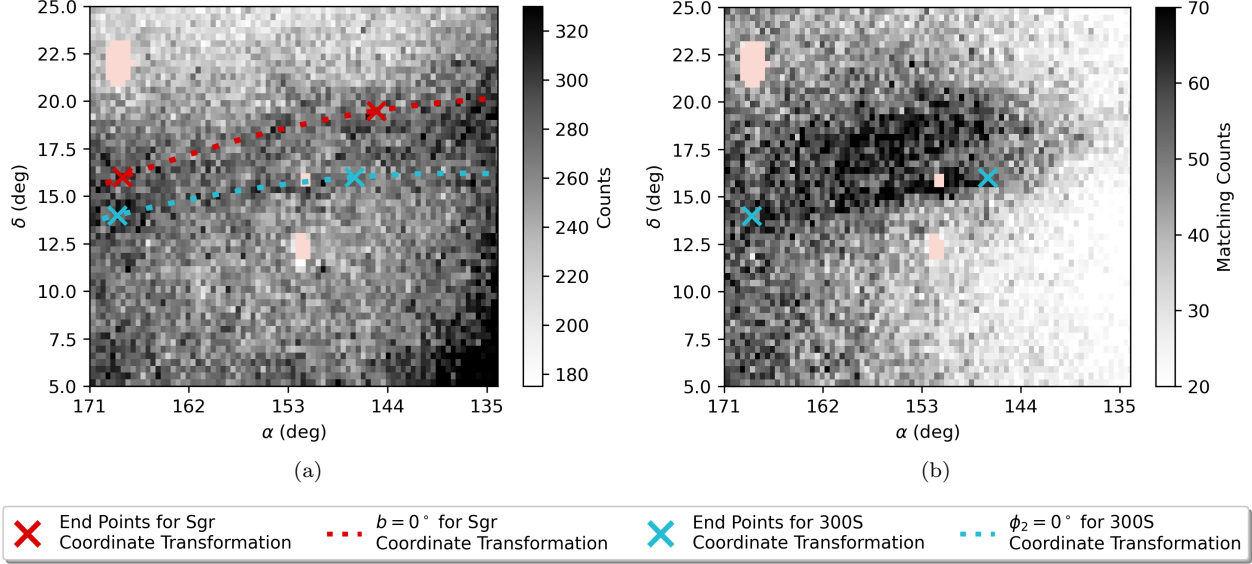


Figure 1. Initial stellar density maps. (a) Stellar density map without matched filter application. Stars were selected using only cuts described in Section 2.1 including the basic color ($0 < g - r < 1$) and magnitude ($g < 22.6$) cuts. The shaded red regions are the object masks. Note the presence of Sgr as the wide stripe across the unfiltered map. (b) Stellar density map under the naive matched filter. There is significant contamination from Sgr into the filtered map, as seen in the large dark region above 300S. This implies that an isochrone filter is insufficient to distinguish the two signals.

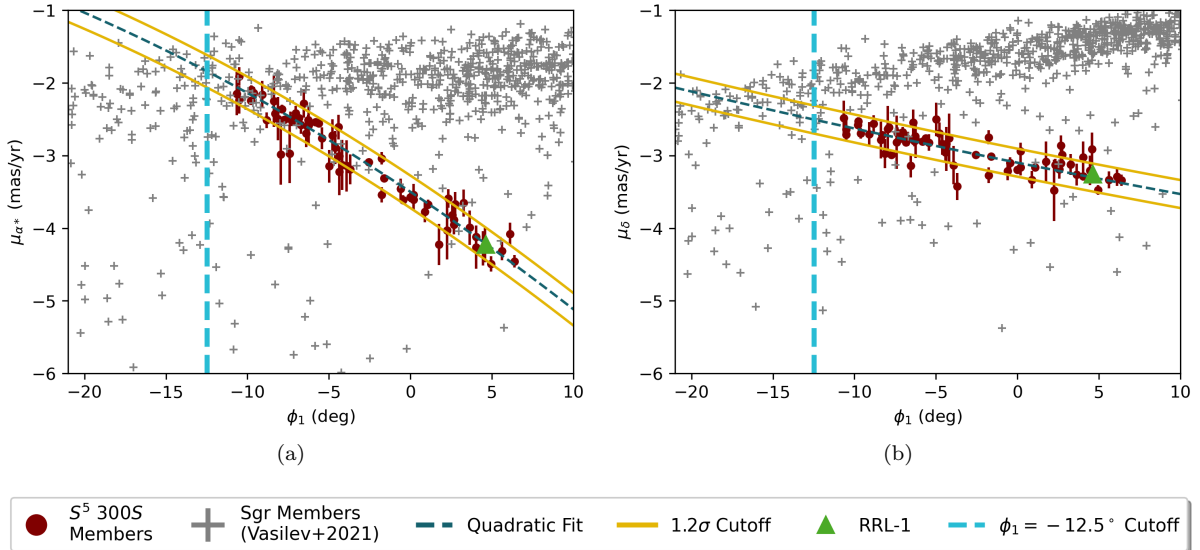


Figure 2. Proper motion filters. Sgr simulated members are taken from the nearest wrap in the simulations of Vasiliev et al. (2021). (a) Filter in μ_{α^*} . (b) Filter in μ_{δ} .

within our proper motion filter. No BHB candidates pass through this filter. Given the relatively high metallicity of 300S, the lack of BHB candidates follows the trend of reddening of the horizontal branch with higher metallicity (Soker & Hadar 2001).

To find RRL stars, we use the *Gaia* DR3 GA-ADR3.VARL_RRLYRAE table, which consists of cleaned and validated data on RRL stars (Clementini et al. 2023). As with the BHB stars, we select members with $|\phi_2| < 1^\circ$, $-12.5^\circ < \phi_1 < 16^\circ$, and a position outside of the object masks. We calculate M_G using the PWZ relation of Garofalo et al. (2022):

$$\begin{aligned}
 W(G, G_{BP}, G_{RP}) &= G - \lambda \times (G_{BP} - G_{RP}) \\
 &= (-2.49^{+0.21}_{-0.20}) \log(P) + (0.14^{+0.03}_{-0.03}) [\text{Fe}/\text{H}] \\
 &\quad + (-0.88^{+0.08}_{-0.09}) \quad (7)
 \end{aligned}$$

where $\lambda = 1.922$ (Garofalo et al. 2022). We assume an RRL metallicity matching Usman et al. (2024)'s 300S metallicity of -1.35 with an uncertainty of 0.11 dex. This uncertainty is the $< 95\%$ metallicity dispersion for 300S found by Li et al. (2022). We again select stars with distance in the range $13.5 - 19.5$ kpc. This results in 8

Table 2
Parameters of the Likely RRL Member: RRL-1

Parameter	Value for RRL-1
<i>Gaia</i> DR3 SOURCE_ID	3885177800499823616
μ_{α^*} (mas yr ⁻¹)	-4.22 ± 0.07
μ_{δ} (mas yr ⁻¹)	-3.26 ± 0.06
# σ_{α^*}	0.04
# σ_{δ}	0.28
Distance (kpc)	14.9 ± 1.1
v_r (km s ⁻¹)	302.9 ± 2.8
ϕ_1 (deg)	4.63
ϕ_2 (deg)	0.02

The radial velocity is from the work of [Fu et al. \(2018\)](#). # σ is the number of standard deviations away from the corresponding proper motion fit.

candidates. After application of our proper motion filter, we are left with one RRL member, henceforth referred to as RRL-1. This star was also identified as a candidate member in [Fu et al. \(2018\)](#) due to its velocity of 302.9 km s⁻¹ and position.³ [Fu et al. \(2018\)](#) do not classify it as a member because of its offset from a 12 Gyr, [Fe/H] = -1.5 isochrone at the distance modulus given by their gradient. However, we suspect that this can be explained by RRL photometric variability.

RRL-1’s position and velocity indicate that it is a stream member. Because its heliocentric distance is 14.9 kpc and galactocentric distance is 19 kpc, it is unlikely to be associated with either the Galactic disk or bulge. Similarly, RRL-1 is unlikely to be a member of Sgr. Our empirical model of Sgr (see Section 5.2.2) places its closest wrap in the region at a heliocentric distance of ~ 20 kpc and simulations place it further at ~ 25 kpc ([Vasiliev et al. 2021](#)) while RRL-1 only has a heliocentric distance of 14.9 ± 1.1 kpc. Further, in addition to its distance and radial velocity, RRL-1’s proper motions are only 0.04 σ_{α^*} and 0.28 σ_{δ} off Section 3.2.1’s respective best fit curves. Because RRL-1’s kinematics in terms of its proper motions from *Gaia* and its radial velocity from [Fu et al. \(2018\)](#)’s study both fit 300S well, and because its distance further rules out other possible associations, we identify RRL-1 as a member of 300S.

We note that one other RRL star,⁴ henceforth referred to as RRL-2, passes our proper motion filter if we expand the cutoff from 1.2 σ to 2.5 σ . Specifically, RRL-2 has proper motions at 2.32 σ_{ra} and 2.29 σ_{dec} off Section 3.2.1’s respective best fit curves. However, RRL-2’s radial velocity was measured by [Liu et al. \(2020\)](#) to be -60.772 km s⁻¹ which is substantially different from the characteristic radial velocity of 300S of ~ 300 km s⁻¹. Therefore, this star is a nonmember.

3.2.3. Distance Gradient Calculation

We are unable to derive a distance gradient directly from standard candles because we only identify one such likely member, RRL-1. To determine the slope of the gradient, we use the pure S^5 member catalog and derive a gradient that minimizes the red giant branch members’ spread around an isochrone. Specifically, we begin by selecting S^5 members that are on the red giant branch by

considering stars with whose matched DECaLS photometry satisfies $(g - r) > 0.35$ and $g > 17.25$. Next, we calculate the distance modulus of the S^5 members from the [Fe/H] = -1.35, 12.5 Gyr isochrone described in Section 3.1, again using the matched DECaLS photometry. We then perform linear regression on these distance moduli. This regression gives a slope $k_{S^5} = -0.035 \pm 0.006$ and intercept $b_{S^5} = 16.2 \pm 0.04$.

We then set the intercept such that the distance gradient goes through RRL-1. Although we could set this intercept using the S^5 distance moduli, this number is highly dependent on the choice of isochrone. For instance, when changing from [Fe/H] = -1.35 (as reported in [Usman et al. 2024](#)) to [Fe/H] = -1.26 (as reported in [Li et al. 2022](#)), k_{S^5} changes by 0.001, or only 0.12 σ , while b_{S^5} changes by 0.19, or > 3 σ .

This calculation leads to a distance gradient of

$$\mu_{300S}(\phi_1) = (-0.035 \pm 0.006)\phi_1 + (16.03 \pm 0.16) \quad (8)$$

Note that the intercept is nevertheless in ~ 1 σ agreement with b_{S^5} . [Fu et al. \(2018\)](#) found a distance gradient as a function of R.A. of

$$d(\alpha) = 48.9952 - 0.2083\alpha \quad (9)$$

where α is the R.A. We cannot exactly compare Equation 8 to Equation 9 because the gradient of [Fu et al. \(2018\)](#) is linear in R.A. and distance while the gradient in this work is linear in ϕ_1 and distance modulus. To make a comparison, we convert the [Fu et al. \(2018\)](#) gradient into ϕ_1 and distance modulus using our transformation matrix by converting $(\phi_1, 0^\circ)$ pairs to (R.A., Decl.) pairs and evaluating $\mu_{fu}(\phi_1) = \mu(d_{fu}(\alpha(\phi_1, 0^\circ)))$. We then fit a linear function to the result in the region of interest ($\phi_1 \in [-20^\circ, 13^\circ]$). After this conversion, the [Fu et al. \(2018\)](#) gradient takes the form

$$\mu_{fu}(\phi_1) \approx -0.028\phi_1 + 16.02 \quad (10)$$

Both the slope and intercept are in reasonable agreement between these two distance gradients ($\Delta k = 1.2\sigma$ and $\Delta b = 0.06\sigma$ excluding uncertainties in the [Fu et al. 2018](#) gradient). We show the two gradients and the non-linearized [Fu et al. \(2018\)](#) result in Figure 3. Over the region of interest where we model 300S, Equation 8 implies an average distance modulus of 16.15 corresponding to a physical distance of 17 kpc.

3.2.4. Refined Matched Filter as Motivation for Filtering Methodologies

We improve our matched filter map using the distance gradient we derived in Section 3.2. We show the 300S matched filter on a Hess diagram of an on-stream region with distance moduli computed using Equation 8 in Figure 4(a). We show the refined matched filter map in Figure 4(b).

300S is visible in this map as the thin overdensity around $\phi_2 = 0^\circ$. The Sgr contamination is also still visible as a wide overdensity above 300S. This map makes the challenge of modeling 300S’s morphology clear. An approach directly modeling the stream and background like that of [Ferguson et al. \(2021\)](#) would be complicated by the Sgr signal. Therefore, this map motivates the

³ There identified as PSO J105016.344+144644.466.

⁴ *Gaia* DR3 SOURCE_ID 621603371140586880.

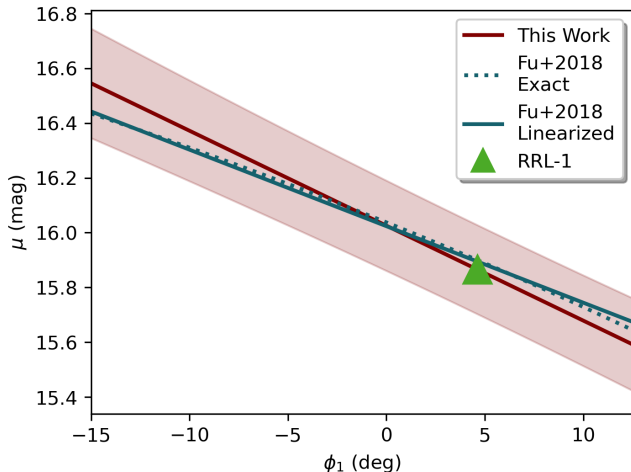


Figure 3. Comparison of our calculated distance gradient and the transformed gradient of Fu et al. (2018) both in its linearized and exact forms. The shaded region represents 1σ uncertainty.

need for additional methods of signal extraction. The next two sections describe the two approaches we use to account for Sgr’s influence.

4. FITTING MODELS OF STREAM MORPHOLOGY METHOD 1: FILTERING USING *GAIA* DR3 DATA

Our first method to filter Sgr contamination is to use kinematic information from *Gaia* DR3. Because 300S’s main sequence turnoff is at $g \simeq 20$, many candidate members have large proper motion uncertainties and are omitted. Therefore, this method excludes many candidate members; leading to a relatively pure but incomplete selection. Because of the resulting low number counts, this method alone is insufficient to extract much of the stream structure with certainty. Instead, we use it as a check against our second filtering method (Section 5), which uses purely photometric information from DECaLS DR9 and extracts a less pure selection with much higher completeness.

4.1. Filtering 300S’s Signal

We use the proper motion filters derived in Section 3.2.1 as the primary filter for 300S’s signal. Because 300S has a main sequence turnoff at $g \simeq 20$, the proper motion uncertainties for many candidate stars are very large. Therefore, to ensure purity, we begin by constraining the *Gaia* catalog to stars with $\sqrt{\sigma_{\mu_{\alpha^*}}^2 + \sigma_{\mu_{\delta}}^2} < 0.8 \text{ mas yr}^{-1}$ and with $g < 20.5$.

Next, because 300S and Sgr’s proper motions are very similar at some negative values of ϕ_1 as can be seen in Figure 2, we remove stars with $\phi_1 < -12.5^\circ$ to prevent contamination. This cut is shown in Figure 2 as a light blue dashed line. We consider $\phi_2 \in [-5^\circ, 5^\circ]$ to match the region used in Method 2 (Section 5). We then employ the proper motion filters described in Section 3.2.1.

Next, we apply a matched filter on the turnoff, subgiant branch, red-giant branch, and horizontal branch using the cross-matched DECaLS photometry. We define this matched filter in three components. First, we define a filter over magnitudes that matches stars with $M_g^{\text{iso}} \in$

$[-0.5, 4]$ using upper and lower magnitude cuts of δ_{upper} and δ_{lower} respectively around the isochrone magnitude $M_g^{\text{iso}}(g-r)$. i.e.

$$M_g^{\text{iso}}(g-r) - \delta_{\text{lower}} < M_g < M_g^{\text{iso}}(g-r) + \delta_{\text{upper}} \quad (11)$$

where M_g is calculated using the distance gradient in Equation 8.

Second, we define a filter over colors that matches stars with $M_g^{\text{iso}} \in [3.6, 5]$ using right and left color cuts of δ_{right} and δ_{left} respectively around the isochrone color $(g-r)_{\text{iso}}$. i.e.

$$(g-r)_{\text{iso}} - \delta_{\text{left}} < (g-r) < (g-r)_{\text{iso}} + \delta_{\text{right}} \quad (12)$$

Third, we define a filter around the visible horizontal branch (HB) overdensity. For this filter, we select stars within a rectangle with center (c_{g-r}, c_{M_g}) , width w , and height h . i.e.

$$\begin{aligned} |(g-r) - c_{g-r}| &< w/2 \\ \&\& \quad |M_g - c_{M_g}| < h/2 \end{aligned} \quad (13)$$

and we accept stars that fall into any of the three filters. We define these filters by eye in order to extract the visible isochrone on the CMD, as seen in Figure 5(a). We use parameters $\delta_{\text{lower}} = 0.3$, $\delta_{\text{upper}} = 0.8$, $\delta_{\text{left}} = 0.043$, $\delta_{\text{right}} = 0.087$, $c_{g-r} = 0.345$, $c_{M_g} = 0.825$, $w = 0.23$, and $h = 0.45$. After we apply these filters, we bin the stars into ϕ_1, ϕ_2 bins of width $\Delta\phi_1 = 0.3^\circ$ and height $\Delta\phi_2 = 0.2^\circ$. We show this filter, the underlying background subtracted color-magnitude distribution of the stars selected with proper motions, and the resulting stellar density map in Figure 5. The Sgr overdensity that was visible in Figure 4(b) is no longer present. Nevertheless, the peak of 300S around $\phi_1 = -6^\circ$ (peak A) that is visible near Segue 1 in Figure 4(b) is still apparent in Figure 5(b)’s density map.

4.2. Modeling 300S’s Morphology

We model the morphology of 300S using a modified version of the approach developed in Koposov et al. (2019), Li et al. (2021), and Ferguson et al. (2021). In this method, the stream is modeled using three components: $\mathcal{I}(\phi_1)$, $w(\phi_1)$ and $\Phi_2(\phi_1)$ as the log central stellar density, log Gaussian width, and ϕ_2 position, respectively. As a 2D function of these components, the stream density Λ_{300S} can be written as

$$\log \Lambda_{300S}(\phi_1, \phi_2) = \mathcal{I}(\phi_1) - \frac{(\phi_2 - \Phi_2(\phi_1))^2}{2e^{2w(\phi_1)}} \quad (14)$$

Further, a background component $\log \Lambda_{\text{background}}$ is included in the model as a polynomial with coefficients \vec{B} . In previous studies, quadratics with $\vec{B} \in \mathbb{R}^3$ have been used (e.g., Ferguson et al. 2021), i.e. $\log \Lambda_{\text{background}} = [1 \ \phi_1 \ \phi_1^2] \cdot \vec{B}$. Due to the high purity and low overall counts for the *Gaia* stars here, we use a linear background model with $\vec{B} \in \mathbb{R}^2$.

We assume that the stars are Poisson distributed in the histogram bins with a spatially varying rate defined by these models as $\Lambda(\phi_1, \phi_2) = \Lambda_{300S}(\phi_1, \phi_2) +$

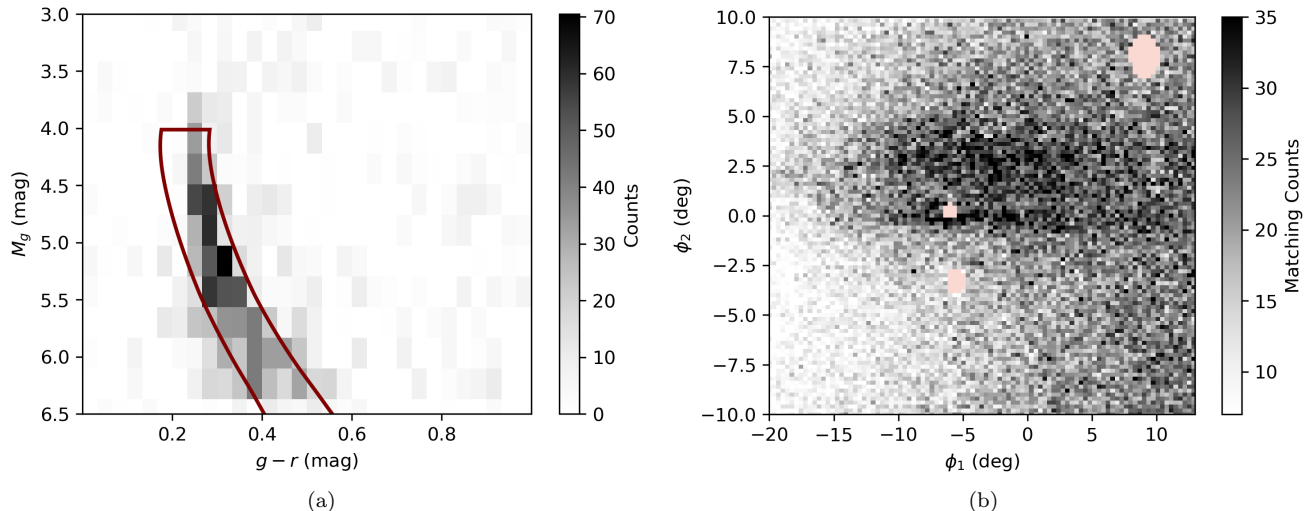


Figure 4. (a) Hess diagram for on-stream region. M_g was computed assuming a distance modulus calculated using Equation 8. The red outline shows the 300S matched filter ($s = 2/3$) used in this work. (b) Refined matched filter density map. 300S is clearly visible as the thin band centered on $\phi_2 = 0^\circ$. The Sgr contamination seen in Figure 1 is still visible as a wide dark region above 300S centered at $\phi_2 \sim 2.5^\circ$. The red shaded regions are the object masks.

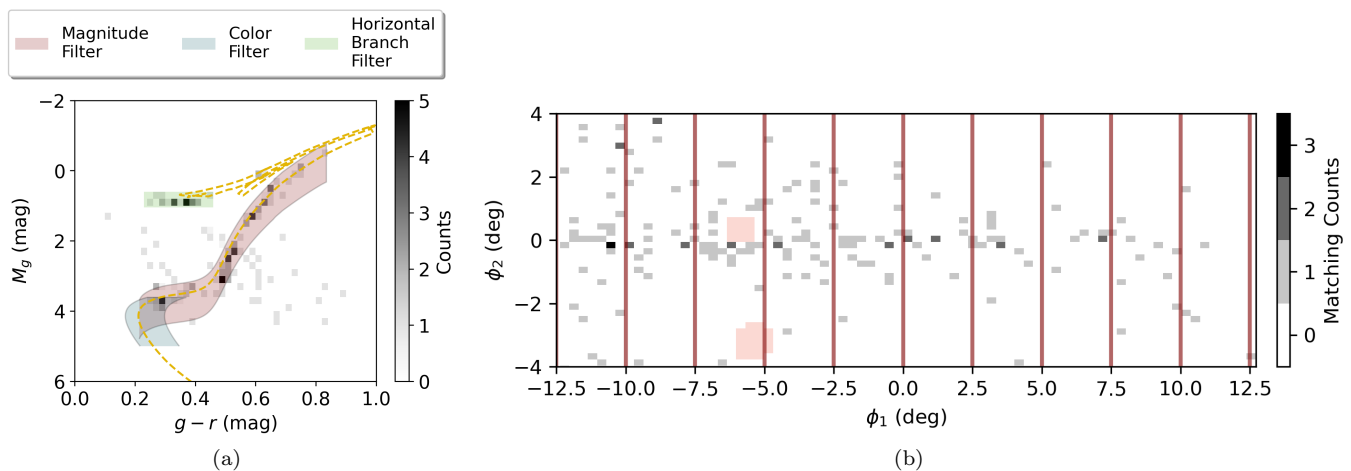


Figure 5. Results from filtering using *Gaia* proper motions in Section 4. (a) The matched filter used for the Method 1 of signal extraction. The yellow dashed line is the $[\text{Fe}/\text{H}] = -1.35$, Age = 12.5 Gyr isochrone used in this work. A Hess diagram of the sample that passes the quality cuts and proper motion filters is also shown. The 300S isochrone is clearly visible. (b) Stellar density map in the vicinity of 300S after filtering. The red shaded regions are the object masks.

$\Lambda_{\text{background}}(\phi_1, \phi_2)$. We then define our composite Poisson likelihood as

$$\log \mathcal{L} = \sum_{\text{bin } i} \log \mathcal{P} \left(N^{(i)} \middle| \Lambda(\phi_1^{(i)}, \phi_2^{(i)}) \right) \quad (15)$$

where $N^{(i)}$ is the number count of matched stars in bin i and $\phi_1^{(i)}, \phi_2^{(i)}$ are its coordinates.

We parameterize $\vec{B}(\phi_1)$, $\mathcal{I}(\phi_1)$, $w(\phi_1)$, and $\Phi_2(\phi_1)$ as cubic splines (as in e.g. Koposov et al. 2019; Li et al. 2021; Ferguson et al. 2021). Including the endpoints, we use 13 nodes for the stream parameters $\mathcal{I}(\phi_1)$, $w(\phi_1)$, and $\Phi_2(\phi_1)$. We use 6 nodes for \vec{B} . Small modifications to both the number and position of these nodes do not dramatically alter the results. Given a set of node positions in ϕ_1 , we desire to sample the posterior y -values of those nodes using the composite Poisson likelihood de-

finied above. We follow Koposov et al. (2019) and only set non-trivial priors on the $\Phi_2(\phi_1)$ and $w(\phi_1)$. We use $\mathcal{N}(0, 1)$ for $\Phi_2(\phi_1)$. We set $\mathcal{N}(\log 0.4, 0.5)$ for $w(\phi_1)$. This is the same width σ as used by Koposov et al. (2023) but with a mean stream full width at half maximum of 0.94° as found for 300S by Fu et al. (2018). We sample the node coefficients using STAN (Carpenter et al. 2017; Stan Development Team 2018), an optimized implementation of Hamiltonian Markov Chain Monte Carlo (MCMC) (Neal 2011) that applies the No U-Turn method to reduce fine-tuning and increase efficiency (Hoffman & Gelman 2011).⁵ We run the sampler for 700 warmup iterations and 800 sampling iterations using 4 chains. All of the parameters achieve a satisfactory \hat{R} score of < 1.1 indi-

⁵ We made use of STAN-SPLINES, <https://zenodo.org/records/14163685>, an implementation of natural cubic splines in STAN (Koposov et al. 2019).

cating convergence (Gelman & Rubin 1992).

We present the results of Method 1, including the median splines and corresponding 16% – 84% quantile ranges for the stream parameters, in Figure 6(a). We present the resulting model’s on-sky distribution and compare it to the filtered stellar density map in Figure 7(a). Method 1 identifies four peaks in the stellar density at $\sim -6^\circ$, $\sim -1^\circ$, $\sim 2.5^\circ$, and $\sim 7^\circ$ (peaks A, B, C, and D respectively), although the uncertainties are substantial. Method 1 also finds 300S to be narrow ($w \leq 0.6^\circ$) with relatively consistent width except for a peak in width at $\phi_1 \simeq -3^\circ$. We discuss this peak in greater detail in Section 6. Generally, the uncertainties on all of the fit parameters are high and make it challenging to obtain a clear picture of 300S’s structure. For example, the 16% – 84% quantile range of $\exp(\mathcal{I}(-2.5^\circ))$ is ~ 0.15 stars/deg², which is $\sim 71\%$ of the median central stellar density, and the quantile range of $\exp(\mathcal{I}(-1^\circ))$ at the approximate location of peak B is 0.28 stars/deg² or roughly 89% of the median central stellar density. We further note that widening the proper motion filters by increasing N allows more Sgr contamination into the filters and can flatten the features while narrowing the filters can accentuate them. This sensitivity is due to the small number counts inherent in Method 1 and the strong contamination in the region. However, changing the exact selection criteria, such as the specific proper motion cut threshold or removing the HB stars, results in similar results within the substantial Poisson uncertainties.

To obtain higher number counts and lower uncertainties, we develop a second method of extracting 300S’s signal that relies purely on DECaLS photometry and therefore has significantly higher number counts. We describe this method in the next section (Section 5). We then compare and discuss our models of 300S extensively in Section 6.

5. FITTING MODELS OF STREAM MORPHOLOGY METHOD 2: FILTERING USING DECALS DR9 DATA

The low number counts and consequentially high uncertainties inherent in Method 1 limit our ability to draw conclusions from that model. This motivates the development of a model that does not require kinematic information to filter out Sgr’s influence, allowing the use of the deeper DECaLS data alone. This second method is motivated by two observations. First, Bernard et al. (2016) noticed that Sgr’s distance gradient has the opposite sign compared to 300S’s in this region. Second, as visible on our matched filter maps (see Figure 4(b)), the component of Sgr that leaks through the filter is much wider than 300S’s signal.

5.1. Motivation and Overview

In the following discussion, we define “300S matched filter” as the filter described in Section 3.2.4. Specifically, it is the matched filter with $s = 2/3$ which identifies stars’ absolute magnitudes using the 300S distance gradient given in Equation 8. This contrasts with the “Sgr matched filter” which is a matched filter based on 300S’s isochrone but that follows the Sgr distance gradient. We discuss this filter in more detail in Section 5.2.

Because of the opposite nature of their distance gradi-

ents, much of Sgr that is present in the region and visible in the unfiltered stellar density map (see Figure 1(a)) is removed after filtering (see Figure 1(b)) despite the two structures’ similarity in distance. As we later show more explicitly, the only region where Sgr contaminates the map is the vicinity of the two distance gradients’ intersection at $\phi_1 \sim -5.1^\circ$ where the matched filter is correctly positioned to also match Sgr’s overdensity.

The same effect applies in the other direction. If we filter using Sgr’s distance gradient rather than 300S’s (i.e. we use the Sgr matched filter rather than the 300S matched filter), we will capture the full extent of Sgr while limiting 300S’s extent to the small region around the distance gradients’ intersection. This result can be seen in Figure 8 where Sgr now appears across the field while 300S is limited in extent to within the red box. Because Sgr is much wider than 300S, it extends to much larger ϕ_2 values than 300S. In these regions, its signal is uncontaminated by 300S’s presence because 300S is relatively thin per Method 1. This is true even in 300S’s ϕ_1 range. Using this wider region, we can fit a model to Sgr’s morphology by applying a simple mask around the leaking 300S component that is relatively small compared to the Sgr signal of interest. We can not do the same for 300S, as the necessary Sgr mask would be very large relative to 300S, and Sgr is long and wide enough that its contamination could still be present behind most or all of 300S. In short, while Sgr is non-negligible when modeling 300S, it is large enough that if we attempt to model it first, 300S becomes negligible. This allows us to model Sgr within the relevant region.

With a Sgr model in hand, we may then account for its influence and model 300S. However, one difficulty remains. The Sgr model is fit under a matched filter that uses Sgr’s distance gradient. In most regions, this filter passes a different set of stars than 300S’s matched filter. The resulting models, then, are not directly comparable. To compare them, we must derive a transformation function that relates the Sgr model as it is seen under Sgr’s matched filter to how it would be seen under 300S’s matched filter.

With this transformation function, we can use the Sgr model as an extremely strong prior on the Sgr component of a joint model of both streams. This constraint prevents degeneracy between 300S and Sgr and allows us to extract 300S’s morphology.

We describe our empirical characterization of Sgr, including our derivation of an empirical distance gradient and stream model, in Section 5.2. Next, we derive the transformation function in Section 5.3. Finally, we combine the Sgr model and the transformation function to produce and fit a joint model of Sgr and 300S in Section 5.4.

5.2. Empirical Characterization of Sgr

We begin our analysis by empirically characterizing Sgr. This way, we may later use our Sgr model to account for its contamination into the 300S stellar density map. We perform our characterization of Sgr in much the same way as we preliminarily characterized 300S in Section 3.

5.2.1. Matched Filter Search and Coordinate System

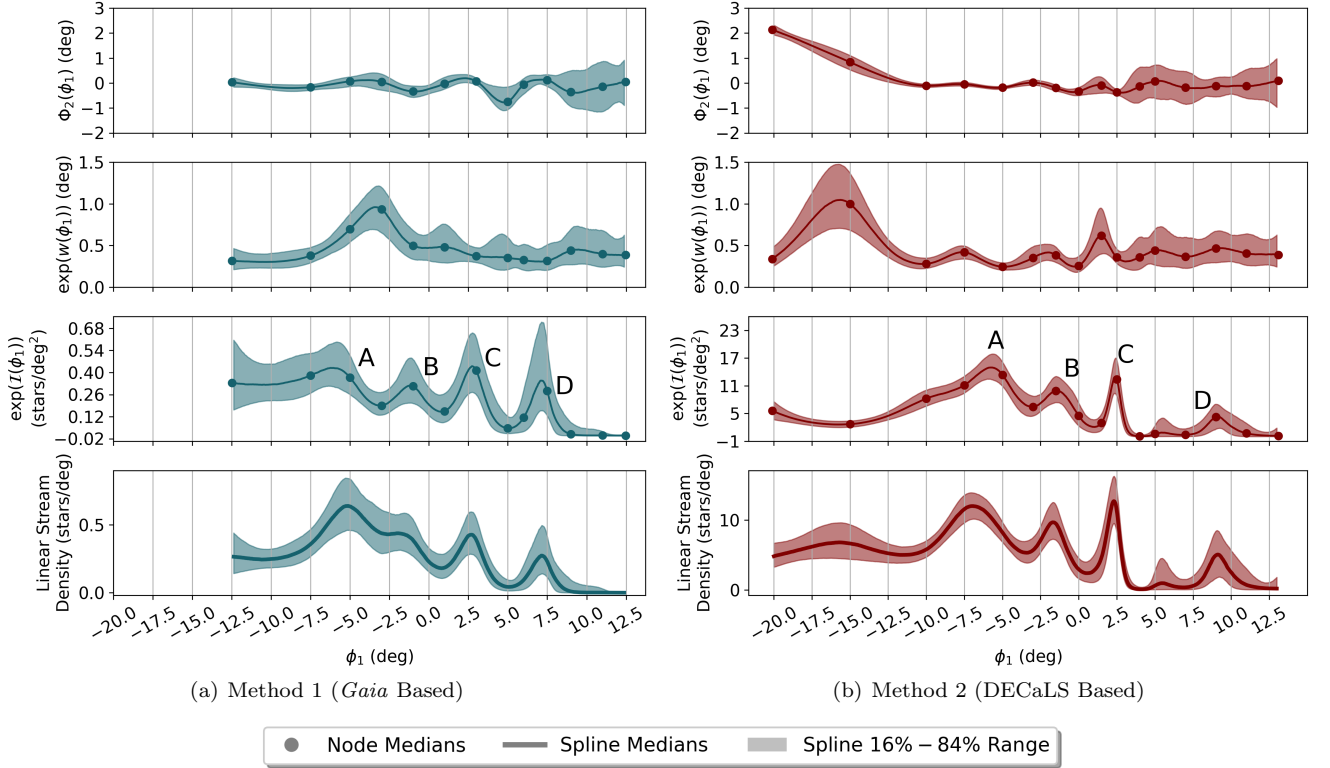


Figure 6. Resulting spline models for both methods of signal extraction. The top plots correspond to $\Phi_2(\phi_1)$ as the ϕ_2 position of 300S’s track. The second plots show $\exp(w(\phi_1))$ as the Gaussian width of the stream. The third plots are $\exp(\mathcal{I}(\phi_1))$ as the stream’s central stellar density. The locations of peaks A, B, C, and D are labeled. Both \mathcal{I} and w are fit as splines in log space and their splines and quantile ranges are subsequently transformed to linear space. Finally, the fourth plots show the linear stream density. (a) Method 1 of signal extraction that uses kinematic information from *Gaia* DR3 in addition to DECaLS DR9 photometry (Section 4). (b) Method 2 of signal extraction that purely uses photometric information from DECaLS DR9 (Section 5). We compare the tracks more directly in Figure 14.

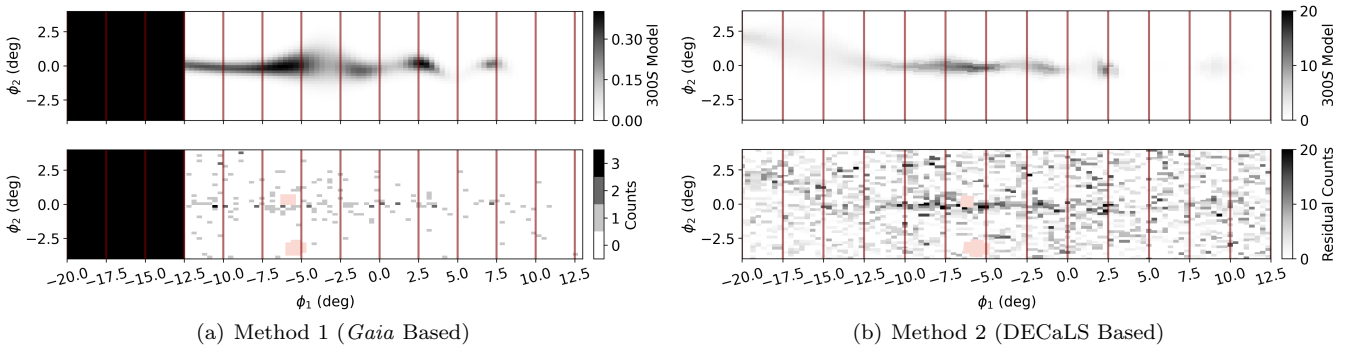


Figure 7. Comparison between the filtered stellar density maps and stream models produced through our two methods of filtering Sgr contamination. (a) Method 1 of signal extraction. The top panel is the 300S component of the model produced by Method 1. The bottom panel is the filtered stellar density map in the vicinity of 300S. The region $\phi_1 < -12.5^\circ$ is excluded from Method 1 due to Sgr contamination. (b) Method 2 of signal extraction. The top panel is the 300S component of the model produced by Method 2. The bottom panel is the background and Sgr subtracted stellar density map in the vicinity of 300S. The red shaded regions are the object masks.

We use the same matched filter for Sgr as we did for 300S, except we set $s = 1/6$. We do not change the isochrone parameters for our Sgr filter because we want to mimic Sgr’s influence on 300S’s signal as closely as possible. We set s lower for Sgr than for 300S to increase the purity of the signal. Specifically, we wish to maximally reduce the contamination from 300S into the Sgr density map. This contamination occurs in a region around where the two objects’ distance gradients intersect. By

reducing the magnitude range of the matched filter, we are limiting where the filter will overlap 300S’s distance, decreasing the size of the region it contaminates. Further, as Sgr is much larger than 300S, this thinner filter still passes enough signal to characterize the stream.

We define a local Sgr coordinate system in a manner similar to our definition of 300S’s coordinate system in Section 3.1. We place two endpoints with (R.A., Decl.) of $(145.0^\circ, 19.5^\circ)$ and $(168.0^\circ, 16.0^\circ)$ on each end of the

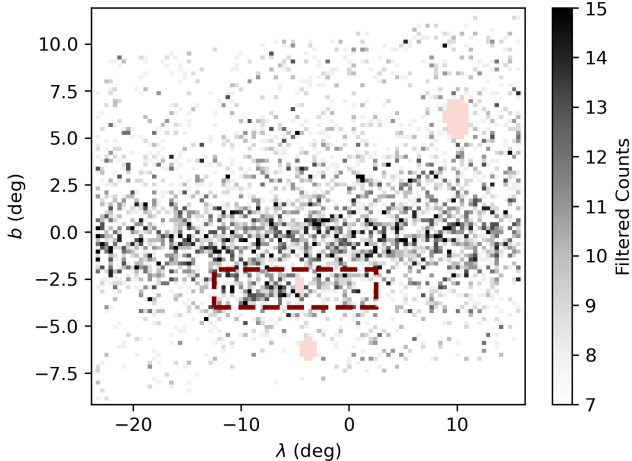


Figure 8. Filtered stellar density map of Sgr using the Sgr distance gradient derived herein and the Sgr matched filter ($s = 1/6$). The red box represents the 300S mask which prevents cross-contamination. 300S can be seen as the localized overdensity within the mask. The overlap between the mask and the Sgr overdensity is minimal, suggesting that a strong fit may be achieved despite the mask. This allows us to model and account for the Sgr contamination.

visual extent of Sgr in the unfiltered density map (Figure 1(a)). Performing the same transformation as described in Section 3.1, we find the transformation matrix

$$R_{\text{sgr}} = \begin{bmatrix} -0.87248158 & 0.37730332 & 0.31051265 \\ -0.43722902 & -0.88653053 & -0.15130899 \\ 0.21818955 & -0.26777945 & 0.93844951 \end{bmatrix} \quad (16)$$

We describe this coordinate system as λ, b coordinates to distinguish it from the common Λ, β coordinate system used for Sgr (e.g., Vasiliev et al. 2021). We use our own λ, b coordinates rather than Λ, β because our coordinates are empirically derived specifically on the Sgr response to the 300S matched filter and therefore provide a better picture for how Sgr will contaminate 300S in this particular region. Both the Sgr and 300S endpoints and $\phi_2 = 0^\circ, b = 0^\circ$ axes are compared in Figure 1(a).

For reference, our ϕ_1, ϕ_2 coordinate system for 300S has its origin at Λ, β of $(129.5^\circ, 10.3^\circ)$ on the leading arm of Sgr in the Sgr coordinates of Vasiliev et al. (2021). Note that these Λ, β coordinates differ from those of Majewski et al. (2003) by the sign of Λ . Our λ, b coordinate system for Sgr has its origin at Λ, β of $(131.5^\circ, 7.9^\circ)$ also on the leading arm and at $(\phi_1, \phi_2) = (-1.4^\circ, 2.7^\circ)$.

5.2.2. Sgr Distance Gradient Through Its Matched Filter

Ramos et al. (2020) derived a distance gradient for Sgr using RRL stars found in *Gaia* DR3. However, we are specifically interested in Sgr’s response to our 300S matched filter. Therefore, a distance gradient that is specifically tuned to the peak response of Sgr to that filter rather than a generalized distance gradient is better for our application. As such, we derive a gradient from the Sgr response to the 300S matched filter ($s = 2/3$) in this section.

We begin by selecting an on-stream region with $|b| < 0.5^\circ$. Next, we bin on-stream stars based on their λ values into bins of width $\Delta\lambda = 1^\circ$. Generally, by mea-

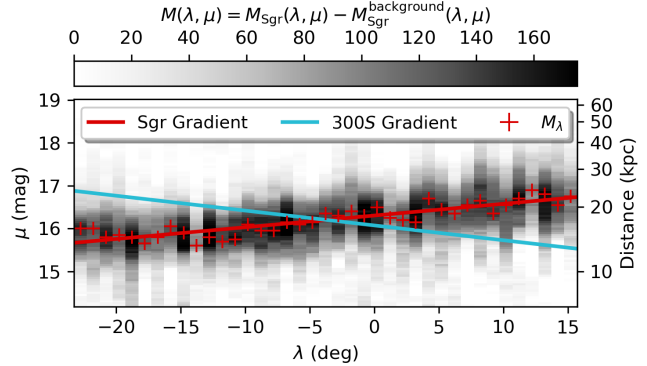


Figure 9. Derivation of empirical Sgr distance gradient. $M(\lambda, \mu)$ represents the background subtracted response to 300S’s matched filter translated to a given μ in a given λ bin. $M_\lambda = \max_\mu M(\lambda, \mu)$ is the peak of Sgr’s response to the filter at λ . We then fit Sgr’s gradient to these points.

suring the response of stars in these bins to our 300S matched filter at different distance moduli, we can identify the distance of the peak response versus the λ of the bin. We can then fit a linear function to these peak responses. Specifically, we compute the match $M_{\text{Sgr}}(\lambda, \mu)$ as the number of stars in the $\lambda \rightarrow \lambda + \Delta\lambda$ bin that fall inside the filter’s color-magnitude mask when shifted to μ . We consider μ values from 14.2 to 19 (6.9 – 63.1 kpc) with $\Delta\mu = 0.05$ for each λ bin. We subtract background by also considering bins with $|b - b_{\text{background}}| < 0.5^\circ$ for $b_{\text{background}} = -5^\circ, +4.5^\circ$. These values were chosen to avoid intersection with the masked regions or 300S. We then compute $M_{\text{Sgr}}^{(\text{background})}(\lambda, \mu)$ by linearly interpolating the matches in these two background regions to $b = 0^\circ$ and obtain a final match $M(\lambda, \mu) = M_{\text{Sgr}}(\lambda, \mu) - M_{\text{Sgr}}^{(\text{background})}(\lambda, \mu)$. We then find the peak response by taking $M_\lambda = \max_\mu M(\lambda, \mu)$ for each λ and fit a linear function to the points (λ, M_λ) . This procedure results in a linear function

$$\mu_{\text{sgr}}(\lambda) = 0.027\lambda + 16.30 \quad (17)$$

which we plot on top of $M(\lambda, \mu)$ and the 300S distance gradient in Figure 9. We also show the values of M_λ , which closely follow the derived gradient. The 300S gradient in the figure is derived by transforming the set of points $(\lambda, 0)$ into (ϕ_1, ϕ_2) and calculating $\mu_{300S}(\phi_1)$ using Equation 8.

As seen in Figure 9, the distance moduli overlap at $\lambda \simeq -3.7^\circ$ or $\phi_1 \simeq -5.1^\circ$. This position is close to the center of the Sgr overdensity visible in the matched filter map of 300S in Figure 4(b).

5.2.3. Modeling Sgr’s Morphology

We model Sgr’s morphology using a method similar to that which we used to model 300S’s morphology in Section 4. We use the Sgr matched filter ($s = 1/6$) and the distance gradient derived in the previous section to create a filtered stellar density map in λ, b coordinates with bins of size $\Delta\lambda = 0.4^\circ, \Delta b = 0.2^\circ$. To simplify the region, we only consider $\phi_2 > -5^\circ$. We show this map in Figure 8.

300S is visible in this map as the small overdensity at $\lambda \simeq -5^\circ, b \simeq -3^\circ$. In order to remove its influence on

the Sgr empirical model, we mask the region defined by a rectangle at $\lambda = -12.5^\circ$, $b = -4^\circ$ with a width of 15° and height of 2° . This mask is also shown in Figure 8. We additionally mask the objects described in Section 2. As seen in Figure 8, the overlap between the 300S mask and the Sgr overdensity is minimal. This implies that we can still fit a good model of Sgr despite the mask.

We then fit the same cubic spline based model onto this density map as we used in Section 4, except in this case all of the parameters are in terms of λ rather than ϕ_1 and $\Phi_2(\phi_1)$ is replaced by $\mathcal{B}(\lambda)$ as the b position of Sgr’s track. In this case, we use 7 nodes for $\mathcal{I}(\lambda)$, $w(\lambda)$, and $\mathcal{B}(\lambda)$. We use the same priors as Kopusov et al. (2019) for the Sgr model: $\mathcal{N}(0, 2.5)$ for $\mathcal{B}(\lambda)$ and $\mathcal{N}(\log 0.9, 0.5)$ for $w(\lambda)$. We use 3 nodes for $\vec{\mathcal{B}}(\lambda)$ to avoid degeneracies between the background and the wide Sgr stream. We again run the model for 700 warmup iterations and 800 sampling iterations and again find a satisfactory $\hat{R} < 1.1$ for all parameters, indicating convergence (Gelman & Rubin 1992).⁶

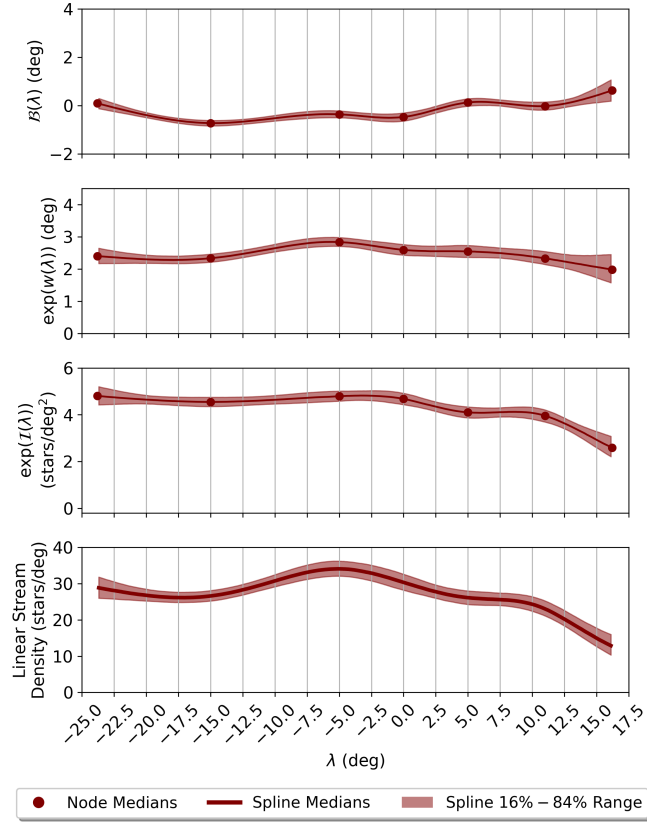


Figure 10. Resulting spline model for Sgr. The first plot corresponds to $\mathcal{B}(\lambda)$, the b position of Sgr’s track. The second plot demonstrates $\exp(w(\lambda))$ as the Gaussian stream width. The third plot shows $\exp(\mathcal{I}(\lambda))$, the central stellar density of Sgr. As in Figure 6, both \mathcal{I} and w are fit in log space and their splines and quantile ranges are then transformed to linear space. The fourth plot shows the linear stream density. We set the y scale of the first plot to be similar to that of Figure 6 and set the lower bounds of the remaining plots at zero to emphasize the relative homogeneity of the Sgr model across the relevant region.

⁶ We again made use of STAN-SPLINES, <https://zenodo.org/records/14163685>, an implementation of natural cubic splines in STAN (Kopusov et al. 2019).

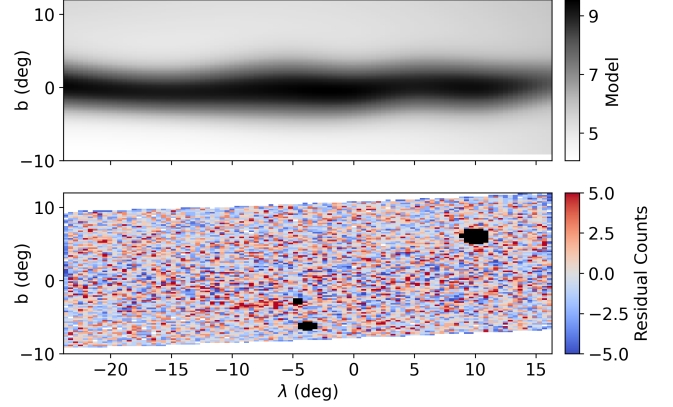


Figure 11. Sgr stream model and residual map. 300S is clearly visible as the overdensity in the residual map at $\lambda \simeq -5^\circ$, $b \simeq -3^\circ$. The lack of any large structures within the residual map except for 300S indicates that little Sgr structure will be unaccounted for by the model.

We show the resulting splines for Sgr’s model in Figure 10. Sgr’s width is very consistent in the region of interest. Between $-15^\circ \leq \lambda \leq 10^\circ$ where Sgr contaminates the 300S map, Sgr’s width changes by $\sim 0.5^\circ$ and the track remains within $|b| \lesssim 0.7^\circ$. For reference, the smallest $|b|$ value of the $\phi_2 = 0^\circ$ line in this region is $|b| = 1.9^\circ$. This consistency suggests that interpolating the Sgr model into the masked region is a reasonable assumption. This is further supported by the lack of any clear, large overdensities in the residual map except for 300S, as seen in Figure 11.

5.3. Deriving the Transformation Function Between the Map Under Sgr’s Distance Gradient and 300S’s

To use the Sgr model we derived in Section 5.2 to account for Sgr contamination in the 300S density map, we must account for the difference in the filters used to generate the Sgr model and the 300S stellar density map. In other words, if the empirical model of Sgr is the “true” underlying stream, we must know what aspects of it would pass through the 300S matched filter into the 300S density map. In this section, we empirically derive a function T that will perform this transformation. Specifically, if $\Lambda_{\text{Sgr}}^{\text{Sgr filter}}(\lambda, b)$ is the underlying bin-wise Poisson rate component for Sgr under the Sgr matched filter (as described in Section 5.2.3) and $\Lambda_{\text{Sgr}}^{300\text{S filter}}(\lambda, b)$ is the visible bin-wise Poisson rate for Sgr under the 300S matched filter, we write

$$\Lambda_{\text{Sgr}}^{300\text{S Filter}} = T(\lambda, b) \times \Lambda_{\text{Sgr}}^{\text{Sgr Filter}} \quad (18)$$

where $T(\lambda, b)$ is some function. We can further constrain $T(\lambda, b)$. We assume that Sgr’s normalized distribution in color-magnitude space is constant – or that its overall distribution is constant up to scalar – within a given λ cross section. One reason this assumption could fail is a metallicity gradient in Sgr (e.g., Hayes et al. 2020; Limberg et al. 2023), but we do not expect this to be significant. We anticipate internal stellar population variations in Sgr to be negligible for our purposes. Using a large sample of RGB stars, Cunningham et al. (2024) fit a metallicity gradient to Sgr in

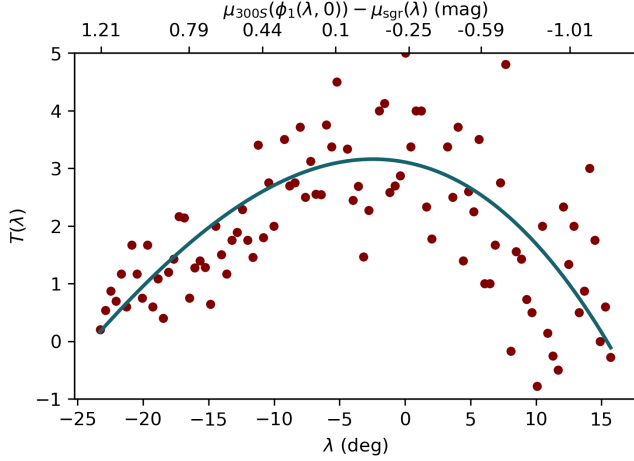


Figure 12. Fit of transformation function $T(\lambda)$. The red circles represent the empirical ratio $\Lambda_{\text{Sgr}}^{300\text{S Filter}} / \Lambda_{\text{Sgr}}^{\text{Sgr Filter}}$ calculated using Equation 20. By multiplying the Sgr model by our fit of $T(\lambda)$, we are able to mimic how Sgr leaks through 300S’s matched filter. For visualization purposes, we exclude five outlier points with $T(\lambda) > 5$ from this plot. These outliers and the points with negative $T(\lambda)$ likely originate from abnormal values of either the foreground or background.

both Λ and β . On the leading arm in the north where the origins of both of our coordinate systems are, they found $\nabla [\text{Fe}/\text{H}] = [-0.00125, -0.0178]$ dex/deg. Over the $\sim 6^\circ$ in β within a given λ cross-section, Sgr’s metallicity changes on the order of 0.1 dex. The corresponding changes in the color-magnitude distribution are negligible compared to the width of our matched filters, especially along the main sequence.

To use this assumption to constrain $T(\lambda)$, consider a set of bins at some λ . By assumption, the density of Sgr is fixed up to scalar multiplier in color-magnitude space at this λ . To be precise, let $D_\lambda(g-r, g)$ be the normalized distribution. Then we may write the distribution within a specific (λ, b) bin as $S_\lambda(b)D_\lambda(g-r, g)$ where S_λ is the b dependent scalar. Note that the operations of multiplying by the scalar $S_\lambda(b)$ and applying a matched filter F_μ commute, i.e., the density of stars Λ_{Sgr}^F matched to the filter is $\Lambda_{\text{Sgr}}^F = F_\mu(S_\lambda(b)D_\lambda(g-r, g)) = S_\lambda(b)F_\mu(D_\lambda(g-r, g))$. This implies that, given a (λ, b) bin, Equation 18 may be rewritten as:

$$\begin{aligned} T(\lambda, b) &= \frac{\Lambda_{\text{Sgr}}^{300\text{S Filter}}}{\Lambda_{\text{Sgr}}^{\text{Sgr Filter}}} = \frac{F_{\mu(\phi_1)}^{300\text{S}}(S_\lambda(b)D_\lambda(g-r, g))}{F_{\mu'(\lambda)}^{\text{Sgr}}(S_\lambda(b)D_\lambda(g-r, g))} \\ &= \frac{S_\lambda(b)}{S_\lambda(b)} \cdot \frac{F_{\mu(\phi_1)}^{300\text{S}}(D_\lambda(g-r, g))}{F_{\mu'(\lambda)}^{\text{Sgr}}(D_\lambda(g-r, g))} = \frac{F_{\mu(\phi_1)}^{300\text{S}}(D_\lambda(g-r, g))}{F_{\mu'(\lambda)}^{\text{Sgr}}(D_\lambda(g-r, g))} \end{aligned} \quad (19)$$

Further, the only spatial dependence the filters have is their vertical translations $\mu(\phi_1)$ and $\mu'(\lambda)$ due to their respective distance gradients. This implies that $F_\mu(D_\lambda(g-r, g))$ only depends on D_λ ’s relation to λ ; and the filters’ dependence on the distance gradients. So the variables involved are λ , $\mu'(\lambda) = \mu_{\text{Sgr}}(\lambda)$, and $\mu(\phi_1) = \mu_{300\text{S}}(\phi_1(\lambda, b))$.

Because of the similarity in the stream tracks, we may

Table 3
Coefficients for the Fit of $T(\lambda)$.

a_0	a_1	a_2	a_3
3.10620	-0.04286	-0.00908	-0.00008

further assume that ϕ_1 is a function purely of λ near $b = 0^\circ$. Along the $b = 0^\circ$ line, this assumption is exact. In the region $\lambda = -25^\circ$ to $\lambda = 15^\circ$, the quantity $|\phi_1(\lambda, b_1) - \phi_1(\lambda, b_2)|$ is $< 0.31^\circ \forall b_1, b_2 \in [-2^\circ, 2^\circ]$. This corresponds to a difference in $\mu_{300\text{S}}$ of 0.01. When $b_1, b_2 \in [-6^\circ, 2^\circ]$ which includes 300S, this quantity is bounded by 0.63° corresponding to $\Delta\mu_{300\text{S}} = 0.02$. In both cases, $\Delta\mu_{300\text{S}}$ is well under the width of 300S’s matched filter.

Therefore, it is reasonable to assume $F_{\mu(\phi_1)}^{300\text{S}}(D_\lambda(g-r, g))$ and $F_{\mu'(\lambda)}^{\text{Sgr}}(D_\lambda(g-r, g))$ are functions only of λ . By the above discussion, it is then reasonable to assume that T only depends on λ in this region. Therefore, we may write $T(\lambda, b) = T(\lambda)$.⁷

We empirically derive $T(\lambda)$ by comparing the stellar density map of Sgr as produced by 300S’s matched filter to that produced by Sgr’s filter. To begin, we compute a comparable density map for 300S’s filter by binning matching stars into the same (λ, b) bins that we used for Sgr’s density map in Section 5.2. Next, we perform the following reduction for both maps. Given a λ value, we take the median count over the corresponding bins with $|b_{\text{bin}}| < 1.5^\circ$ to reduce the impact of stochastic density fluctuations in the ratio T . We call these foreground medians $C_{300\text{S}}(\lambda)$ and $C_{\text{Sgr}}(\lambda)$ for 300S and Sgr’s density maps respectively. We also compute off-Sgr backgrounds as the average of the backgrounds at two locations. Specifically, we calculate the medians of same- λ bins for $|b_{\text{bin}} + b_{\text{background}}| < 1.5^\circ$ with the two constraints $b_{\text{background}} = 6^\circ, -6^\circ$ for each map. We then calculate the average of the binned counts between these two values of $b_{\text{background}}$ to obtain a λ -dependent background for both 300S and Sgr’s maps. We call these background values $B_{300\text{S}}(\lambda)$ and $B_{\text{Sgr}}(\lambda)$ respectively. Then we can calculate the ratio

$$T(\lambda) = \frac{\Lambda_{\text{Sgr}}^{300\text{S Filter}}}{\Lambda_{\text{Sgr}}^{\text{Sgr Filter}}} = \frac{C_{300\text{S}} - B_{300\text{S}}}{C_{\text{Sgr}} - B_{\text{Sgr}}} \quad (20)$$

at each λ -bin.

We fit a cubic polynomial to this ratio for use in our final 300S model. The fit is shown in Figure 12 and the

⁷ With these assumptions, there is a closely related description. By the assumption that the color-magnitude distribution is constant up to scalar in b , we can write the filtered signal

$$\Lambda_{\text{Sgr}}^{\text{Filter}} = I_{\text{Sgr}}(\lambda, b) \times f_{\text{Sgr}}^{\text{Filter}}(\lambda)$$

where $I_{\text{Sgr}}(\lambda, b)$ represents the integrated stellar density in a bin and $f_{\text{Sgr}}^{\text{Filter}}(\lambda)$ represents the fraction of the Sgr signal that passes through the filter at λ . In this depiction, f contains information about both the filter and the shape of the color-magnitude distribution at λ . The intensity I_{Sgr} contains information about the scaling of the distribution. Then again we find

$$T = \frac{\Lambda_{\text{Sgr}}^{300\text{S Filter}}}{\Lambda_{\text{Sgr}}^{\text{Sgr Filter}}} = \frac{I_{\text{Sgr}}(\lambda, b) \times f_{\text{Sgr}}^{300\text{S Filter}}(\lambda)}{I_{\text{Sgr}}(\lambda, b) \times f_{\text{Sgr}}^{\text{Sgr Filter}}(\lambda)}$$

is purely a function of λ .

coefficients are provided in Table 3.

We can now virtually pass the Sgr model through the 300S matched filter by multiplying it by $T(\lambda)$. The result of this transformation on the Sgr model can be seen in Figure 13(a). Here, the Sgr model appears similarly to the Sgr overdensity in Figure 4(b). It peaks around $\phi_1 \simeq -5^\circ$ and decays in both directions as $|\Delta\mu|$ increases. This ϕ_1 is close to the intersection of the distance gradients, as can be seen in Figure 13(a). Subtracting this transformed model of Sgr from 300S’s stellar density map, we obtain the map in Figure 13(b). In this map, we can clearly see 300S as an elongated overdensity around $\phi_2 = 0^\circ$ and Sgr’s contamination is no longer clearly visible. 300S is especially visible when we also subtract the background, as seen in Figures 13(c) and 13(d).

5.4. Modeling 300S’s morphology

Using the transformation of the Sgr model from the previous section, we are able to model 300S itself. Like in our model using *Gaia* in Section 4, we define $\mathcal{I}(\phi_1)$, $\Phi_2(\phi_1)$, and $w(\phi_1)$ as the log central stellar density, ϕ_2 position, and log Gaussian width respectively for 300S. Using these components, we write the stream density $\Lambda_{300S}(\phi_1)$ using Equation 14. We similarly continue to use a linear background model, $\Lambda_{\text{background}}(\phi_1)$ with $\vec{B} \in \mathbb{R}^2$.

To account for Sgr, we add to this model a Sgr component, $\Lambda_{\text{Sgr}}(\lambda)$, like the one we fit in Section 5.2. This model is parameterized by $\mathcal{I}_{\text{Sgr}}(\lambda)$, $\mathcal{B}_{\text{Sgr}}(\lambda)$, and $w_{\text{Sgr}}(\lambda)$ as Sgr’s log central stellar density, b position, and log Gaussian width respectively. To avoid the substantial degeneracy between Sgr’s components and 300S’s, we use the pure Sgr model and transformation function we derived in the previous sections to constrain the Sgr component. Using the Sgr model, we place smooth priors of $\mathcal{N}(\mu_{\text{Sgr}}, \sigma_{\text{Sgr}})$ on each node value where μ_{Sgr} and σ_{Sgr} are the median and standard deviation of the corresponding node’s value in the pure Sgr model as fit in Section 5.2. We additionally require that this value is within $50\sigma_{\text{Sgr}}$ of the corresponding value in the Sgr model. Then, we include the transformation function within the model to write the full density as

$$\begin{aligned} \Lambda(\phi_1, \phi_2) &= \Lambda_{300S}(\phi_1, \phi_2) \\ &\quad + \Lambda_{\text{background}}(\phi_1, \phi_2) \\ &\quad + T(\lambda(\phi_1, \phi_2)) \times \Lambda_{\text{Sgr}}(\lambda(\phi_1, \phi_2), b(\phi_1, \phi_2)) \end{aligned} \quad (21)$$

We use the same priors for the 300S nodes as in Section 4: $\mathcal{N}(0, 1)$ for $\Phi_2(\phi_1)$ and $\mathcal{N}(\log 0.4, 0.5)$ for $w(\phi_1)$. Like with our other stream models, we assume that the stellar density is binwise Poisson distributed with a spatially varying rate. We then define the likelihood using Equation 15 and sample the posterior distribution using STAN. We perform this sampling using the same bins that we have used in the rest of this section (described in Section 5.2) to maintain consistency between the Sgr model, $T(\lambda)$, and the 300S model. We use 16 nodes for the stream parameters $\mathcal{I}(\phi_1)$, $w(\phi_1)$, and $\Phi_2(\phi_1)$, the same nodes as in Section 5.2 for $\mathcal{I}_{\text{Sgr}}(\lambda)$, $w_{\text{Sgr}}(\lambda)$, and $\mathcal{B}_{\text{Sgr}}(\lambda)$, and 6 nodes for the background parameter \vec{B} . The specific choice of node positions does not significantly alter the resulting fit. To simplify the background, we con-

strain the region to $\phi_2 \in [-5^\circ, 5^\circ]$. We run the model for 700 warm-up iterations and 800 sampling iterations using 4 chains.⁸ As with our other models, we achieve a satisfactory $\hat{R} < 1.1$ on each parameter, indicating convergence (Gelman & Rubin 1992).

We present the resulting median splines and corresponding 16% – 84% quantile ranges for the stream parameters extracted using our second method in Figure 6(b). We compare the stream component of the model with the background and Sgr subtracted density map in Figure 7(b). We discuss this model and compare it to the *Gaia*-based model in Section 6 and Figure 14.

6. DISCUSSION OF MODELS

Generally, the two methods of signal extraction that we apply to model 300S lead to agreeing central stellar densities along the majority of the track, as can be seen in the comparison in Figure 14 and the splines in Figure 6.⁹ This agreement is especially apparent in the region of highest stellar density from $\phi_1 \simeq -7^\circ$ to $\simeq 2.5^\circ$. They also lead to agreeing tracks and half-widths for the majority of the stream. Because the two methods used different datasets and filtering methodologies, this agreement indicates that our fits are robust against contamination.

6.1. Stream Features Present Under Both Methods

Generally, the models agree that 300S is an angularly long (though relatively physically short) thin stream, whose track closely traces a great circle. Stream length is related to both the age and energy distribution of the stream (Johnston et al. 2001). Method 1 detects 300S between -12.5° and $\sim 8^\circ$ and Method 2 extends that measurement to identify the stream within $\sim -20^\circ$ and $\sim 12^\circ$. At 32° and a distance of 17 kpc, 300S has a physical length of 9.7 kpc. This is much shorter than the Jet and GD-1 streams, the other known globular cluster streams on retrograde orbits (which have lengths of ~ 16 kpc and ~ 15.4 kpc respectively, Ferguson et al. 2021 and Malhan & Ibata 2018; Price-Whelan & Bonaca 2018; Webb & Bovy 2019; de Boer et al. 2020).

The models also agree that 300S is thin and its track is close to a great circle. In the region $\phi_1 \in [-12.5^\circ, 13.0^\circ]$, Method 2’s median Gaussian width is $\lesssim 0.6^\circ$ and its $|\phi_2| \lesssim 0.4^\circ$. At a distance of 17 kpc, this width corresponds to 178 pc which is reasonable for a globular cluster stream ($w \sim 100$ pc) and extreme for a dwarf galaxy stream ($w \gtrsim 500$ pc, Patrick et al. 2022). This further verifies the conclusions of both Li et al. (2022)’s chemical and kinematic analysis and Usman et al. (2024)’s further chemical analysis that 300S’s progenitor is a globular cluster.

We also identify oscillations in $\mathcal{I}(\phi_1)$ with four peaks at $\phi_1 \simeq -6^\circ$, -1° , 2.5° , and 8° (peaks A, B, C, and D respectively). The positions of these peaks are shown in Figure 14 with arrows. The specific coordinates

⁸ We again made use of STAN-SPLINES: <https://zenodo.org/records/14163685> (Koposov et al. 2019).

⁹ We include tables of the 300S spline nodes’ ϕ_1 positions and their corresponding values in Appendices A and C the end of this paper. We also include this information for the Sgr spline nodes in Appendix B. We share the complete model results and machine-readable tables at <https://zenodo.org/records/15391938>.

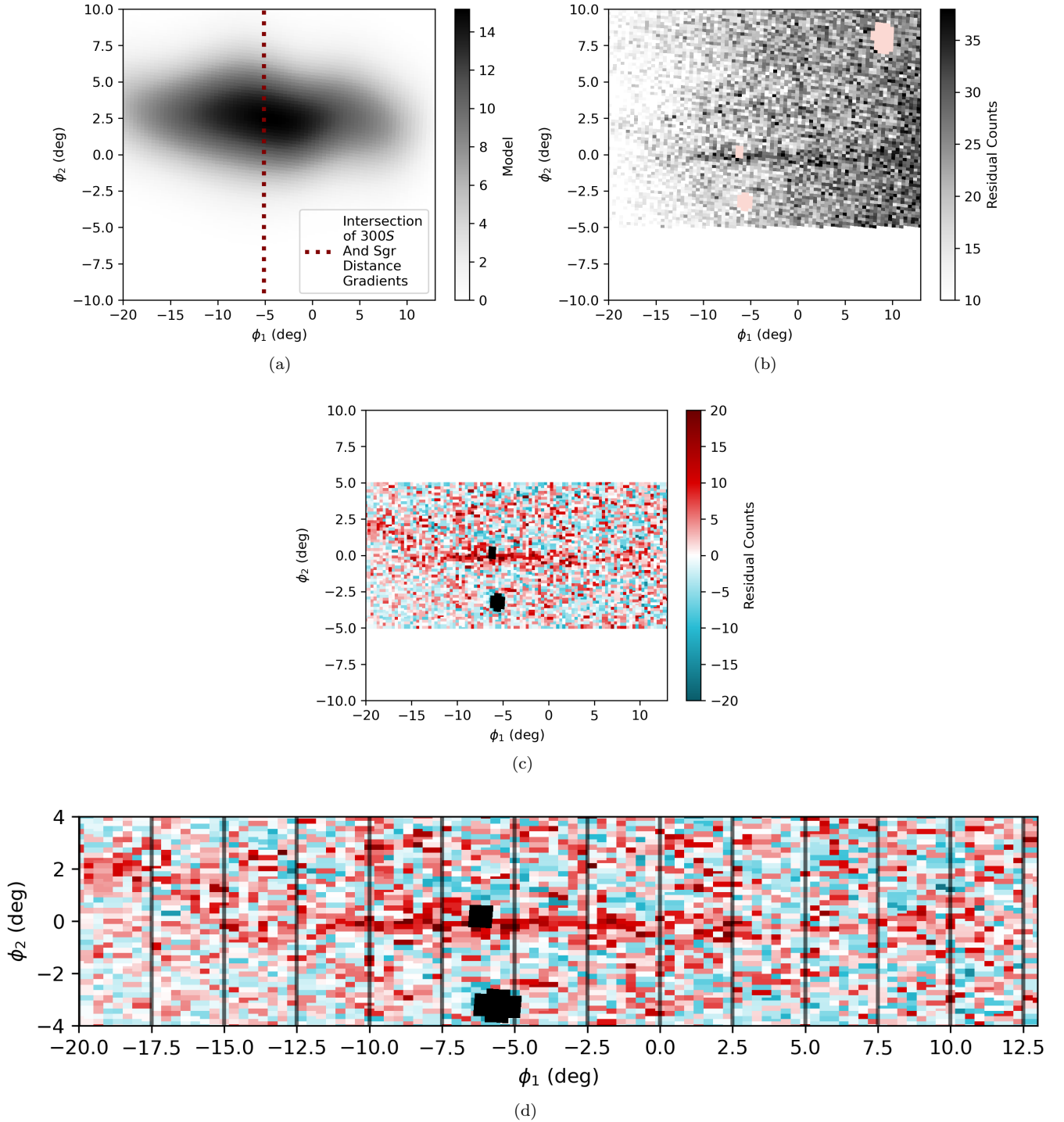


Figure 13. Impact of $T(\lambda)$ on Sgr and subsequent subtraction. (a) The Sgr model (as shown in Figure 11) after being transformed using $T(\lambda)$. Note how the intensity peaks near the intersection of 300S and Sgr’s distance gradients and falls off on either side as the gradients diverge. (b) The stellar density map of 300S with the transformed Sgr model subtracted out. 300S remains clearly present in this density map as an overdensity along $\phi_2 = 0^\circ$ while the Sgr overdensity present in Figure 4(b) has been removed. The region below $\phi_2 = -5^\circ$ has been removed because it is excluded from the Sgr model fit. The red shaded regions are the object masks. We keep the proportions of Figure 4(b) in this figure for reference. (c) The interpolated stellar density map of 300S after both $\Lambda_{\text{background}}$ and the transformed Λ_{Sgr} as fit in Section 5.4 have been subtracted out. In (c) and (d), we apply nearest neighbor interpolation to transform the λ, b bins into ϕ_1, ϕ_2 bins for easier comparison. The black overlays are the bin masks due to the object masks applied to the datasets in Section 2. As with the Sgr model, extraneous regions are removed in the fit to emphasize the stream signal. Only $\phi_2 \in [-5^\circ, 5^\circ]$ is shown to match the region 300S’s model is fit upon. Again, we maintain the proportions of the map for easy comparison. (d) A closer look at the resulting stream signal after both $\Lambda_{\text{background}}$ and the transformed Λ_{Sgr} have been subtracted out. The bin coloration is the same as in (c). 300S is now clear against the residual map. No other large structures within the residual map are visible, indicating that the contamination in the region is being correctly described. Further, many of the major stream features are clearly visible in this map. The four peaks in the stream density are visible at $\phi_1 \simeq -6^\circ, -1^\circ, 2.5^\circ, 8^\circ$ (peaks A, B, C, and D respectively). The possible gap can be seen as the blue region between $\phi_1 \simeq 2.5^\circ$ and $\phi_1 \simeq 5^\circ - 7.5^\circ$. The kink is visible as the angled overdensity visible between $\phi_1 = -20^\circ$ to -12.5° .

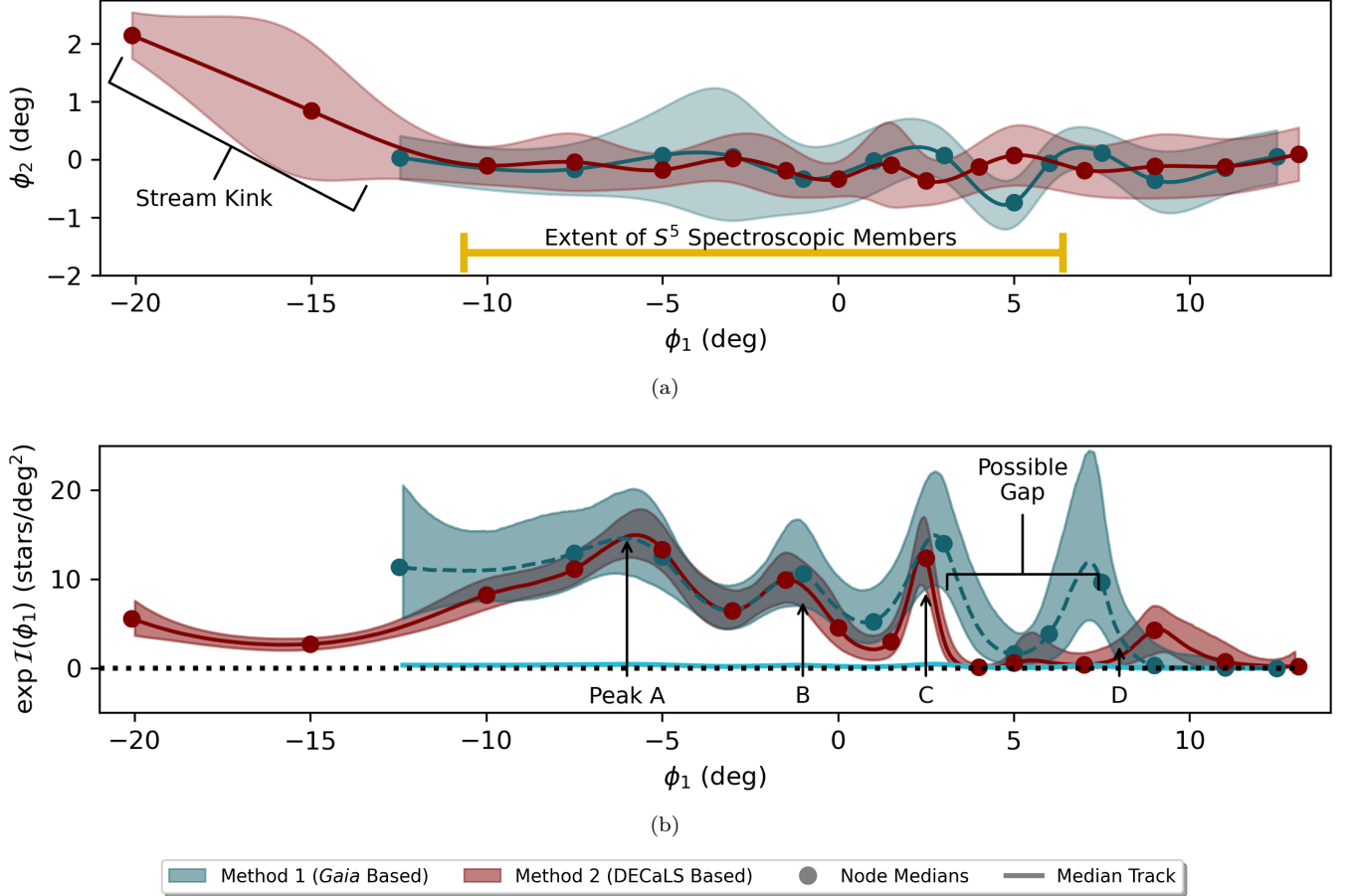


Figure 14. Comparison of modeled stream morphologies. (a) The on-sky image of the stream models using the median spline values shown in Figure 6. The shaded regions represent the stream’s full width at half maximum as identified by the respective model. We further include the ϕ_1 range of the S^5 members we use to calculate the distance gradient and the proper motion filters as the yellow line. 300S’s kink is labeled. (b) The $\exp \mathcal{I}(\phi_1)$ splines overplotted for both models. The positions of peaks A, B, C, and D as well as the potential gap are labeled. The dotted horizontal line is at 0 for reference. As seen in Figure 6, the two central stellar density splines have inherently different characteristic magnitudes. To compare their structures here, we scale the Method 1 spline by $\max_{\phi_1}(\exp \mathcal{I}_2) / \max_{\phi_1}(\exp \mathcal{I}_1)$ to force the corresponding peaks of the splines to line up. The Method 1 spline with its original magnitude can be seen as the solid light blue line. The similarity in structure of these two splines despite their different derivations indicates that the resulting stream density profile is robust and that our second method of signal extraction (Section 5) was successful.

are identified by eye. These peaks are similar to the peaks found in ATLAS (Li et al. 2021), another globular cluster stream. We do note that the Orphan-Chenab (OC) stream’s track (Koposov et al. 2023) intersects the $\phi_2 = 0^\circ$ line at $\phi_1 = -2^\circ$ and the intersection of the OC stream’s full width at half maximum is $-3^\circ < \phi_1 < -1^\circ$. In the OC stream coordinate system (Koposov et al. 2019), this intersection occurs at $\phi_1^{(\text{OC})} = 83^\circ$. However, it is unlikely that the OC stream is making a significant impact on our results. At that location, Koposov et al. (2023)’s distance spline indicates that the OC stream’s distance is 25.2 kpc while our distance gradient places 300S at 16.5 kpc. Moreover, the ϕ_1 of the objects’ intersection ranges over both part of peak B and part of the trough between peaks A and B. If the OC stream were leaking through the filter, we would not expect a trough in that ϕ_1 range. Finally, the OC stream is not visible on the residual maps in Figure 13, indicating that it has a minimal influence.

One possible explanation of these oscillations is the influence of epicycles, which can lead to peaks in stellar

density (Küpper et al. 2012) and are predicted to exist in globular cluster streams (e.g., Weatherford et al. 2024). Ibata et al. (2020) use epicycles to explain similar peaks in density found in the GD-1 stellar stream. As epicycles are a potential explanation for 300S’s density peaks, are useful for constraining stream mass (Ibata et al. 2020), and are useful for indicating the progenitor’s position because they appear equally spaced from it (Küpper et al. 2008), we briefly investigate whether these density variations could be epicyclic in origin. Küpper et al. (2008) derived the following relation for the spatial period of epicyclic over-densities for a progenitor on a circular orbit

$$y_c = \frac{4\pi\Omega}{\kappa} \left(1 - \frac{4\Omega^2}{\kappa^2}\right) x_L \quad (22)$$

where Ω is the angular velocity of the progenitor, κ is the epicyclic frequency, and $x_L = (GM/(4\Omega^2 - \kappa^2))^{1/3}$ is the radius of the Lagrange point. For a Milky Way potential, Küpper et al. (2012) reduces this relation to

$y_c \approx 3\pi x_L$ using $\kappa \approx 1.4\Omega$ in the Milky Way potential (Just et al. 2009). Then, $y_c \approx 3\pi (GM/(2\Omega^2))^{1/3}$. Using these equations, we may check whether epicycles are a reasonable explanation of 300S’s periodic nature.

At present, 300S’s angular velocity Ω is $5.7 \text{ km s}^{-1} \text{ kpc}^{-1}$. This Ω is around two thirds of the stable circular angular velocity at 300S’s present day Galactic radius because of the high eccentricity of its orbit. Assuming a stellar mass of $\log_{10}(M/M_\odot) = 4.5$, the lower bound of Usman et al. (2024)’s mass bounds, the epicyclic spatial period y_c is 1.2 kpc. At 17 kpc, this corresponds to 4.1° , which is of the correct order to explain 300S’s density peaks whose average separation is $\sim 4.7^\circ$.¹⁰ This indicates that epicycles are a plausible explanation of 300S’s interesting density variations.

Unfortunately, because there is no analytic treatment of epicycles for eccentric orbits (Küpper et al. 2012) and 300S’s orbit is highly eccentric (Fu et al. 2018 and Li et al. 2022, also see Section 7.2.2), these calculations are quite approximate. Küpper et al. (2012)’s simulations found that y_c shrinks at orbital apocenter and then grows as the cluster reaches pericenter with orbit eccentricities of 0.25 and 0.5. This effect would likely be more considerable for 300S due to its higher eccentricity. Further, as discussed in Section 6.4, 300S’s progenitor’s mass was likely higher than $\log_{10}(M/M_\odot) = 4.5$, which would act to increase y_c . 300S’s density oscillations could also be residue from the complex disruption of globular clusters (Malhan et al. 2020) or other environmental interactions. Further dynamical simulations of 300S’s density peaks are necessary to formulate a conclusive explanation for the stream’s structure by shedding light on the specifics of 300S’s disruption and decisively clarifying the plausibility of an epicyclic description.

Finally, depending on the exact position of peak D and shape of peak C (see the next section), the models agree on the presence of a $\sim 3^\circ - \sim 6^\circ$ gap in the stream. This gap is on a similar angular scale as the 4° gap found in the Jet stream by Ferguson et al. (2021) but is around two-thirds the physical length. At 17 kpc, 300S’s gap is ~ 1.4 kpc long assuming an angular length equal to the average peak separation of 4.7° . Such a gap could be formed through a variety of processes including interactions with small-scale dark matter sub-halos (e.g., Bonaca et al. 2019) or other environmental features, interactions with the progenitor’s environment (e.g., Malhan et al. 2020), or the process of total progenitor disruption (e.g., Webb & Bovy 2019).

6.2. Tensions Between the Methods

Although the models generally agree on the morphology of the stream and its features, there are a few tensions. First, although both models identify peaks A, B, and C in approximately the same location and peak D between $\phi_1 \sim 7^\circ$ and $\phi_1 \sim 10^\circ$, Method 2 finds the latter structure to be at a larger ϕ_1 . It is possible that Method 1 does not fully characterize that feature due to a combination of the low count statistics inherent in the method and the relatively low peak stellar density of the feature. In fact, the bump in Method 1’s spline is

¹⁰ Using the slightly higher lower mass bound of $\log_{10}(M/M_\odot) = 4.7$ found in Section 6.4, we obtain an epicyclic angular period of 4.7 deg.

due to only a few bins in the vicinity of peak D which contain only $\sim 1 - 2$ stars each. As the S^5 catalog does not cover this structure, further spectroscopic analysis in the region will be necessary to confirm its morphology. However, given that both methods pick up a substantive structure in this region, we believe that it is a real component of the stream.

Second, despite the methods’ agreement on the presence and relative height of peak C, they disagree slightly on how rapidly the density decays as ϕ_1 increases past 2.5° . As seen in Figure 15, S^5 finds stream members in this region, indicating that the stream extends there. We find it unlikely that Method 2 fails to capture this behavior due to poor Sgr subtraction, as $T(\lambda)$ strongly suppresses Sgr in this region (see Figures 12 and 13(a)) and there is no pattern in the residuals near 300S in Figure 13(b). Moreover, we find that alternative node placements can lead Method 1 to have lower central stellar density in the region in closer agreement with Method 2, although they also increase the amplitude of Method 1’s peak C within the substantial Poisson uncertainties. We also note that without the inclusion of the horizontal branch candidates (see Section 4.1) and with a corresponding slight increase in the proper motion filter width to make up for the lost candidates, the two models also achieve closer agreement on the width and depth of the gap. Therefore, we are inconclusive on the specifics of the stream density’s decay to the right of peak C, although there is likely a gap in this region. This gap is visually apparent in Figures 13(c) and 13(d).

Third, despite the models’ agreement on the stream track and width over the majority of the stream, Method 1 identifies a widening in the stream at $-5^\circ \lesssim \phi_1 \lesssim -2.5^\circ$. This widening is due to the small collection of stars within $1^\circ \lesssim \phi_2 \lesssim 3^\circ$ in the relevant region, as seen in Figure 5(b). These stars are on the side of 300S closer to Sgr’s stream track, meaning that they are potentially contamination from the complex Sgr background population. This is reinforced by the fact that Method 2 does not identify widening in this region. The smoothly varying Sgr background used in Method 2 should not be eliminating this signal if were strongly present. Moreover, a stronger prior on the width in Method 1 of $\mathcal{N}(\log 0.4, 0.3)$ substantially reduces the widening in this region. However, these stars do pass through both the proper motion and isochrone filters described in Section 4. As these stars are outside of the S^5 footprint, we can not test their radial velocities against 300S’s distinct $\sim 300 \text{ km s}^{-1}$. Therefore, further spectroscopic followup is necessary to fully characterize this potential feature.

6.3. Kink Visible Under Method 2

Method 2 detects a “kink,” or sudden bend away from the $\phi_2 = 0^\circ$ line, in the stream track at $\phi_1 \lesssim -12.5^\circ$. As this kink is at the end of the stream where the signal is weakest, and we are unable to verify it with Method 1 due to the Sgr contamination, it could be an artifact of background mismodeling. On the other hand, as S^5 did not cover that region and therefore there are no members there, we must extrapolate our distance gradient into it. This could imply that our matched filter may be poorly extracting the kink’s signal, resulting in our under-modeling it.

The kink does not align with any other streams in

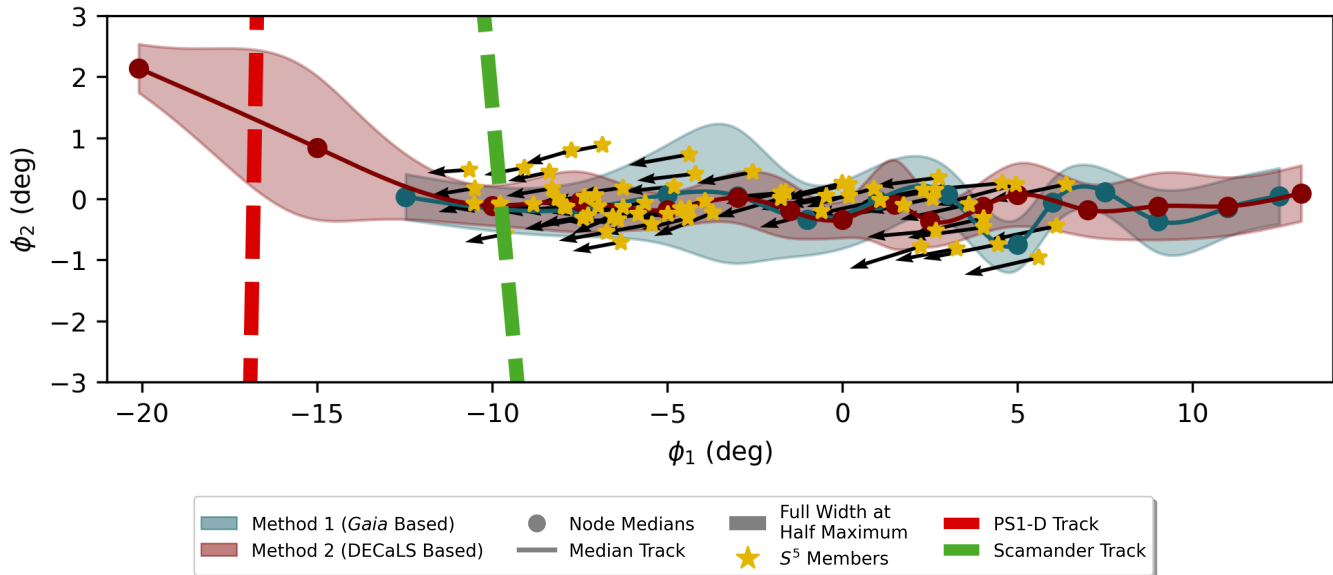


Figure 15. The positions and reflex-corrected proper motions of the S^5 member stars overplotted on the stream models. The shaded regions represent the full widths at half maximum as identified by the respective model. Reflex corrections were performed assuming the same solar motion as described in Section 7.1. Note that the members are clustered near the 3 central peaks in stellar density at peaks A, B, and C. The proper motions of the S^5 members are slightly misaligned with both models’ stream tracks. This indicates that 300S experienced a significant interaction over its lifetime. As we discuss in Section 7, we find that a close interaction with the LMC is relatively consistent with the current kinematics of 300S, as well as the kink we measure at $\phi_1 \simeq -12.5^\circ$. The GALSTREAMS tracks for Scamander and PS1-D are also included. Neither track has the correct orientation to explain the kink.

the region. Of the streams listed in the GALSTREAMS catalog (Mateu 2023), only Scamander (Grillmair 2017) and PS1-D (Bernard et al. 2016) are near the kink spatially and at a similar distance. Specifically, Scamander intersects 300S at $\phi_1 \sim -9.7^\circ$ and is at a distance of 21 kpc (Mateu 2023). Our distance gradient places 300S at 18.7 ± 1.6 kpc there. PS1-D intersects 300S at $\phi_1 \sim -16.8^\circ$ and is at a distance of 23 kpc (Mateu 2023). 300S is at 21.0 ± 2.0 kpc there. As seen in Figure 15, neither of these candidates’ GALSTREAMS tracks (Mateu 2023) are close to being in the correct orientation to explain the overdensity (also see Figure 1(d) in Grillmair 2017).

In addition, we find that 300S’s track is misaligned with the proper motions of the S^5 members. This is visible in Figure 15. Such a proper motion-stream track misalignment was also found in the OC stream (Koposov et al. 2019) and there was due to a strong interaction with the LMC. We investigate the possibility of an 300S-LMC interaction in the next section (Section 7) and find that such an interaction can both produce a kink that aligns with our empirical model and reproduce the kinematics of the S^5 members. The dynamical model provides a strong motivation for additional spectroscopic followup in the region of the kink to better clarify whether it is a real component of the stream.

6.4. The Total Mass of 300S

Using our maps of 300S, we may also consider integrated stellar density over the stream. We show the cumulative distributions in Figure 16. As Method 1 does not cover the entire footprint of the stream due to the $\phi_1 > -12.5^\circ$ requirement, we assume for the sake of comparison that if Method 1 could analyze the $\phi_1 \leq -12.5^\circ$ region, it would find the same proportion of stars as were

found using Method 2. As can be seen in Figure 16, once this adjustment is made, the two methods produce mostly agreeing distributions. This is as expected from the similarities in their $\mathcal{I}(\phi_1)$ splines. The primary difference in these distributions is in the positive ϕ_1 region where the models disagree on the exact shape of peak D. There is also worse agreement around $\phi_1 \sim -5^\circ$ in the vicinity of the stream’s widening under Method 1.

Using Method 2, we find that the S^5 members used in this work have a footprint which encapsulates around 61% of the stream stars. Around $31^{+6}_{-6}\%$ – where the reported uncertainties are the 16% and 84% quantiles respectively – are cutoff on the left where $\phi_1 \leq -10.7^\circ$. $7^{+4}_{-3}\%$ are cutoff on the right with $\phi_1 \geq 6.4^\circ$. The members used by Usman et al. (2024) from Li et al. (2022) have a slightly smaller footprint which includes around 55% of the stream stars, cutting off around $38^{+6}_{-6}\%$ on the left with $\phi_1 \leq -8.8^\circ$ and $7^{+4}_{-3}\%$ on the right with $\phi_1 \geq 6.4^\circ$.

Usman et al. (2024) found a lower limit mass of the progenitor of $\log_{10}(M/M_\odot) = 4.5$ assuming the ratio of observable to total stars within their footprint is equal to the same ratio for a Salpeter initial mass function (Salpeter 1955). As they used the members of Li et al. (2022), they further assume for the sake of a lower limit that the sample is spatially complete and do not consider stars outside of Li et al. (2022)’s footprint. Using the coverage we identify with our models, we can improve this lower bound. For the sake of a lower bound, we consider the 16% quantile on the left and the 84% quantile on the right. Using these values, we find the footprint to encapsulate around 63% of stream stars. Then we may increase this lower limit to $\log_{10}(M/M_\odot) = 4.7$. Together with Usman et al. (2024)’s upper limit, we find

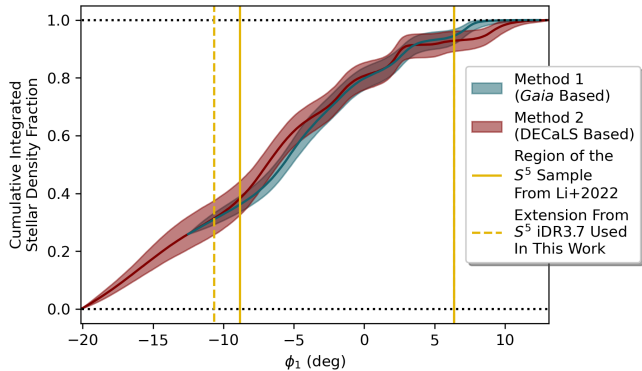


Figure 16. Integrated stellar density under both methods. The yellow lines represent the ϕ_1 range of the S^5 members. The solid lines show the range of members identified by Li et al. (2022) and used by Usman et al. (2024). The dashed line shows the extension of that region available in the S^5 iDR3.7 sample used in this work. The shaded regions represent the 16% – 84% quantile range of the integrated stellar density. To account for the lower coverage of Method 1 and make the two methods comparable, we set Method 1’s $\phi_1 = -12.5^\circ$ starting point to the integrated density fraction found by Method 2 at that ϕ_1 . Under Method 2, the S^5 members encapsulate 61% of the stream going from $\sim 31\%$ to $\sim 93\%$.

300S’s progenitor mass to be in the range $10^{4.7-4.9} M_\odot$.

7. DYNAMICAL MODELING

To better understand the origins of the kink that Method 2 identifies in 300S (see Figure 14), we consider whether 300S was influenced by the LMC. In this section, we prepare a simple dynamical model of 300S as an initial investigation of the 300S-LMC interaction. We find that the LMC likely had a strong influence on the formation of 300S. Further, our model indicates that the LMC interaction with 300S can form a kink in the stream whose angle and position relative to the remainder of the stream track matches our empirical result. This is evidence that the kink Method 2 identifies is a real feature of the stream.

7.1. Preparing the Dynamical Model

We utilize Chen et al. (2024)’s implementation of their particle spray technique in GALPY (Bovy 2015) for our dynamical model. This technique was designed specifically with globular cluster streams in mind. It produces an accurate description of test objects in phase space by sampling tracer particles from distributions found through N-body simulations that are robust against changes in progenitor and orbit parameters (Chen et al. 2024). We set the Sun’s current position and kinematics using the ASTROPY v4.0 (Price-Whelan et al. 2018) values with $d_\odot = 8.122$ kpc (GRAVITY Collaboration et al. 2018) and $v_\odot = (12.9, 245.6, 7.78)$ km s^{-1} (Reid & Brunthaler 2004; Drimmel & Poggio 2018; GRAVITY Collaboration et al. 2018). We use GALPY’s MW POTENTIAL2014 setting R_0 according to the ASTROPY v4.0 parameters and $V_c(R_0) = 236$ km s^{-1} . This setting of V_c leads to a halo virial mass of $1.05 \times 10^{12} M_\odot$ which is the mean virial mass found in recent studies of the MW (Bobylev & Baykova 2023) and leads to a reasonable value of V_\odot given the uncertainties on the quantity (Bland-Hawthorn & Gerhard 2016; Ding et al. 2019). We also find this increase in mass better reproduces the

tracks of other stellar streams. In general, however, our results don’t depend on the specific value of V_c , as expected given the flexibility of MW POTENTIAL2014 under reasonable values of R_0 and V_c (Bovy et al. 2016).

We treat the LMC potential as a Hernquist potential (Hernquist 1990) as done in Erkal et al. (2019)’s investigation of the OC stream’s LMC interaction. We fix the LMC mass as $18.4 \times 10^{10} M_\odot$ as derived in Shipp et al. (2021) and use a scale radius of 19.91 kpc such that the circular velocity at a radius of 8.7 kpc matches the measurement of van der Marel & Kallivayalil (2014) of 91.7 km s^{-1} as was assumed in Shipp et al. (2021). We note that in a more recent study, Cullinane et al. (2020) found a circular velocity of 88 km s^{-1} at a radius of 10.5 kpc. Using this value instead does not dramatically change our results. However, we present results using the circular velocity of van der Marel & Kallivayalil (2014) to maintain consistency with Shipp et al. (2021). The current day 6D phase space coordinate of the LMC used in this simulation is given in Table 4.

We treat both the LMC and MW as particulate sources for their respective potentials. For ease of implementation, we pre-compute the trajectory of the LMC and the corresponding non-inertial reference frame of the MW. We incorporate dynamical friction using the GALPY implementation of CHANDRASEKHAR DYNAMICAL FRICTION FORCE (Bovy 2015).

Given the free parameter ϕ_1 , we assume a present day progenitor position of $(\phi_1, \Phi_2(\phi_1))$ where $\Phi_2(\phi_1)$ is Method 2’s track position. We set the progenitor distance according to 300S’s distance gradient with a free offset to account for the nonlinearity of the distance gradient described in Section 7.2.3. We set the progenitor’s kinematics using quadratic fits to the S^5 member proper motions and radial velocities (see Table 1 for the coefficients). We use a progenitor mass of $\log_{10}(M/M_\odot) = 4.7$ – the new lower limit mass discussed in Section 6.4 – and set 300S’s mass profile as a Plummer profile (Plummer 1911) with a free scale radius that we set to 12.5 pc to match the width of the stream. We assume that tidal stripping began 4 Gyr ago. The current day 6D phase space coordinate of 300S’s progenitor is also given in Table 4.

In order to understand whether a LMC interaction can reproduce the kink Method 2 identifies, we set the free parameters of the ϕ_1 progenitor position and the distance offset from 300S’s distance gradient by hand to maximize agreement between the modeled stream’s on-sky track and the empirical on-sky tracks. We find that $\phi_1 = -5^\circ$ and a distance offset of 0.6 kpc produce good agreement with the empirical stream track. As visible in Figures 18(a) and 20, a distance offset of 0.6 kpc also fits the empirical distance gradient at the location of RRL-1 and roughly matches the stream overdensity in $\phi_1 - \mu$ space. Further work should attempt to fit these parameters more carefully, perhaps in a joint model with the LMC mass as in, e.g., Erkal et al. (2019), Shipp et al. (2021), and Koposov et al. (2023).

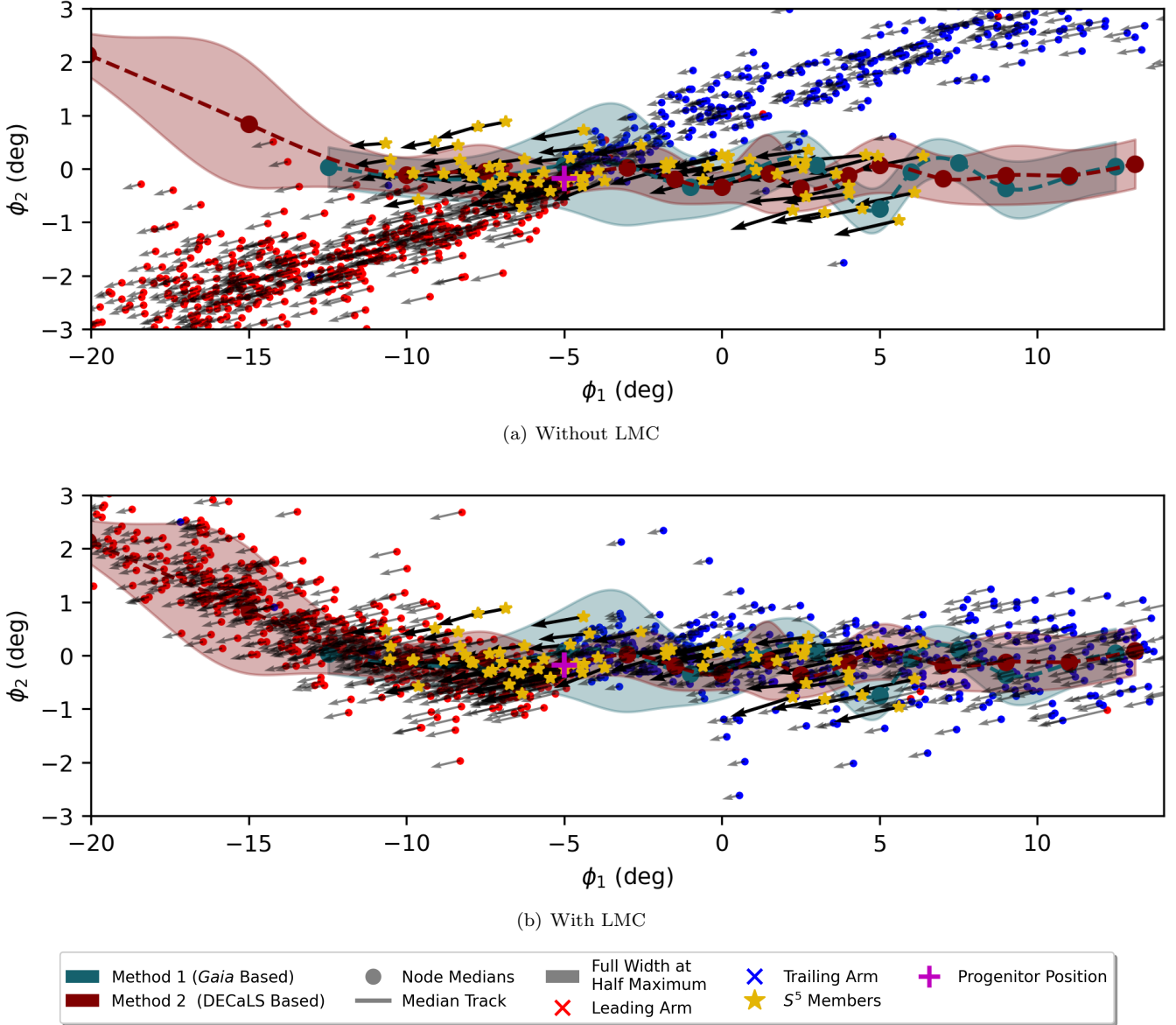


Figure 17. On-sky distribution of particles in the dynamical simulation of 300S overplotted onto the empirical stream models. (a) The results of the simulation with the same progenitor initial conditions while excluding the influence of the LMC. It is very challenging to find progenitor initial conditions which lead to simulated particles matching both the S^5 kinematics and the on-sky distribution of the tail of 300S. (b) The results of the simulation including the influence of the LMC. From these simulations, it is clear that the LMC had a substantial influence on the present day morphology of 300S, resulting in a rotation of the stream track by $\sim 11^\circ$. The simulation reproduces the position and slope of the kink, indicating it to be a real structure.

7.2. Discussion of the Dynamical Model

We present the results of the dynamical model in Figures 17, 18, and 19.¹¹ In Figure 17, we show the on-sky particle distribution from the simulation with and with-

¹¹ We also include an animation showcasing 300S’s evolution with time and the effect of the LMC perturbation. There are two versions of the animation. The first can be found at <https://youtu.be/7MozYSgV5wQ> and just showcases 300S’s evolution in galactocentric coordinates. The second can be found at <https://youtu.be/s-lxWk-ZruE> and also displays 300S’s evolution in projections onto the $x-y$, $x-z$, and $y-z$ planes as well as an on-sky projection of 300S with coordinates transformed such that the x -axis is tangent to 300S’s orbit as projected onto the sky. We also include the particles’ present day phase space information at <https://zenodo.org/records/15391938>.

out the LMC interaction overplotted onto the empirical stream tracks. In Figure 18, we compare the simulated distance, proper motion, and radial velocity tracks from the model with the LMC against those of the S^5 member stars. Finally, in Figure 19 we show the orbit of 300S and its spatial distribution in galactocentric coordinates from the simulation with the LMC.

7.2.1. Agreement Between the Dynamical Model and the Empirical Results

The dynamical model’s on-sky tracks reveal the importance of the LMC interaction in explaining 300S’s modern day morphology. Figure 17(a) shows the result of the simulation without the influence of the LMC using the same progenitor current day phase space information.

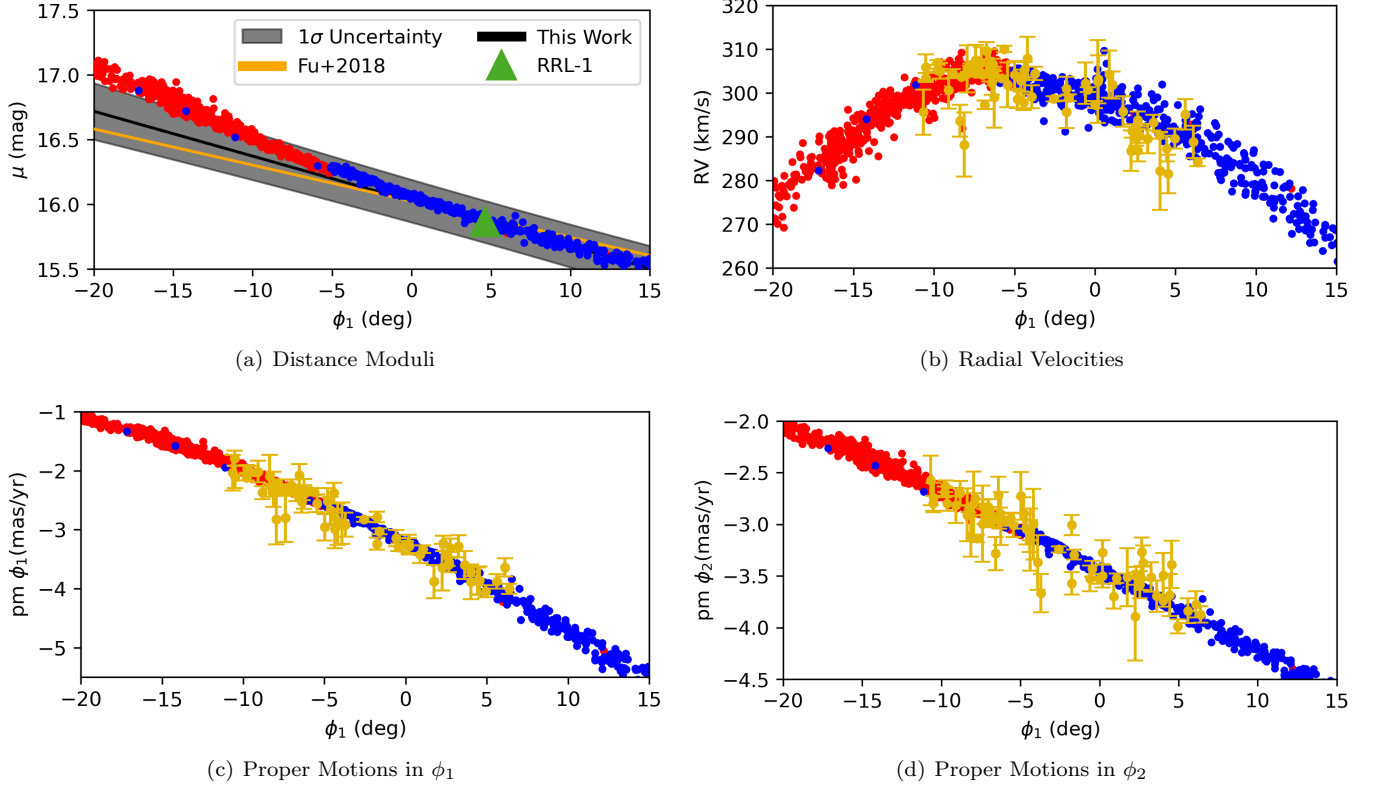


Figure 18. Comparison between the result of the dynamical simulation which includes the LMC and additional empirical properties of 300S. The three free variables – progenitor position, distance offset, and scale radius – were tuned by hand to match the data. The other variables were set using these parameters and tracks derived from the S^5 members and our empirical models. See Section 7.1 (a) Comparison between 300S’s distance gradient derived in Section 3.2, the transformed distance gradient of Fu et al. (2018) (see Section 3.2 and Equation 10), and the dynamical simulation distances. The dynamical simulation predicts a nonlinear distance gradient similar to the one observed in the data in Section 7.2.3. The dynamical simulation’s gradient at RRL-1’s ϕ_1 is close to the distance of RRL-1. (b) A comparison between the dynamical model’s radial velocities and those of the S^5 member stars. (c) A comparison between the dynamical model’s proper motions in ϕ_1 and those of the S^5 member stars. (d) A comparison between the dynamical model’s proper motions in ϕ_2 and those of the S^5 member stars. The kinematic comparisons are not reflex corrected per the discussion in Section 7.2.1.

Table 4
Current Day Phase Space Information for the LMC and 300S Used in the Dynamical Model.

Parameter	Stream	Parameter	LMC	Note
$\phi_{1,\text{prog}}$ (deg)	-5	α_{LMC} (deg)	80.8942	Kaisina et al. (2012)
$\phi_{2,\text{prog}}$ (deg)	-0.18	δ_{LMC} (deg)	-69.7561	Kaisina et al. (2012)
$v_{r,\text{prog}}$ (km s $^{-1}$)	303.5	$v_{r,\text{LMC}}$ (km s $^{-1}$)	262.2	van der Marel et al. (2002)
$d_{r,\text{prog}}$ (kpc)	$17.4 + d_{\text{offset}} = 18.0$	$d_{r,\text{LMC}}$ (kpc)	49.97	Pietrzyński et al. (2013)
$\mu_{\phi_1^*,\text{prog}}$ (mas yr $^{-1}$)	-2.6	$\mu_{\alpha^*,\text{LMC}}$ (mas yr $^{-1}$)	1.91	Kallivayalil et al. (2013)
$\mu_{\phi_2,\text{prog}}$ (mas yr $^{-1}$)	-3.1	$\mu_{\delta,\text{LMC}}$ (mas yr $^{-1}$)	0.229	Kallivayalil et al. (2013)
M_{prog} (M_{\odot})	$10^{4.7}$	M_{LMC} ($10^{10} M_{\odot}$)	18.4	Shipp et al. (2021)
r_{prog} (pc)	12.5	—	—	—

Except for their intersection at the progenitor’s location, the simulated track and empirical tracks differ substantially in this case. In fact, the trailing arm – considering particles with $\phi_1 < 15^\circ$ where both the majority of LMC model’s trailing arm particles ($\sim 73\%$), and the primary on-sky signal, are located – makes a 10.3° angle with the $\phi_2 = 0^\circ$ line. Indeed, due to the mismatch between the proper motion slopes and the stream track, it is very challenging to reproduce both the on-sky angle of the trailing arm and the S^5 member kinematics without the LMC. This result indicates that a substantial perturbative influence is necessary to explain 300S’s modern day track and kinematics.

Once the LMC is included in the dynamical model, the two on-sky tracks agree. Figure 17(b) shows the simulation’s track when the LMC is included. Now the track roughly follows the empirical on-sky track, with the angle between the tail and the $\phi_2 = 0^\circ$ line being only -0.2° . This implies that the LMC interaction results in a $\sim 11^\circ$ rotation of the stream track. Further, the dynamical model reproduces the kink that Method 2 identifies with the correct slope. This supports the kink being a real structure rather than an artifact of Sgr mismodeling. As both the stream’s overall on-sky angle and the presence of the kink are dependent on the LMC interaction, 300S’s track has the potential to be a strong constraint on the

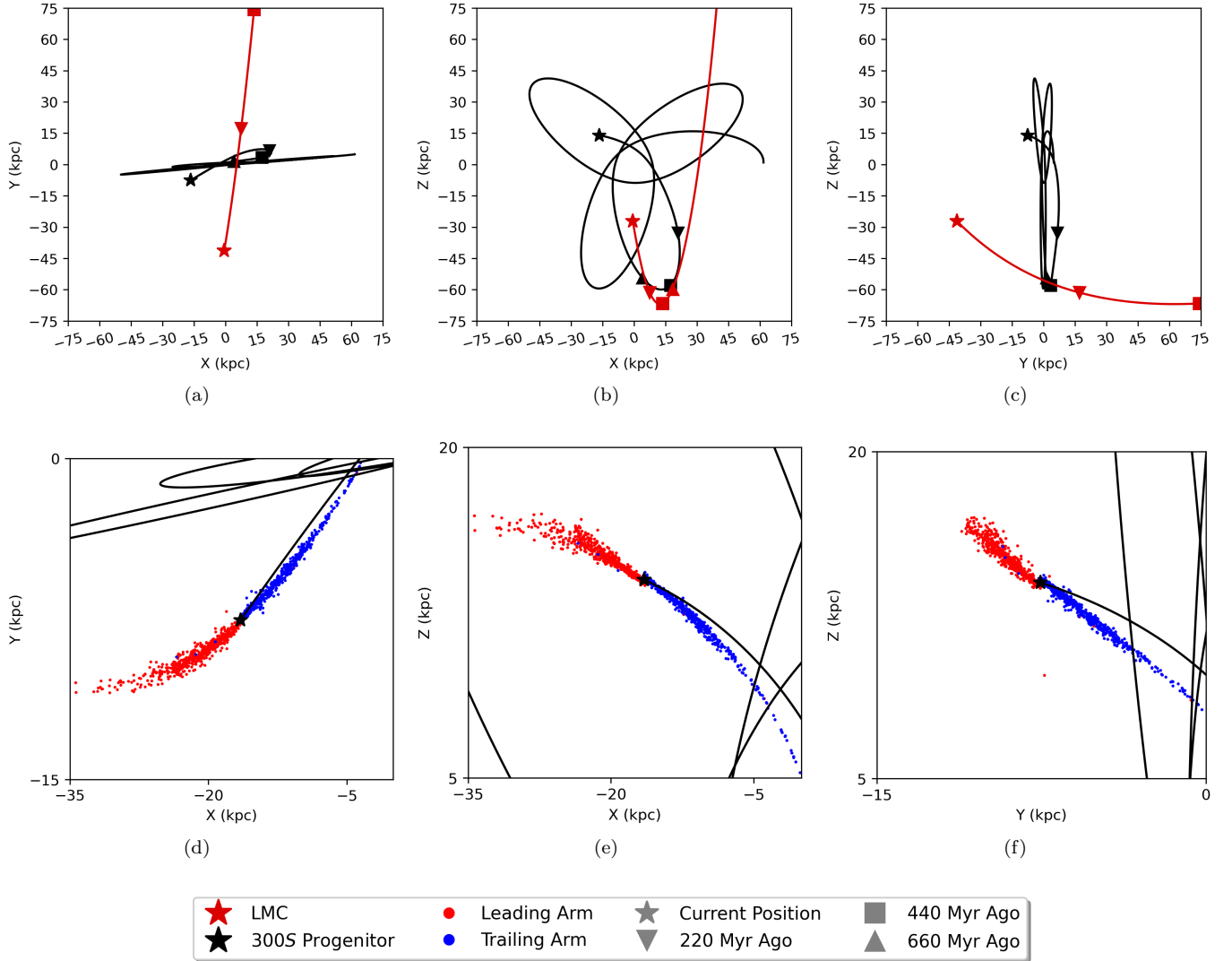


Figure 19. 300S’s orbit in the dynamical simulations with the LMC. 300S was integrated back 4 Gyr in these simulations. (a-c) Full views of the orbit in galactocentric coordinates using the same axis proportions as Figure 12 in Fu et al. (2018). 300S’s progenitor’s present day location is marked by a black star. The LMC’s trajectory is represented by the red line with the object’s present day position marked as a red star. The objects’ positions at previous times are also shown. 300S’s time of closest approach to the LMC at ~ 220 Myr ago is labeled with the upside down triangle. (d-f) Zoomed in views of 300S’s orbit showing the offset between the red and blue simulated stream particles and the black orbital track. The red points represent the leading arm of the stream and the blue represent the trailing arm. The clear misalignment between 300S and its orbital track is primarily due to the influence of the LMC.

LMC’s present mass. The LMC induced misalignment between the stream track and the orbital track is clearly visible in galactocentric coordinates in Figure 19 as well.

The dynamical simulation produces a nonlinear distance gradient which we compare with the empirical distance gradient derived in Section 3.2 and with the gradient of Fu et al. (2018) in Figure 18(a). This figure makes clear why a progenitor distance offset was necessary in the instantiation of the dynamical model. Although the simulation gradient agrees with the empirical one in positive ϕ_1 , it grows faster as ϕ_1 decreases. The distance offset makes up for this deviation at 300S’s progenitor’s location in the simulation at $\phi_1 = -5^\circ$. The dynamical model’s gradient is still within $\sim 1.7\sigma$ of the linear gradient over $\phi_1 \in [-20^\circ, 15^\circ]$. It identifies a stream distance of 15.0 kpc at the position of RRL-1 which agrees with 300S’s distance gradient at that position. Finally, the dynamical model’s gradient agrees with 300S’s overdensity in $\phi_1 - \mu$ space as described in Section 7.2.3 and seen in Figure 20.

The dynamical model proper motion tracks agree with the track formed by the S^5 member stars as seen in Figures 18(c) and 18(d). The radial velocity track also matches the S^5 member track as seen in Figure 18(b). These kinematics are not reflex corrected in order to remain independent of the particulars of the distance gradient.

Overall, the dynamical simulation and the empirical models are in good agreement in their spatial distributions and kinematics. This agreement includes the kink identified empirically by Method 2. It implies that a strong interaction with the LMC can produce the feature while being consistent with most of the stream’s other kinematic and spatial attributes. From this analysis, we conclude that the kink is possibly real and, if so, its formation and morphology could provide a strong constraint on the LMC’s mass. Further investigations and spectroscopic followup in the region will be necessary to fully confirm or reject the feature.

7.2.2. Orbital Characteristics

The dynamical simulation identifies 300S’s orbit to have an apocenter of 62.0 kpc and a pericenter of 7.1 kpc with an eccentricity of 0.80. This is around the same eccentricity as found by Li et al. (2022), but with a larger pericenter and apocenter. Li et al. (2022) found an apocenter of 45.8 kpc and a pericenter of 5.8 kpc. Most of this difference is not due to the influence of the LMC. Without the LMC, we find 300S’s apocenter is 58.4 kpc and its pericenter is 6.8 kpc. Rather, the difference is likely due to modeling choices. For instance, Li et al. (2022) use the MW potential derived by McMillan (2017) which has a virial mass around 30% larger than MWPOTENTIAL2014 with our settings for R_0 and $V_c(R_0)$. Our results are similar to those of Fu et al. (2018) who found a pericenter/apocenter of 4.1/ ~ 60 kpc. Currently, 300S’s radius to the Galactic center is 23 kpc and it last passed pericenter 69 Myr ago. This is $\sim 8\%$ of 300S’s orbital period of 861 Myr in our model.

7.2.3. Nonlinear Distance Gradient

Figure 18(a) shows that the dynamical simulation of 300S produces a nonlinear distance gradient that agrees

with our empirically derived gradient in positive ϕ_1 but diverges slightly at negative ϕ_1 . In this section, we analyze the possibility of 300S having a nonlinear distance gradient.

To begin, we use our Sgr model and our matched filter definitions to investigate 300S’s distribution in $\phi_1 - \mu$ space. We derive its $M_{300S}(\phi_1, \mu)$ distribution as we did for Sgr in Section 5.2.2 and Figure 9. We again begin by selecting an on-stream region. To capture the kink, we consider quadrilateral bins with corners $\phi_2 = \Phi_2(\phi_1) \pm 0.75^\circ$ where $\Phi_2(\phi_1)$ is the Method 2 stream track. We set $\Delta\phi_1$ to a constant 0.8° . We compute $M_{300S}(\phi_1, \mu)$ by again considering μ values from 14.2 to 19 (6.9–63.1 kpc) with $\Delta\mu = 0.05$. We use a new matched filter defined as in Section 3.1 (Equations 1 and 2) with $s = 1/3$. The resulting $M_{300S}(\phi_1, \mu)$ is heavily contaminated by Sgr. To obtain any useful result from this distribution, it is once again necessary to compute Sgr’s contribution and subtract it out.

In order to subtract Sgr’s contribution, we consider the stars within the reflection of the bins across Sgr’s stream track at their respective λ coordinates. We then compute a new $M_{300S}^{(\text{background})}(\phi_1, \mu)$ using stars which fall in the corresponding reflected bins. Finally, we compute the background subtracted distribution $M'(\phi_1, \mu) = M_{300S}(\phi_1, \mu) - M_{300S}^{(\text{background})}(\phi_1, \mu)$. We show $M'(\lambda, \mu)$ in Figure 20.

We first note that our subtraction of Sgr’s influence appears successful. In Figure 20, the four peaks in 300S’s stellar density are visible at the correct ϕ_1 values. We also find that the extracted overdensity matches the distance to RRL-1 at its ϕ_1 position.

Interestingly, the gradient of the overdensity in Figure 20 appears nonlinear. We overplot the distance gradient derived from the S^5 member stars in Section 3.2 as the light blue dashed line. Although the overdensity generally agrees with this gradient, there are some deviations. In $\phi_1 \gtrsim 0^\circ$ the gradient decreases faster than the overdensity and the former’s slope has a larger magnitude. In $\phi_1 \lesssim 0^\circ$, the linear gradient’s slope appears to have a smaller magnitude and varies slower.

Although 300S’s overdensity appears to have a more extreme slope than the distance gradient between $\phi_1 \sim -15^\circ$ and $\sim -5^\circ$, it bends down again between $\phi_1 \sim -20^\circ$ and $\sim -16^\circ$. It is unclear whether this bend is real. 300S’s kink causes its track to approach Sgr’s track in the relevant region, making it more difficult to fully remove Sgr’s contamination. The overdensity at -20° is near the distance of Sgr in the region, see Figure 9, implying that it could be contamination. Nevertheless, the complex behavior of 300S’s distance indicates a possible undermodeling of 300S in those regions.

As an additional check, we compare the velocity of the stream with its spatial distribution. Generally, streams that are unperturbed travel in the same direction as they are extended (e.g., Erkal et al. 2019; de Boer et al. 2020; Li et al. 2021; Shipp et al. 2021). As can be seen in Figure 21, the S^5 members and dynamical simulation particles’ v_r/μ_{ϕ_1} are in strong agreement and are both misaligned with the linear stream slope, especially in the vicinity of the kink. This pattern is independent of the specific distance gradient used to compute the solar reflex correction. The ratio more closely mimics the slope

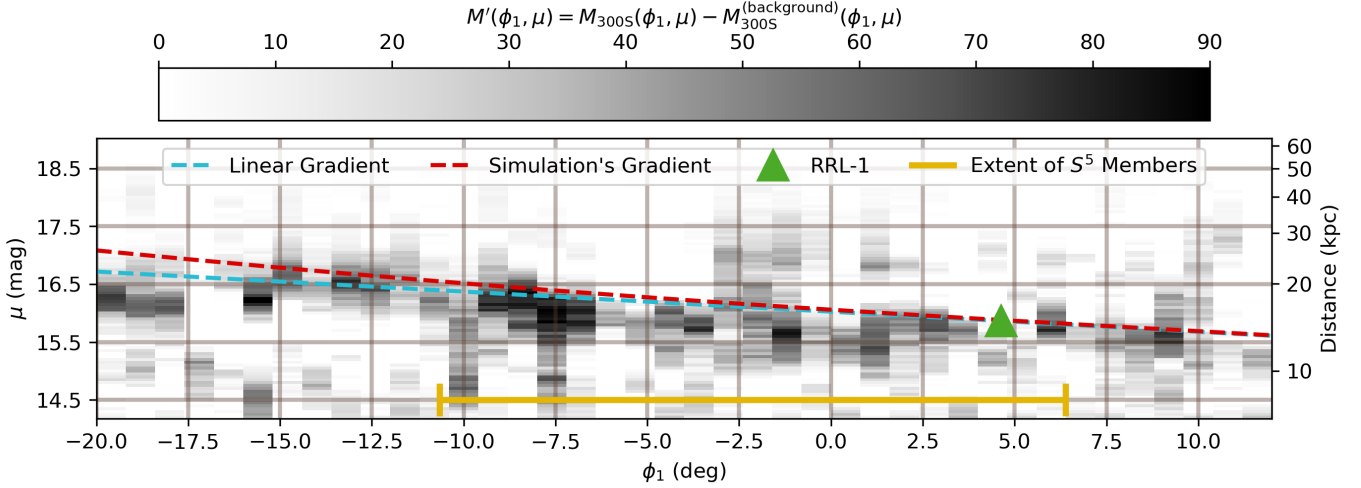


Figure 20. The background subtracted $\phi_1 - \mu$ distribution for 300S. The yellow line represents the extent of the S^5 members that were used in Section 3.2 to compute 300S’s distance gradient. RRL-1 is shown as a green triangle. 300S’s gradient itself is shown as a blue dashed line. Although the gradient approximately follows the stream overdensity, the stream distance appears to curve upward (i.e. towards larger distances) faster than the gradient in negative ϕ_1 and appears flatter than the gradient in positive ϕ_1 . The red dashed line is the distance function we find through our dynamical simulations of 300S. Its curvature matches 300S’s and captures the upturn at $\phi_1 \lesssim -5^\circ$, although it does not account for the overdensity at $\phi_1 \sim -20^\circ$.

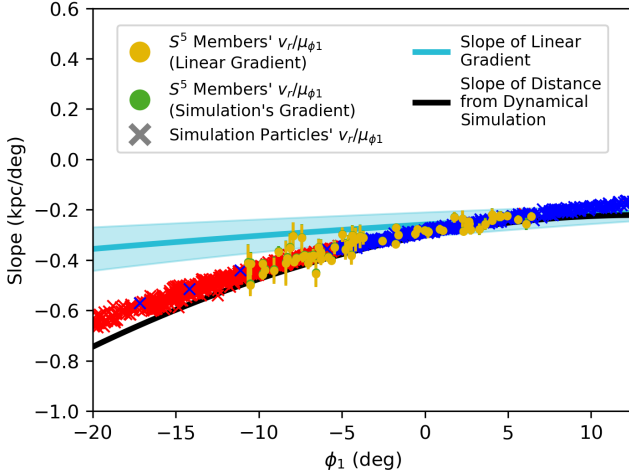


Figure 21. Relation between radial velocity and distance gradient for 300S. The yellow dots and associated uncertainties represent the S^5 member velocity slope after reflex correction using the 300S distance gradient derived in Section 3.2. The green points represent the velocity slope after reflex correction using the distance gradient derived from the dynamical simulation. 1σ uncertainty in the linear gradient slope is shown in the shaded region.

of the nonlinear gradient identified by the dynamical simulation. However, perturbations can also form offsets between the distance gradient slope and v_r/μ_{ϕ_1} (e.g., Shipp et al. 2021).

Overall, we find tentative evidence that 300S has a nonlinear distance gradient. However, we considered a nonlinear fit to both the S^5 members and the horizontal branch candidates identified using Equation 13 and found that neither dramatically altered the resulting empirical models. So we leave additional study to future work. Additional simulation work would help pin down a precise functional form for 300S’s gradient that describes any nonlinearity, and additional spectroscopic members will help constrain the gradient robustly against Sgr.

7.2.4. The Influence of the LMC

Figure 17 visually demonstrates how the LMC strongly influenced the formation and morphology of 300S. In this section, we quantify the strength of this relationship.

Shipp et al. (2021) utilized dynamical models of stellar streams to infer the mass of the LMC. To compare the relative strength of different streams in this inference, they considered the streams’ relative velocities and distances compared to the LMC at their closest approach. Generally, the closer a stream’s approach and the lower its relative velocity to the LMC, the stronger its perturbation. They noted, however, that not all perturbations are created equal. Perturbations in the radial direction lead to measurable differences in distance gradient and radial velocity, while perturbations in the on-sky plane lead to measurable differences in angular position and proper motion. As the distance gradient is difficult to measure with accuracy, the former type of perturbation leads to weaker constraints. To quantify this “measurability” of an LMC-induced perturbation, Shipp et al. (2021) introduced the metric $\hat{r}_{\text{LMC}} \cdot \hat{L}$ as the dot product of the unit vector between a segment of the stream and the LMC with the stream segment’s normalized angular momentum. Approximately, the closer this metric is to 1, the more the perturbation is realized as measurable on-sky effects.

We provide 300S’s position within closest approach distance-relative velocity space in Figure 22(c). To avoid biasing the results with particles that are emitted after closest approach, we only consider particles released over 220 Myr ago. 300S has a median $\hat{r}_{\text{LMC}} \cdot \hat{L}$ of 0.6. Interestingly, this value changed substantially over 300S’s interaction with the LMC, as seen in Figure 22(a). During 300S’s approach towards the LMC, $\hat{r}_{\text{LMC}} \cdot \hat{L}$ was ≥ 0.9 and on the same order as most of the OC stream, the stellar stream leading to the best constraint on the LMC mass of those analyzed by Shipp et al. (2021). However, during the 300S-LMC interaction, $\hat{r}_{\text{LMC}} \cdot \hat{L}$ decreased to

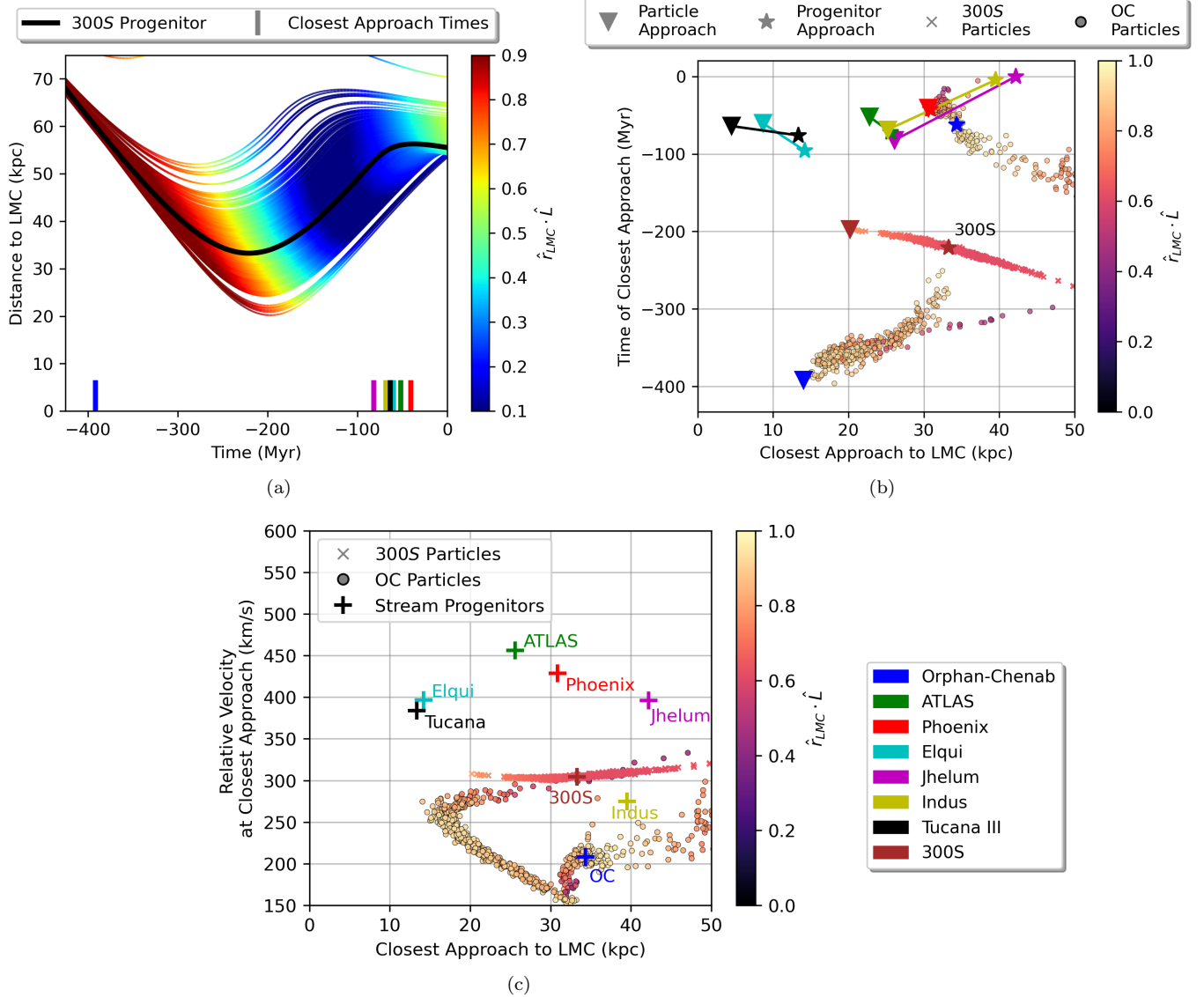


Figure 22. Summary of kinematic relation between 300S and the LMC. (a) The time dependence of the 300S-LMC interaction. The multicolored lines are the trajectories of 300S’s particles. The color represents $\hat{r}_{\text{LMC}} \cdot \hat{L}$ as a metric for the on-sky visibility of the perturbation. For more details, see Shipp et al. (2021). The black line shows the trajectory of 300S’s progenitor. Note especially the gradient in $\hat{r}_{\text{LMC}} \cdot \hat{L}$ over time and its high value on 300S’s approach towards the LMC. The colored vertical ticks represent the times of closest particle approach for the streams simulated by Shipp et al. (2021). (b) A comparison between 300S’s closest approach time and distance with other streams’ closest approach times and distances. The triangles represent the time and distance of closest particle approach while the stars represent the time and distance of closest progenitor approach. Streams without plotted particles have their markers connected for easier comparison. Note how 300S captures a unique period around 220 Myr ago which is not probed by any stream other than OC, whose closest particle approach and closest progenitor approach straddle 300S. (c) 300S’s position in closest approach distance-relative velocity space compared to other streams. Stream particles are included for the OC stream and 300S in (b) and (c).

below 0.1. This indicates that much of the on-sky perturbation of 300S occurred during its approach towards the LMC.

To make 300S’s results comparable to those of other streams, we simulate the streams considered by Shipp et al. (2021) within our simulation environment using the particle spray model of Chen et al. (2024) which we use for 300S. We utilize the stream progenitor current day parameters described in Shipp et al. (2021)’s Table A.1 for each of the streams they considered. Differences between our results and Shipp et al. (2021)’s are due to the sensitivity of stellar streams to model hyperparam-

eters (e.g. Koposov et al. 2023). However, we recover their general results. We compare 300S and the other streams in Figure 22.

Compared to the streams analyzed by Shipp et al. (2021), 300S has a reasonably small velocity relative to the LMC, but an average distance to the LMC upon its closest approach. Specifically, its progenitor’s closest approach was ~ 33 kpc, which is closer than 3 of the 7 streams measured in Shipp et al. (2021). The trailing arm of 300S approaches closer, at around 25 kpc. The relative velocity of 300S’s progenitor at closest approach was 304 km s^{-1} , which is smaller than 5 of the 7 streams

measured by Shipp et al. (2021).

Additionally, 300S has a unique time of closest approach. As seen in Figure 22(a), 300S’s progenitor passed through its closest approach to the LMC 221 Myr ago. 300S’s closest particle to the LMC passed its closest approach around 197 Myr ago. This is nearly 200 Myr later than the approach of the closest OC stream particle at 392 Myr ago. That time is shown in Figure 22(a) as a vertical, blue tick. Generally, 300S fills in the gap in the times of closest approach found by Shipp et al. (2021), as seen in Figure 22(b). Other than the OC stream, each stream has a time of closest progenitor approach and closest particle approach $\lesssim 100$ Myr ago. 300S’s closest approach time of 221 Myr fits in the middle between the OC stream’s closest particle approach and the other streams’ approaches. Due to the difference in time of closest approach between 300S and these other streams, 300S could act to probe the LMC at a different and less accessible moment in its temporal evolution. This new moment could act to better constrain the LMC’s mass evolution and its orbit, as done in Koposov et al. (2023). However, the measurability of more recent parts of 300S’s LMC interaction may be limited, as indicated by the decreasing $\hat{r}_{\text{LMC}} \cdot \hat{L}$ over the interaction.

Overall, the 300S-LMC interaction is both relatively strong and observable. The interaction acts to both rotate 300S’s on-sky distribution and produce a kink in 300S. 300S has a very high $\hat{r}_{\text{LMC}} \cdot \hat{L}$ on its approach although its $\hat{r}_{\text{LMC}} \cdot \hat{L}$ decreases over the interaction. In relation to other streams, 300S has a small relative velocity upon closest approach. These features motivate additional study of 300S’s utility as a constraint on the LMC’s mass.

8. CONCLUSIONS

In this paper, we present our study of the 300S stellar stream’s morphology and formation. Understanding these attributes facilitates both additional follow-up observations of 300S and further studies of the stream’s complex development. They also lay the groundwork for using 300S to constrain the structure of our Galaxy and, potentially, the LMC.

Sgr is the primary difficulty in understanding 300S’s morphology because it acts to contaminate the majority of the relevant field. To extract 300S’s morphology against this contamination, we identified a coordinate system for 300S and re-derived its distance gradient with a method robust against Sgr’s influence (Section 3.1 and 3.2 respectively). We then applied two methods to extract 300S’s signal and fit empirical models to its morphology. Method 1 used kinematic information to separate the signals (Section 4) while Method 2 used photometric information to simultaneously model 300S and Sgr (Section 5). Motivated by these empirical results, we performed dynamical modeling to study the formation of 300S and its morphological features (Section 7).

The primary results of our empirical analysis can be found in Figures 3, 6, 13(d), and 14. From our empirical analysis, we make the following conclusions.

- We rederive a distance gradient robustly against Sgr contamination (see Section 3.2 and Figure 3).
- The empirical models generated using our two

methods agree on their overlap and together describe 300S across $\sim 32^\circ$, extending the known track by as much as 7° (see Figures 6 and 14).

- Overall, 300S is a thin stellar stream that closely follows a great circle except for its kink (see Section 6.1).
- Although 300S has a long angular extent, its physical length is relatively short at 9.7 kpc (see Section 6.1).
- Within the newly identified stream regions, we find that 300S has a possible gap and a kink (see Sections 6.1 and 6.3 and Figure 14).
- Within the primary stream region, we find three peaks labeled A, B, and C in stellar density. A fourth peak D has a less certain center and structure.
- The separation and periodicity of 300S’s peaks are consistent with epicycles; but could also be related to either the complex disruption of globular clusters, or to some other perturbative influence on 300S (see Section 6.1 and Figure 14).
- Using the integrated stellar density over our empirical models, we improve Usman et al. (2024)’s lower limit on stream mass from $\log_{10}(M/M_\odot) = 4.5$ to $\log_{10}(M/M_\odot) = 4.7$ (see Section 6.4 and Figure 16).

The primary results from our dynamical simulation can be found in Figures 17, 18, 19, and 22. From our dynamical simulation we make the following conclusions.

- Our dynamical simulation indicates that the LMC strongly influenced 300S’s formation, rotating the stream by approximately 11° (see Sections 7.2.1 and 7.2.4 and Figures 17 and 22).
- The dynamical simulation also reproduces 300S’s kink, and indicates that it may be explained by a strong interaction with the LMC (see Section 7.2.1 and Figure 17).
- We find possible evidence that 300S has a nonlinear distance gradient with a decreasing slope over increasing ϕ_1 (see Section 7.2.3 and Figure 20).
- Compared to other stellar streams used for constraining the LMC’s mass (Shipp et al. 2021), 300S’s closest approach with the LMC occurred at 221 Myr ago, a time distinct from other streams’ closest approaches (see Section 7.2.4 and Figure 22(a)).

There are multiple paths for further investigation of 300S. Improved dynamical simulations to better understand the 300S-LMC interaction would allow for a clearer picture of both 300S’s morphology itself and the LMC’s mass. Dynamical simulations could better constrain the formation of 300S’s peaks and kink. Further, because 300S’s interaction with the LMC leads to dramatic changes in its on-sky orientation, 300S has the potential

to be another strong constraint on the LMC’s mass. Due to its unique time of closest approach, further analysis of 300S’s interaction with the LMC could provide a look into the time evolution of the LMC’s mass profile. Because 300S is extremely sensitive to small scale dark matter subhalos (Lu et al. 2025) and on a retrograde orbit, further simulation studies could also examine whether 300S’s structure hints at interactions with these elusive objects.

Empirical follow-up on the nature and morphology of 300S’s kink – to confirm its existence and angular relation to the rest of the stream – would also be useful for this analysis. Additional spectroscopically confirmed members and improvements to the precision of their distances could also help pin down the form of the distance gradient and of peak D. Further investigations into 300S’s density peaks could provide a better understanding of the necessary disruption physics or to possible perturbers. Similarly, if peak D is confirmed by followup investigations, 300S’s gap provides another source for studies of the structure of 300S’s progenitor, globular cluster disruption, and of the MW potential. Overall, 300S is a rich source for further investigations.

ACKNOWLEDGMENTS

B.C. acknowledges support from the University of Chicago Provost Scholarship and Provost Scholars Program. A.P.J. acknowledges support from the National Science Foundation under grants AST-2206264 and AST-2307599. S.K. acknowledges support from the Science & Technology Facilities Council (STFC) grant ST/Y001001/1. For the purpose of open access, the author has applied a Creative Commons Attribution (CC BY) license to any Author Accepted Manuscript version arising from this submission. G.L. acknowledges funding from KICP/UChicago through a KICP Postdoctoral Fellowship. A.P.L. and T.S.L. acknowledge financial support from the Natural Sciences and Engineering Research Council of Canada (NSERC) through grant RGPIN-2022-04794. Y.Y. and G.F.L. acknowledge support from the Australian Research Council through the Discovery Program grant DP220102254. This research benefited from the Dwarf Galaxies, Star Clusters, and Streams Workshop hosted by the Kavli Institute for Cosmological Physics. This work was supported by the Australian Research Council Centre of Excellence for All Sky Astrophysics in 3 Dimensions (ASTRO 3D), through project number CE170100013. S.L.M. acknowledges the support of the Australian Research Council through Discovery Project grant DP180101791, and the support of the UNSW Scientia Fellowship Program.

The paper includes data obtained with the Anglo-Australian Telescope in Australia. We acknowledge the traditional owners of the land on which the AAT stands, the Gamilaraay people, and pay our respects to elders past, present and emerging.

The Legacy Surveys consist of three individual and complementary projects: the Dark Energy Camera Legacy Survey (DECaLS; Proposal ID #2014B-0404; PIs: David Schlegel and Arjun Dey), the Beijing-Arizona Sky Survey (BASS; NOAO Prop. ID #2015A-0801; PIs: Zhou Xu and Xiaohui Fan), and the Mayall z-band Legacy Survey (MzLS; Prop. ID #2016A-0453; PI: Arjun Dey). DECaLS, BASS and MzLS together include

data obtained, respectively, at the Blanco telescope, Cerro Tololo Inter-American Observatory, NSF’s NOIRLab; the Bok telescope, Steward Observatory, University of Arizona; and the Mayall telescope, Kitt Peak National Observatory, NOIRLab. Pipeline processing and analyses of the data were supported by NOIRLab and the Lawrence Berkeley National Laboratory (LBNL). The Legacy Surveys project is honored to be permitted to conduct astronomical research on Iolkam Du’ag (Kitt Peak), a mountain with particular significance to the Tohono O’odham Nation.

NOIRLab is operated by the Association of Universities for Research in Astronomy (AURA) under a cooperative agreement with the National Science Foundation. LBNL is managed by the Regents of the University of California under contract to the U.S. Department of Energy.

This project used data obtained with the Dark Energy Camera (DECam), which was constructed by the Dark Energy Survey (DES) collaboration. Funding for the DES Projects has been provided by the U.S. Department of Energy, the U.S. National Science Foundation, the Ministry of Science and Education of Spain, the Science and Technology Facilities Council of the United Kingdom, the Higher Education Funding Council for England, the National Center for Supercomputing Applications at the University of Illinois at Urbana-Champaign, the Kavli Institute of Cosmological Physics at the University of Chicago, Center for Cosmology and Astro-Particle Physics at the Ohio State University, the Mitchell Institute for Fundamental Physics and Astronomy at Texas A&M University, Financiadora de Estudos e Projetos, Fundacao Carlos Chagas Filho de Amparo, Financiadora de Estudos e Projetos, Fundacao Carlos Chagas Filho de Amparo a Pesquisa do Estado do Rio de Janeiro, Conselho Nacional de Desenvolvimento Cientifico e Tecnolico and the Ministerio da Ciencia, Tecnologia e Inovacao, the Deutsche Forschungsgemeinschaft and the Collaborating Institutions in the Dark Energy Survey. The Collaborating Institutions are Argonne National Laboratory, the University of California at Santa Cruz, the University of Cambridge, Centro de Investigaciones Energeticas, Medioambientales y Tecnologicas-Madrid, the University of Chicago, University College London, the DES-Brazil Consortium, the University of Edinburgh, the Eidgenossische Technische Hochschule (ETH) Zurich, Fermi National Accelerator Laboratory, the University of Illinois at Urbana-Champaign, the Institut de Ciencies de l’Espai (IEEC/CSIC), the Institut de Fisica d’Altes Energies, Lawrence Berkeley National Laboratory, the Ludwig Maximilians Universitat Munchen and the associated Excellence Cluster Universe, the University of Michigan, NSF’s NOIRLab, the University of Nottingham, the Ohio State University, the University of Pennsylvania, the University of Portsmouth, SLAC National Accelerator Laboratory, Stanford University, the University of Sussex, and Texas A&M University.

BASS is a key project of the Telescope Access Program (TAP), which has been funded by the National Astronomical Observatories of China, the Chinese Academy of Sciences (the Strategic Priority Research Program “The Emergence of Cosmological Structures” Grant # XDB09000000), and the Special Fund for Astronomy from the Ministry of Finance. The

BASS is also supported by the External Cooperation Program of Chinese Academy of Sciences (Grant # 114A11KYSB20160057), and Chinese National Natural Science Foundation (Grant # 12120101003, # 11433005).

The Legacy Survey team makes use of data products from the Near-Earth Object Wide-field Infrared Survey Explorer (NEOWISE), which is a project of the Jet Propulsion Laboratory/California Institute of Technology. NEOWISE is funded by the National Aeronautics and Space Administration.

The Legacy Surveys imaging of the DESI footprint is supported by the Director, Office of Science, Office of High Energy Physics of the U.S. Department of Energy under Contract No. DE-AC02-05CH1123, by the National Energy Research Scientific Computing Center, a DOE Office of Science User Facility under the same contract; and by the U.S. National Science Foundation, Division of Astronomical Sciences under Contract No. AST-0950945 to NOAO.

This work has made use of data from the European Space Agency (ESA) mission *Gaia* (<https://www.cosmos.esa.int/gaia>), processed by the *Gaia* Data Processing and Analysis Consortium (DPAC, <https://www.cosmos.esa.int/web/gaia/dpac/consortium>). Funding for the DPAC has been provided by national institutions, in particular the institutions participating in the *Gaia* Multilateral Agreement.

This work made use of `numpy` (Harris et al. 2020), `matplotlib` (Hunter 2007), `scipy` (Virtanen et al. 2020), `pandas` (McKinney et al. 2010; pandas development team 2023), `ipython` (Pérez & Granger 2007), `statsmodels` (Seabold & Perktold 2010), `shapely` (Gillies et al. 2022), `gala` (Price-Whelan 2017; Price-Whelan et al. 2024), and `galpy`¹² (Bovy 2015).

APPENDIX

A. SPLINE RESULTS FOR METHOD 1

In this appendix, we include spline node positions and values for 300S as found using Method 1 (Section 4). Here and in the other appendices, the provided node parameters may be used as inputs to a natural cubic spline interpolation scheme, such as `CubicSpline` from the Python library `scipy.interpolate` with `bc_type='natural'`. We additionally provide machine readable versions of these tables, as well the complete set of samples for the models and the present day states of the dynamical simulation particles, at <https://zenodo.org/records/15391938>.

¹² <http://github.com/jobovy/galpy>

Table A1
Spline Nodes for $\Phi_2(\phi_1)$ for Method 1

ϕ_1 (deg)	Median	16%	84%
-12.4722	0.03451	-0.15458	0.23195
-7.5	-0.16588	-0.2858	-0.05416
-5	0.07033	-0.13633	0.25153
-3	0.04836	-0.28184	0.3611
-1	-0.3357	-0.5696	-0.11528
1	-0.01952	-0.23315	0.23527
3	0.06788	-0.07103	0.20049
5	-0.7419	-1.06453	-0.15301
6	-0.05864	-0.44178	0.1797
7.5	0.11682	-0.13757	0.33846
9	-0.35772	-0.93933	0.49332
11	-0.14704	-1.1424	0.862
12.47615	0.04826	-0.9441	1.00607

Table A2
Spline Nodes for $w(\phi_1)$ for Method 1

ϕ_1 (deg)	Median	16%	84%
-12.4722	-1.1482	-1.56019	-0.749
-7.5	-0.96866	-1.22905	-0.74144
-5	-0.359	-0.61178	-0.12468
-3	-0.06608	-0.42604	0.17956
-1	-0.69863	-1.09264	-0.38308
1	-0.73258	-1.2275	-0.2789
3	-0.9855	-1.21629	-0.74314
5	-1.04113	-1.55225	-0.51345
6	-1.1174	-1.58302	-0.66265
7.5	-1.1564	-1.58847	-0.67537
9	-0.82212	-1.30515	-0.36033
11	-0.91997	-1.42016	-0.38506
12.47615	-0.94538	-1.45144	-0.43219

Table A3
Spline Nodes for $\mathcal{I}(\phi_1)$ for Method 1

ϕ_1 (deg)	Median	16%	84%
-12.4722	-1.09481	-1.83362	-0.47423
-7.5	-0.96614	-1.30942	-0.65287
-5	-0.99868	-1.34493	-0.67723
-3	-1.65766	-2.03268	-1.28925
-1	-1.1614	-1.58938	-0.72899
1	-1.86545	-2.46176	-1.31733
3	-0.88536	-1.34635	-0.47797
5	-3.06207	-4.28368	-2.10239
6	-2.17293	-3.62987	-1.25492
7.5	-1.2604	-2.07768	-0.55286
9	-4.67722	-10.00582	-2.48122
11	-6.93234	-12.24508	-3.64041
12.47615	-8.99249	-13.13426	-4.54915

B. SPLINE RESULTS FOR SGR MODEL

In this appendix, we include the spline node positions and values for Sgr as found in Section 5.2.

Table B1
Spline Nodes for $\mathcal{B}(\lambda)$ for Sgr

λ (deg)	Median	16%	84%
-23.78772	0.09363	-0.11451	0.31663
-15	-0.72274	-0.8373	-0.61206
-5	-0.35984	-0.49998	-0.21786
0	-0.46852	-0.63451	-0.30133
5	0.13257	-0.02154	0.28308
11	-0.018	-0.18006	0.1528
16.20932	0.632	0.19356	1.09284

Table B2
Spline Nodes for $w(\lambda)$ for Sgr

λ (deg)	Median	16%	84%
-23.78772	0.87547	0.77479	0.97608
-15	0.84795	0.79479	0.90084
-5	1.04225	0.99478	1.09105
0	0.95295	0.88879	1.0153
5	0.93433	0.85965	1.00481
11	0.84543	0.7609	0.933
16.20932	0.68329	0.4453	0.89756

Table B3
Spline Nodes for $\mathcal{I}(\lambda)$ for Sgr

λ (deg)	Median	16%	84%
-23.78772	1.56917	1.48627	1.65099
-15	1.5144	1.47073	1.55763
-5	1.56675	1.52205	1.61157
0	1.54271	1.48907	1.59289
5	1.4115	1.35292	1.46659
11	1.375	1.30466	1.43639
16.20932	0.95117	0.77894	1.11815

C. SPLINE RESULTS FOR METHOD 2

In this appendix, we include spline node positions and values for 300S as found using Method 2 (Section 5).

Table C1
Spline Nodes for $\Phi_2(\phi_1)$ for Method 2

ϕ_1 (deg)	Median	16%	84%
-20.09482	2.13973	1.94689	2.35251
-15	0.83754	0.53236	1.10646
-10	-0.10692	-0.16822	-0.03979
-7.5	-0.04552	-0.11765	0.02836
-5	-0.18016	-0.23413	-0.12755
-3	0.01807	-0.08089	0.12465
-1.5	-0.19026	-0.31072	-0.0808
0	-0.33377	-0.49751	-0.17492
1.5	-0.0927	-0.40269	0.23555
2.5	-0.36475	-0.47459	-0.25023
4	-0.1276	-0.76882	0.63328
5	0.06985	-0.60708	0.72525
7	-0.18322	-0.84495	0.46682
9	-0.12043	-0.54863	0.21882
11	-0.12115	-0.60963	0.54154
13.09569	0.09346	-1.02696	1.04144

Table C2
Spline Nodes for $w(\phi_1)$ for Method 2

ϕ_1 (deg)	Median	16%	84%
-20.09482	-1.08362	-1.41119	-0.74395
-15	-0.00022	-0.37753	0.31449
-10	-1.27464	-1.48191	-1.0512
-7.5	-0.86829	-1.08127	-0.70401
-5	-1.40426	-1.57312	-1.22967
-3	-1.04102	-1.3476	-0.72157
-1.5	-0.95999	-1.21266	-0.72737
0	-1.35799	-1.69143	-0.991
1.5	-0.47983	-0.91903	-0.05595
2.5	-1.02566	-1.24726	-0.77864
4	-1.0223	-1.52709	-0.51001
5	-0.82289	-1.32445	-0.36727
7	-1.00148	-1.47787	-0.51148
9	-0.7672	-1.22214	-0.39706
11	-0.90397	-1.33514	-0.44385
13.09569	-0.94416	-1.43329	-0.43366

Table C3
Spline Nodes for $\mathcal{I}(\phi_1)$ for Method 2

ϕ_1 (deg)	Median	16%	84%
-20.09482	1.72369	1.32105	2.06118
-15	0.99816	0.73675	1.22487
-10	2.10921	1.89082	2.30911
-7.5	2.41012	2.24694	2.56922
-5	2.59217	2.39074	2.78161
-3	1.86333	1.50099	2.17118
-1.5	2.29467	2.00034	2.56773
0	1.51388	0.85506	1.98447
1.5	1.10012	0.36338	1.60074
2.5	2.51922	2.16935	2.81322
4	-2.38898	-3.98931	-0.80396
5	-0.5341	-3.26221	0.87144
7	-0.93168	-3.15648	0.5347
9	1.45176	0.4942	1.94699
11	-0.33036	-3.19487	1.06812
13.09569	-1.7112	-3.9308	0.75085

REFERENCES

- AAO software team. 2015, 2dfdr: Data reduction software, Astrophysics Source Code Library, record ascl:1505.015
- Abbott, T. M. C., Abdalla, F. B., Allam, S., et al. 2018, *ApJS*, 239, 18, doi: [10.3847/1538-4365/aae9f0](https://doi.org/10.3847/1538-4365/aae9f0)
- Banik, N., Bovy, J., Bertone, G., Erkal, D., & de Boer, T. 2021, *Journal of Cosmology and Astroparticle Physics*, 2021, 043, doi: [10.1088/1475-7516/2021/10/043](https://doi.org/10.1088/1475-7516/2021/10/043)
- Bastian, N., & Lardo, C. 2018, *ARA&A*, 56, 83, doi: [10.1146/annurev-astro-081817-051839](https://doi.org/10.1146/annurev-astro-081817-051839)
- Belokurov, V., Erkal, D., Evans, N. W., Koposov, S. E., & Deason, A. J. 2018, *MNRAS*, 478, 611, doi: [10.1093/mnras/sty982](https://doi.org/10.1093/mnras/sty982)
- Belokurov, V., & Koposov, S. E. 2015, *Monthly Notices of the Royal Astronomical Society*, 456, 602–616, doi: [10.1093/mnras/stv2688](https://doi.org/10.1093/mnras/stv2688)
- Belokurov, V., Zucker, D. B., Evans, N. W., et al. 2007, *The Astrophysical Journal*, 654, 897–906, doi: [10.1086/509718](https://doi.org/10.1086/509718)
- Bernard, É. J., Ferguson, A. M. N., Schlafly, E. F., et al. 2016, *Monthly Notices of the Royal Astronomical Society*, 463, 1759–1768, doi: [10.1093/mnras/stw2134](https://doi.org/10.1093/mnras/stw2134)
- Bland-Hawthorn, J., & Gerhard, O. 2016, *ARA&A*, 54, 529, doi: [10.1146/annurev-astro-081915-023441](https://doi.org/10.1146/annurev-astro-081915-023441)
- Bobylev, V. V., & Baykova, A. T. 2023, *Astronomy Reports*, 67, 812, doi: [10.1134/S1063772923080024](https://doi.org/10.1134/S1063772923080024)
- Bonaca, A., Geha, M., & Kallivayalil, N. 2012, *ApJL*, 760, L6, doi: [10.1088/2041-8205/760/1/L6](https://doi.org/10.1088/2041-8205/760/1/L6)
- Bonaca, A., Geha, M., Küpper, A. H. W., et al. 2014, *The Astrophysical Journal*, 795, 94, doi: [10.1088/0004-637x/795/1/94](https://doi.org/10.1088/0004-637x/795/1/94)
- Bonaca, A., Hogg, D. W., Price-Whelan, A. M., & Conroy, C. 2019, *The Astrophysical Journal*, 880, 38, doi: [10.3847/1538-4357/ab2873](https://doi.org/10.3847/1538-4357/ab2873)
- Bonaca, A., & Price-Whelan, A. M. 2024, *Stellar Streams in the Gaia Era*. <https://arxiv.org/abs/2405.19410>
- Bonaca, A., Naidu, R. P., Conroy, C., et al. 2021, *ApJL*, 909, L26, doi: [10.3847/2041-8213/abeaa9](https://doi.org/10.3847/2041-8213/abeaa9)
- Bovy, J. 2015, *The Astrophysical Journal Supplement Series*, 216, 29, doi: [10.1088/0067-0049/216/2/29](https://doi.org/10.1088/0067-0049/216/2/29)
- Bovy, J., Bahmanyar, A., Fritz, T. K., & Kallivayalil, N. 2016, *ApJ*, 833, 31, doi: [10.3847/1538-4357/833/1/31](https://doi.org/10.3847/1538-4357/833/1/31)
- Carlin, J. L., & Newberg, H. J. 2016, *Tidal Streams in the Local Group and Beyond* (Springer Cham)
- Carlin, J. L., Yam, W., Casetti-Dinescu, D. I., et al. 2012, *The Astrophysical Journal*, 753, 145, doi: [10.1088/0004-637x/753/2/145](https://doi.org/10.1088/0004-637x/753/2/145)
- Carpenter, B., Gelman, A., Hoffman, M. D., et al. 2017, *J Stat Softw*, 76
- Chambers, K. C., Magnier, E. A., Metcalfe, N., et al. 2016, *arXiv e-prints*, arXiv:1612.05560, doi: [10.48550/arXiv.1612.05560](https://doi.org/10.48550/arXiv.1612.05560)
- Chen, Y., Valluri, M., Gnedin, O. Y., & Ash, N. 2024, *Improved particle spray algorithm for modeling globular cluster streams*. <https://arxiv.org/abs/2408.01496>
- Clementini, G., Rippepi, V., Garofalo, A., et al. 2023, *Astronomy & Astrophysics*, 674, A18, doi: [10.1051/0004-6361/202243964](https://doi.org/10.1051/0004-6361/202243964)
- Cullinane, L. R., Mackey, A. D., Da Costa, G. S., et al. 2020, *Monthly Notices of the Royal Astronomical Society*, 497, 3055, doi: [10.1093/mnras/staa2048](https://doi.org/10.1093/mnras/staa2048)
- Cunningham, E. C., Hunt, J. A. S., Price-Whelan, A. M., et al. 2024, *The Astrophysical Journal*, 963, 95, doi: [10.3847/1538-4357/ad187b](https://doi.org/10.3847/1538-4357/ad187b)
- de Boer, T. J. L., Erkal, D., & Gieles, M. 2020, *MNRAS*, 494, 5315, doi: [10.1093/mnras/staa917](https://doi.org/10.1093/mnras/staa917)
- Deason, A. J., Belokurov, V., & Evans, N. W. 2011, *Monthly Notices of the Royal Astronomical Society*, 416, 2903–2915, doi: [10.1111/j.1365-2966.2011.19237.x](https://doi.org/10.1111/j.1365-2966.2011.19237.x)
- Dey, A., Schlegel, D. J., Lang, D., et al. 2019, *AJ*, 157, 168, doi: [10.3847/1538-3881/ab089d](https://doi.org/10.3847/1538-3881/ab089d)
- Ding, P.-J., Zhu, Z., & Liu, J.-C. 2019, *Research in Astronomy and Astrophysics*, 19, 068, doi: [10.1088/1674-4527/19/5/68](https://doi.org/10.1088/1674-4527/19/5/68)
- Dotter, A. 2016, *The Astrophysical Journal Supplement Series*, 222, 8, doi: [10.3847/0067-0049/222/1/8](https://doi.org/10.3847/0067-0049/222/1/8)
- Drimmel, R., & Poggio, E. 2018, *Research Notes of the American Astronomical Society*, 2, 210, doi: [10.3847/2515-5172/aaef8b](https://doi.org/10.3847/2515-5172/aaef8b)
- Erkal, D., Belokurov, V., Bovy, J., & Sanders, J. L. 2016, *MNRAS*, 463, 102, doi: [10.1093/mnras/stw1957](https://doi.org/10.1093/mnras/stw1957)
- Erkal, D., Koposov, S. E., & Belokurov, V. 2017, *Monthly Notices of the Royal Astronomical Society*, 470, 60–84, doi: [10.1093/mnras/stx1208](https://doi.org/10.1093/mnras/stx1208)
- Erkal, D., Belokurov, V., Laporte, C. F. P., et al. 2019, *Monthly Notices of the Royal Astronomical Society*, 487, 2685–2700, doi: [10.1093/mnras/stz1371](https://doi.org/10.1093/mnras/stz1371)
- Ferguson, P. S., Shipp, N., Drlica-Wagner, A., et al. 2021, *The Astronomical Journal*, 163, 18, doi: [10.3847/1538-3881/ac3492](https://doi.org/10.3847/1538-3881/ac3492)
- Flaugher, B., Diehl, H. T., Honscheid, K., et al. 2015, *The Astronomical Journal*, 150, 150, doi: [10.1088/0004-6256/150/5/150](https://doi.org/10.1088/0004-6256/150/5/150)
- Forbes, D. A. 2020, *Monthly Notices of the Royal Astronomical Society*, 493, 847–854, doi: [10.1093/mnras/staa245](https://doi.org/10.1093/mnras/staa245)
- Frebel, A., Lunnan, R., Casey, A. R., et al. 2013, *The Astrophysical Journal*, 771, 39, doi: [10.1088/0004-637x/771/1/39](https://doi.org/10.1088/0004-637x/771/1/39)
- Fu, S. W., Simon, J. D., Shetrone, M., et al. 2018, *The Astrophysical Journal*, 866, 42, doi: [10.3847/1538-4357/aad9f9](https://doi.org/10.3847/1538-4357/aad9f9)
- Gaia Collaboration, Prusti, T., de Bruijne, J. H. J., et al. 2016, *A&A*, 595, A1, doi: [10.1051/0004-6361/201629272](https://doi.org/10.1051/0004-6361/201629272)
- Gaia Collaboration, Vallenari, A., Brown, A. G. A., et al. 2023, *A&A*, 674, A1, doi: [10.1051/0004-6361/202243940](https://doi.org/10.1051/0004-6361/202243940)
- Garofalo, A., Delgado, H. E., Sarro, L. M., et al. 2022, *Monthly Notices of the Royal Astronomical Society*, 513, 788, doi: [10.1093/mnras/stac735](https://doi.org/10.1093/mnras/stac735)
- Garofalo, A., Cusano, F., Clementini, G., et al. 2013, *ApJ*, 767, 62, doi: [10.1088/0004-637x/767/1/62](https://doi.org/10.1088/0004-637x/767/1/62)
- Geha, M., Willman, B., Simon, J. D., et al. 2009, *The Astrophysical Journal*, 692, 1464–1475, doi: [10.1088/0004-637x/692/2/1464](https://doi.org/10.1088/0004-637x/692/2/1464)
- Gelman, A., & Rubin, D. B. 1992, *Statistical Science*, 7, 457, doi: [10.1214/ss/1177011136](https://doi.org/10.1214/ss/1177011136)
- Gillies, S., van der Wel, C., Van den Bossche, J., et al. 2022, *Shapely*, 2.0.0, doi: [10.5281/zenodo.5597138](https://doi.org/10.5281/zenodo.5597138)
- GRAVITY Collaboration, Abuter, R., Amorim, A., et al. 2018, *A&A*, 615, L15, doi: [10.1051/0004-6361/201833718](https://doi.org/10.1051/0004-6361/201833718)
- Grillmair, C. J. 2013, *Proceedings of the International Astronomical Union*, 9, 405–405, doi: [10.1017/S1743921313006728](https://doi.org/10.1017/S1743921313006728)
- . 2017, *The Astrophysical Journal*, 834, 98, doi: [10.3847/1538-4357/834/2/98](https://doi.org/10.3847/1538-4357/834/2/98)
- Hambly, N., Andrae, R., De Angeli, F., et al. 2022, *Gaia DR3 documentation Chapter 20: Datamodel description, Gaia DR3 documentation, European Space Agency; Gaia Data Processing and Analysis Consortium*. Online at <https://gea.esac.esa.int/archive/documentation/GDR3/index.html>
- Harris, C. R., Millman, K. J., van der Walt, S. J., et al. 2020, *Nature*, 585, 357–362, doi: [10.1038/s41586-020-2649-2](https://doi.org/10.1038/s41586-020-2649-2)
- Hattori, K., Erkal, D., & Sanders, J. L. 2016, *MNRAS*, 460, 497, doi: [10.1093/mnras/stw1006](https://doi.org/10.1093/mnras/stw1006)
- Hayes, C. R., Majewski, S. R., Hesselquist, S., et al. 2020, *The Astrophysical Journal*, 889, 63, doi: [10.3847/1538-4357/ab62ad](https://doi.org/10.3847/1538-4357/ab62ad)
- Haywood, M., Di Matteo, P., Lehnert, M. D., et al. 2018, *ApJ*, 863, 113, doi: [10.3847/1538-4357/aad235](https://doi.org/10.3847/1538-4357/aad235)
- Helmi, A., Babusiaux, C., Koppelman, H. H., et al. 2018, *Nature*, 563, 85, doi: [10.1038/s41586-018-0625-x](https://doi.org/10.1038/s41586-018-0625-x)
- Hernquist, L. 1990, *ApJ*, 356, 359, doi: [10.1086/168845](https://doi.org/10.1086/168845)
- Hoffman, M. D., & Gelman, A. 2011, *The No-U-Turn Sampler: Adaptively Setting Path Lengths in Hamiltonian Monte Carlo*. <https://arxiv.org/abs/1111.4246>
- Hunter, J. D. 2007, *Computing in science & engineering*, 9, 90
- Ibata, R., Thomas, G., Famaey, B., et al. 2020, *The Astrophysical Journal*, 891, 161, doi: [10.3847/1538-4357/ab7303](https://doi.org/10.3847/1538-4357/ab7303)
- Ibata, R., Malhan, K., Martin, N., et al. 2021, *The Astrophysical Journal*, 914, 123, doi: [10.3847/1538-4357/abfcc2](https://doi.org/10.3847/1538-4357/abfcc2)
- Ibata, R., Malhan, K., Tenachi, W., et al. 2023, *Charting the Galactic acceleration field II. A global mass model of the Milky Way from the STREAMFINDER Atlas of Stellar Streams detected in Gaia DR3*. <https://arxiv.org/abs/2311.17202>
- Ji, A. P., Koposov, S. E., Li, T. S., et al. 2021, *The Astrophysical Journal*, 921, 32, doi: [10.3847/1538-4357/ac1869](https://doi.org/10.3847/1538-4357/ac1869)
- Johnston, K. V. 1998, *ApJ*, 495, 297, doi: [10.1086/305273](https://doi.org/10.1086/305273)
- Johnston, K. V., Sackett, P. D., & Bullock, J. S. 2001, *The Astrophysical Journal*, 557, 137–149, doi: [10.1086/321644](https://doi.org/10.1086/321644)
- Just, A., Berczik, P., Petrov, M. I., & Ernst, A. 2009, *Monthly Notices of the Royal Astronomical Society*, 392, 969–981, doi: [10.1111/j.1365-2966.2008.14099.x](https://doi.org/10.1111/j.1365-2966.2008.14099.x)
- Kaisina, E. I., Makarov, D. I., Karachentsev, I. D., & Kaisin, S. S. 2012, *Astrophysical Bulletin*, 67, 115, doi: [10.1134/S1990341312010105](https://doi.org/10.1134/S1990341312010105)
- Kallivayalil, N., van der Marel, R. P., Besla, G., Anderson, J., & Alcock, C. 2013, *ApJ*, 764, 161, doi: [10.1088/0004-637x/764/2/161](https://doi.org/10.1088/0004-637x/764/2/161)
- Koposov, S. E. 2019, *RVSpecFit: Radial velocity and stellar atmospheric parameter fitting*. <https://ascl.net/1907.013>
- Koposov, S. E., Belokurov, V., Li, T. S., et al. 2019, *Monthly Notices of the Royal Astronomical Society*, 485, 4726, doi: [10.1093/mnras/stz457](https://doi.org/10.1093/mnras/stz457)
- Koposov, S. E., Erkal, D., Li, T. S., et al. 2023, *Monthly Notices of the Royal Astronomical Society*, 521, 4936–4962, doi: [10.1093/mnras/stad551](https://doi.org/10.1093/mnras/stad551)
- Küpper, A. H. W., Balbinot, E., Bonaca, A., et al. 2015, *ApJ*, 803, 80, doi: [10.1088/0004-637x/803/2/80](https://doi.org/10.1088/0004-637x/803/2/80)

- Küpper, A. H. W., Kroupa, P., Baumgardt, H., & Heggie, D. C. 2010, *MNRAS*, 401, 105, doi: [10.1111/j.1365-2966.2009.15690.x](https://doi.org/10.1111/j.1365-2966.2009.15690.x)
- Küpper, A. H. W., Lane, R. R., & Heggie, D. C. 2012, *Monthly Notices of the Royal Astronomical Society*, 420, 2700–2714, doi: [10.1111/j.1365-2966.2011.20242.x](https://doi.org/10.1111/j.1365-2966.2011.20242.x)
- Küpper, A. H. W., Macleod, A., & Heggie, D. C. 2008, *Monthly Notices of the Royal Astronomical Society*, 387, 1248–1252, doi: [10.1111/j.1365-2966.2008.13323.x](https://doi.org/10.1111/j.1365-2966.2008.13323.x)
- Lewis, I. J., Cannon, R. D., Taylor, K., et al. 2002, *MNRAS*, 333, 279, doi: [10.1046/j.1365-8711.2002.05333.x](https://doi.org/10.1046/j.1365-8711.2002.05333.x)
- Li, T. S., Koposov, S. E., Zucker, D. B., et al. 2019, *Monthly Notices of the Royal Astronomical Society*, 490, 3508, doi: [10.1093/mnras/stz2731](https://doi.org/10.1093/mnras/stz2731)
- Li, T. S., Koposov, S. E., Erkal, D., et al. 2021, *The Astrophysical Journal*, 911, 149, doi: [10.3847/1538-4357/abeb18](https://doi.org/10.3847/1538-4357/abeb18)
- Li, T. S., Ji, A. P., Pace, A. B., et al. 2022, *The Astrophysical Journal*, 928, 30, doi: [10.3847/1538-4357/ac46d3](https://doi.org/10.3847/1538-4357/ac46d3)
- Limberg, G., Souza, S. O., Pérez-Villegas, A., et al. 2022, *ApJ*, 935, 109, doi: [10.3847/1538-4357/ac8159](https://doi.org/10.3847/1538-4357/ac8159)
- Limberg, G., Queiroz, A. B. A., Perottoni, H. D., et al. 2023, *The Astrophysical Journal*, 946, 66, doi: [10.3847/1538-4357/acb694](https://doi.org/10.3847/1538-4357/acb694)
- Liu, G.-C., Huang, Y., Zhang, H.-W., et al. 2020, *The Astrophysical Journal Supplement Series*, 247, 68, doi: [10.3847/1538-4365/ab72f8](https://doi.org/10.3847/1538-4365/ab72f8)
- Lu, J., Lin, T., Sholapurkar, M., & Bonaca, A. 2025, Detectability of dark matter subhalo impacts in Milky Way stellar streams. <https://arxiv.org/abs/2502.07781>
- Majewski, S. R., Skrutskie, M. F., Weinberg, M. D., & Osthheimer, J. C. 2003, *The Astrophysical Journal*, 599, 1082–1115, doi: [10.1086/379504](https://doi.org/10.1086/379504)
- Majewski, S. R., Schiavon, R. P., Frinchaboy, P. M., et al. 2017, *AJ*, 154, 94, doi: [10.3847/1538-3881/aa784d](https://doi.org/10.3847/1538-3881/aa784d)
- Malhan, K., & Ibata, R. A. 2018, *Monthly Notices of the Royal Astronomical Society*, 477, 4063, doi: [10.1093/mnras/sty912](https://doi.org/10.1093/mnras/sty912)
- Malhan, K., Valluri, M., & Freese, K. 2020, *Monthly Notices of the Royal Astronomical Society*, 501, 179, doi: [10.1093/mnras/staa3597](https://doi.org/10.1093/mnras/staa3597)
- Malhan, K., Ibata, R. A., Sharma, S., et al. 2022, *The Astrophysical Journal*, 926, 107, doi: [10.3847/1538-4357/ac4d2a](https://doi.org/10.3847/1538-4357/ac4d2a)
- Martin, N. F., de Jong, J. T. A., & Rix, H. 2008, *The Astrophysical Journal*, 684, 1075–1092, doi: [10.1086/590336](https://doi.org/10.1086/590336)
- Martin, N. F., Ibata, R. A., Starkenburg, E., et al. 2022, *Monthly Notices of the Royal Astronomical Society*, 516, 5331–5354, doi: [10.1093/mnras/stac2426](https://doi.org/10.1093/mnras/stac2426)
- Massari, D., Koppelman, H. H., & Helmi, A. 2019, *A&A*, 630, L4, doi: [10.1051/0004-6361/201936135](https://doi.org/10.1051/0004-6361/201936135)
- Mateu, C. 2023, *Monthly Notices of the Royal Astronomical Society*, 520, 5225–5258, doi: [10.1093/mnras/stad321](https://doi.org/10.1093/mnras/stad321)
- McKinney, W., et al. 2010, in *Proceedings of the 9th Python in Science Conference*, Vol. 445, Austin, TX, 51–56
- McMillan, P. J. 2017, *MNRAS*, 465, 76, doi: [10.1093/mnras/stw2759](https://doi.org/10.1093/mnras/stw2759)
- Musella, I., Ripepi, V., Marconi, M., et al. 2012, *ApJ*, 756, 121, doi: [10.1088/0004-637X/756/2/121](https://doi.org/10.1088/0004-637X/756/2/121)
- Neal, R. M. 2011, in *Handbook of Markov Chain Monte Carlo* (Chapman and Hall/CRC), doi: [10.1201/b10905](https://doi.org/10.1201/b10905)
- Niederste-Ostholt, M., Belokurov, V., Evans, N. W., et al. 2009, *Monthly Notices of the Royal Astronomical Society*, 398, 1771–1781, doi: [10.1111/j.1365-2966.2009.15287.x](https://doi.org/10.1111/j.1365-2966.2009.15287.x)
- Norris, J. E., Wyse, R. F. G., Gilmore, G., et al. 2010, *The Astrophysical Journal*, 723, 1632–1650, doi: [10.1088/0004-637x/723/2/1632](https://doi.org/10.1088/0004-637x/723/2/1632)
- Odenkirchen, M., Grebel, E. K., Rockosi, C. M., et al. 2001, *ApJL*, 548, L165, doi: [10.1086/319095](https://doi.org/10.1086/319095)
- Pace, A. B., Erkal, D., & Li, T. S. 2022, *The Astrophysical Journal*, 940, 136, doi: [10.3847/1538-4357/ac997b](https://doi.org/10.3847/1538-4357/ac997b)
- pandas development team. 2023, *pandas-dev/pandas: Pandas, v2.0.3*, Zenodo, doi: [10.5281/zenodo.8092754](https://doi.org/10.5281/zenodo.8092754)
- Patrick, J. M., Koposov, S. E., & Walker, M. G. 2022, *Monthly Notices of the Royal Astronomical Society*, 514, 1757, doi: [10.1093/mnras/stac1478](https://doi.org/10.1093/mnras/stac1478)
- Pearson, S., Price-Whelan, A. M., & Johnston, K. V. 2017, Gaps and length asymmetry in the stellar stream Palomar 5 as effects of Galactic bar rotation. <https://arxiv.org/abs/1703.04627>
- Pérez, F., & Granger, B. E. 2007, *Computing in Science & Engineering*, 9
- Perottoni, H. D., Limberg, G., Amarante, J. A. S., et al. 2022, *The Astrophysical Journal Letters*, 936, L2, doi: [10.3847/2041-8213/ac8846](https://doi.org/10.3847/2041-8213/ac8846)
- Pietrzyński, G., Graczyk, D., Gieren, W., et al. 2013, *Nature*, 495, 76, doi: [10.1038/nature11878](https://doi.org/10.1038/nature11878)
- Plummer, H. C. 1911, *MNRAS*, 71, 460, doi: [10.1093/mnras/71.5.460](https://doi.org/10.1093/mnras/71.5.460)
- Pourbaix, D., Arenou, F., Gavras, P., et al. 2022, *Gaia DR3 documentation Chapter 7: Non-single stars*, Gaia DR3 documentation, European Space Agency; Gaia Data Processing and Analysis Consortium.
- Price-Whelan, A., Souchereau, H., Wagg, T., et al. 2024, *adrn/gala: v1.9.1, v1.9.1*, Zenodo, doi: [10.5281/zenodo.13377376](https://doi.org/10.5281/zenodo.13377376)
- Price-Whelan, A. M. 2017, *The Journal of Open Source Software*, 2, doi: [10.21105/joss.00388](https://doi.org/10.21105/joss.00388)
- Price-Whelan, A. M., & Bonaca, A. 2018, *The Astrophysical Journal Letters*, 863, L20, doi: [10.3847/2041-8213/aad7b5](https://doi.org/10.3847/2041-8213/aad7b5)
- Price-Whelan, A. M., Sipőcz, B., Günther, H., et al. 2018, *The Astronomical Journal*, 156, 123
- Ramos, P., Mateu, C., Antoja, T., et al. 2020, *Astronomy & Astrophysics*, 638, A104, doi: [10.1051/0004-6361/202037819](https://doi.org/10.1051/0004-6361/202037819)
- Reid, M. J., & Brunthaler, A. 2004, *ApJ*, 616, 872, doi: [10.1086/424960](https://doi.org/10.1086/424960)
- Riello, M., De Angeli, F., Evans, D. W., et al. 2021, *Astronomy & Astrophysics*, 649, A3, doi: [10.1051/0004-6361/202039587](https://doi.org/10.1051/0004-6361/202039587)
- Rockosi, C. M., Beers, T. C., Allende Prieto, C., Wilhelm, R., & Sloan Digital Sky Survey Collaboration. 2003, in *American Astronomical Society Meeting Abstracts*, Vol. 203, American Astronomical Society Meeting Abstracts, 112.10
- Ruiz-Macias, O., Zarrouk, P., Cole, S., et al. 2021, *MNRAS*, 502, 4328, doi: [10.1093/mnras/stab292](https://doi.org/10.1093/mnras/stab292)
- Salpeter, E. E. 1955, *ApJ*, 121, 161, doi: [10.1086/145971](https://doi.org/10.1086/145971)
- Seabold, S., & Perktold, J. 2010, in *9th Python in Science Conference*
- Shipp, N., Drlica-Wagner, A., Balbinot, E., et al. 2018, *The Astrophysical Journal*, 862, 114, doi: [10.3847/1538-4357/aacdab](https://doi.org/10.3847/1538-4357/aacdab)
- Shipp, N., Erkal, D., Drlica-Wagner, A., et al. 2021, *The Astrophysical Journal*, 923, 149, doi: [10.3847/1538-4357/ac2e93](https://doi.org/10.3847/1538-4357/ac2e93)
- Simion, I. T., Belokurov, V., & Koposov, S. E. 2019, *MNRAS*, 482, 921, doi: [10.1093/mnras/sty2744](https://doi.org/10.1093/mnras/sty2744)
- Simon, J. D., Geha, M., Minor, Q. E., et al. 2011, *The Astrophysical Journal*, 733, 46, doi: [10.1088/0004-637x/733/1/46](https://doi.org/10.1088/0004-637x/733/1/46)
- Smith, G. A., Saunders, W., Bridges, T., et al. 2004, in *Ground-based Instrumentation for Astronomy*, ed. A. F. M. Moorwood & M. Iye, Vol. 5492, International Society for Optics and Photonics (SPIE), 410–420, doi: [10.1117/12.551013](https://doi.org/10.1117/12.551013)
- Soker, N., & Hadar, R. 2001, *Monthly Notices of the Royal Astronomical Society*, 324, 213–217, doi: [10.1046/j.1365-8711.2001.04310.x](https://doi.org/10.1046/j.1365-8711.2001.04310.x)
- Stan Development Team. 2018, *The Stan Core Library*. <http://mc-stan.org/19>
- Tavangar, K., Ferguson, P., Shipp, N., et al. 2022, *The Astrophysical Journal*, 925, 118, doi: [10.3847/1538-4357/ac399b](https://doi.org/10.3847/1538-4357/ac399b)
- Usman, S. A., Ji, A. P., Li, T. S., et al. 2024, Multiple Populations and a CH Star Found in the 300S Globular Cluster Stellar Stream. <https://arxiv.org/abs/2401.02476>
- van der Marel, R. P., Alves, D. R., Hardy, E., & Suntzeff, N. B. 2002, *AJ*, 124, 2639, doi: [10.1086/343775](https://doi.org/10.1086/343775)
- van der Marel, R. P., & Kallivayalil, N. 2014, *The Astrophysical Journal*, 781, 121, doi: [10.1088/0004-637x/781/2/121](https://doi.org/10.1088/0004-637x/781/2/121)
- Vasiliev, E., Belokurov, V., & Erkal, D. 2021, *MNRAS*, 501, 2279, doi: [10.1093/mnras/staa3673](https://doi.org/10.1093/mnras/staa3673)
- Virtanen, P., Gommers, R., Oliphant, T. E., et al. 2020, *Nature Methods*, 17, 261, doi: [10.1038/s41592-019-0686-2](https://doi.org/10.1038/s41592-019-0686-2)
- Vivas, A. K., Martínez-Vázquez, C., & Walker, A. R. 2020, *ApJS*, 247, 35, doi: [10.3847/1538-4365/ab67c0](https://doi.org/10.3847/1538-4365/ab67c0)
- Weatherford, N. C., Rasio, F. A., Chatterjee, S., et al. 2024, Stellar Escape from Globular Clusters. II. Clusters May Eat Their Own Tails. <https://arxiv.org/abs/2310.01485>
- Webb, J. J., & Bovy, J. 2019, *Monthly Notices of the Royal Astronomical Society*, 485, 5929, doi: [10.1093/mnras/stz867](https://doi.org/10.1093/mnras/stz867)
- Yang, Y., Lewis, G. F., Erkal, D., et al. 2025, *ApJ*, 984, 189, doi: [10.3847/1538-4357/adc57c](https://doi.org/10.3847/1538-4357/adc57c)
- Yanny, B., Rockosi, C., Newberg, H. J., et al. 2009, *AJ*, 137, 4377, doi: [10.1088/0004-6256/137/5/4377](https://doi.org/10.1088/0004-6256/137/5/4377)

provides fast and easy peer review for new papers in the astro-ph section of the arXiv, making the reviewing process simpler for authors and referees alike. Learn more

at <http://astro.theoj.org>.